Politechnika Wrocławska

FIELD OF SCIENCE: THE FIELD OF EXACT AND NATURAL SCIENCES

DISCIPLINE OF SCIENCE: PHYSICAL SCIENCE

DOCTORAL DISSERTATION

Fabrication, optimization and application of hybrid photonic microcomponents based on 2D materials

DARIA HLUSHCHENKO

Supervisor: Prof. Robert Kudrawiec

Keywords: 2D materials, sol-gel, photonic structures, waveguides, device

WROCLAW 2024

The work was created with the support of the project "Hybrid sensor platforms of integrated photonic systems based on ceramic and polymer materials" implemented as part of the TEAM-NET program of the Foundation for Polish Science financed by the European Union under the European Regional Development Fund, POIR.04.04.00-00- 14D6/18-02.

Acknowledgements

First of all I would like to thank my supervisor, Prof. Robert Kudrawiec, for providing the interesting ideas and valuable support during my PhD. I am also grateful for his support during working on the articles. Special thanks to Dr. Marta Gladysiewicz-Kudrawiec for introducing me into the band structure calculations using the *k·p* method and for great support in conducting the student classes.

Special thanks to Dr. Katarzyna Komorowska, for invaluable support in working in the CleanRoom laboratory, for showing the techniques and methods for fabrication photonic structures; for work on interesting ideas and their joint implementation.

I would like to extend my gratitude to Dr.Tomasz Baraniecki, Katarzyna Opolczynska, Dr.Anna Melnychenko, Aneta Mglosiek and Dr.Damian Pucicki for provided help and assistance during my PhD at PORT.

I would also like to acknowledge my colleagues from the department of the Wroclaw University of Science and Technology, Dr.Lukasz Gelczuk, Agata Tolloczko, Karolina Ciesolkiewicz for help with measurements and work on great ideas.

I would like to extend my gratitude to department of Optics and Photonics, especially for Dr. Jacek Olszewski, Dr. Tadeusz Martynkien and Karolina Gemza, who helped with spectral measurements and advices on my projects.

Finally, I want to thank my husband, Andrii Udovychenko, who always stood behind me and have supported me throughout my PhD. I dedicate this work to him.

Last but not least, I want to take this opportunity to thank my family, my father Sergii Hlushchenko, my mother Valentyna Hlushchenko and my brother Roman Hlushchenko.

TABLE OF CONTENTS

Abstract

There is currently trend to miniaturization, where the nanotechnology based on fabrication of the micro- and nano- structures develops more frequently. The main task of such miniaturization is to introduce the new cheaper material platforms to the market and improvement of photonic micro- and nanocomponents characteristics. The high application potential is observed for devices based on the two-dimensional (2D) van der Waals crystals like monochalcogenides (MX) and dichalcogenides (MX_2). The main advantage of such materials is ability to choose the thickness of material, appropriate spectral range, material type, possibility of doping *etc.*

Researching the stability of van der Waals crystals in ambient conditions is crucial for understanding their practical applicability and longevity in device fabrication and operation. Research, presented in this thesis, involve monitoring the exfoliated layered MX and MX_2 materials over time to assess any changes in their properties and performance.

Sol-gel SiO_x:TiO_y material offers transparency in the visible spectrum and low optical losses, making it an attractive alternative to commercial silicon platforms for photonic and optoelectronic applications. This material provides a versatile platform for integrating with 2D vdW crystals. The focus of the research is on the fabrication of photonic microcomponents such as waveguides and microdiscs, with the aim of integrating them with vdW crystals. This integration opens up possibilities for designing and realizing novel photonic devices with tailored characteristics.

The presented thesis demonstrates the integration of transition metal dichalcogenides with sol-gel SiO_x:TiO_y waveguides. This integration enables the fabrication of photonic devices with desired characteristics within the visible spectral range. Optical phenomena observed at the interfaces between the vdW crystals and sol-gel SiO_x:TiO_y microstructures are utilized for device fabrication. These phenomena likely include effects such as light-matter interactions and waveguide coupling, which can be exploited to engineer device functionality. For instance, MX_2-based photodetectors fabricated in this study exhibit the high photoresponsivity at specific bias voltages, indicating the potential for sensitive photodetection in optoelectronic systems.

Motivation and hypothesis

Research on 2D material-based devices is currently of great interest due to the ever-growing application needs of semiconductor devices, *i.e*. photodetectors, light-emitting diodes or lasers. These devices, especially in recent years, are used in areas such as optoelectronics, photovoltaic and energy storage. The 2D materials have also shown promise in the field of photovoltaics for harvesting solar energy. Their tunable bandgaps, high carrier mobilities, and excellent optical properties make them attractive candidates for use in solar cells and photodetectors.

The research outlined in this thesis revolves around three key hypotheses:

1) *Suitability of sol-gel SiO_x:TiO_y material for photonic microstructures.* The first hypothesis examines the possibility of fabricating photonic microstructures using the developed SiO_x:TiO_y material obtained via the sol-gel method. This hypothesis aims to determine whether the sol-gel platform can serve as a viable alternative to traditional commercial platforms such as silicon (Si), silicon nitride (Si_3N_4), and gallium arsenide (GaAs) for the production of photonic devices. This hypothesis addresses the materials suitability in terms of its optical properties, fabrication process compatibility, and overall performance compared to existing platforms.

2) *Integration of 2D materials with sol-gel SiO_x:TiO_y microstructures.* This hypothesis explores the possibility of integrating two-dimensional materials, such as vdW crystals, with the fabricated sol-gel microstructures. Integration involves considerations such as material compatibility, adhesion, and interface engineering. Successful integration would allow for the realization of hybrid photonic devices with combined functionalities.

3) *Fabrication of microdevices based on integration of exfoliated layered MX and MX_2 materials with sol-gel microstructures.* The third hypothesis focuses on the fabrication of microdevices by integrating vdW crystals with the sol-gel SiO_x:TiO_y waveguides. This hypothesis aims to demonstrate the practical realization of photonic devices leveraging the unique properties of both materials.

These hypotheses provide a structured approach for exploring the potential of sol-gel SiO_x:TiO_y microstructures and their integration with two-dimensional materials for advancing photonic device technology. Experimental validation of these hypotheses would contribute to the development of novel photonic devices with enhanced performance and functionality.

The first chapter of thesis presents an introduction to the two-dimensional materials. Methods of obtaining monolayers and few-layers from bulk vdW crystals by using mechanical exfoliation have been presented and discussed. Initially, the characterisation methods of 2D materials as Raman and photoluminescence spectroscopy were reported.

The second chapter describes the new material platform as sol-gel SiO_x:TiO_y, where such material is characterized by transparency in the visible spectrum, good transmission properties and low optical losses. Therefore, this material can be used as an alternative to commercial Si platform.

The third chapter provides an overview on fabrication techniques of photonic microstructures like photolithography, wet and dry etching, nanoimprint lithography (NIL). This chapter contains a brief description of the techniques for preparing metallic contacts to bulk and exfoliated layered materials and semiconductor devices.

The fourth chapter introduces the types of photonic microstructures and their applications. A brief description of the planned manufactured structures is included in this chapter.

Characterization of two-dimensional materials as well as the results of Raman and photoluminescence measurements for the studied materials and heterostructures are included in the fifth chapter of this work.

Research on the stability of van der Waals (vdW) crystals (monochalcogenides MX and dichalcogenides MX_2) in ambient conditions is presented in the sixth chapter. The chapter also contains results from encapsulation of the most reactive materials.

A detailed description of the fabrication and characterization of photonic microstructures like waveguides and microdiscs from sol-gel SiO_x:TiO_y is provided in chapter seven of this work.

The eighth chapter provides development in engineering of electrical contacts to bulk end exfoliated MX and MX_2 2D materials. The summary of obtained ohmic and Schottky contacts is presented and discussed. The original experimental results on realisation of electrical contacts based on high work-function metals are demonstrated.

The ninth chapter reports the research that proceeded with designing and fabrication of photodetectors by using WS_2 and MoS_2 as the active material integrated with sol-gel waveguides. The method of manufacturing the photodetector has been described in detail and experimental setup for measuring (*I-V*) characteristics is introduced.

In order to verify the presented research hypothesis, experiments were carried out, reported in detail in Chapter 9, which concerns results on microdevices fabrication by using techniques described in Chapter 3. Chapter 9 contains the results on the fabrication of the MX_2-based photodetectors. The photodetectors were designed and fabricated using exfoliated MX_2 as the active material. The active material in the photodetectors was contacted with platinum pads for electrical probing, providing better charge conduction and low contact resistance for the device.

The research presented in this thesis was performed within the Team-NET program titled: "Hybrid sensor platforms of integrated photonic systems based on ceramic and polymer materials". The program was aimed to develop of ceramic and polymer platforms like ceramic sol-gels for fabrication the photonic microcomponents and microdevices. My participation in the project involved the creation of photonic structures from the sol-gel SiO_x:TiO_y material; integration of fabricated microstructures with two-dimensional materials; manufacturing the integrated photonic devices.

1 TWO-DIMENSIONAL MATERIALS

1.1 Introduction to the two-dimensional materials

In the field of semiconductors is currently being observed the "post-Moore's Law" period, where the new materials with smaller dimensions and better properties will replace the currently used ones.[1] The silicon-based micro- and nano- devices have reached the theoretical limit and there is a need to obtain and research the new materials. The 2D materials represent alternatives to each silicon nanodevices due to high potential in electronic and optoelectronic applications.[1-15] Among the 2D materials, graphene, transition metal dichalcogenides (TMDCs), transition metal monochalcogenides (TMMCs) are the most interesting due to their properties. TMMCs have a general formula MX and TMDCs - MX_2, where M is a transition metal atom from group IV (Ti, Zr), V (V, Nb, Ta), VI (Mo, W), and X is a chalcogen atom (S, Se, Te), see Figure 1.1. Such layered materials contain covalently bonded and dangling-bond-free layers that are holding up by van der Waals forces. These materials are also so-called as van der Waals crystals (vdW).[14] The band gaps of these materials covers an energy range from 1 to 1.2 eV which is desired for optoelectronic applications. In layered materials (LMs) the physical properties can be predicted by controlling the layer thickness of the material through various manufacturing techniques. A great variety of 2D materials allows the creation of larger amount a combinations and heterojunctions than any traditional fabrication method.[13-15]

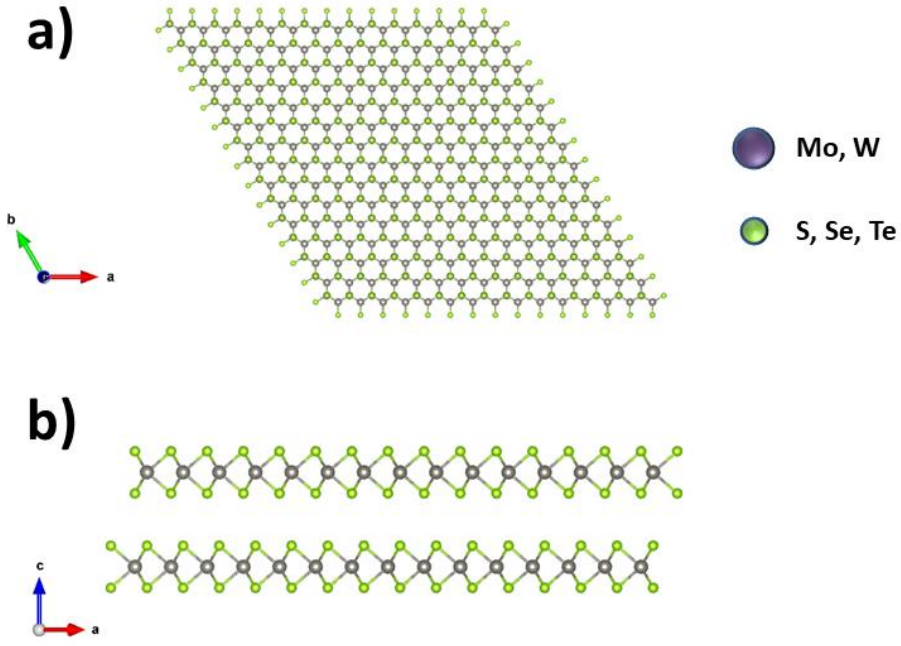

Figure 1.1. a) Top-view on atomic structure of TMDCs monolayer; b) Two TMDCs monolayers, the middle atom is transition metal atom and chalcogen atoms on both sides. The simulation of the layers was carried out in Avogadro molecular editor.

From the two-dimensional materials, graphene is the most popular and studied.[16-26] Graphene is a semiconductor with zero band gap, wide wavelength range and excellent optical properties, see Figure 1.2. Graphene found its application mainly as a transparent electrode in optoelectronic devices due to the high carrier mobility, mechanical strength and flexibility.[16-24]

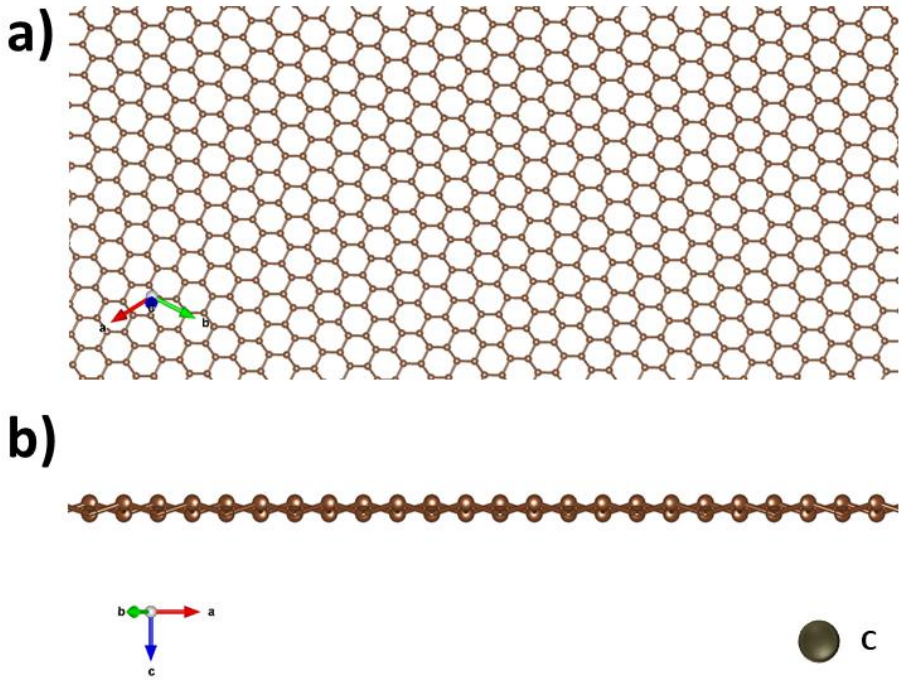

Figure 1.2. a) Top-view on atomic structure of graphene monolayer; b) Side view on graphene monolayer and C-C bonds. The simulation of the graphene monolayer was carried out in Avogadro molecular editor.

The group-IV layered materials with abbreviation of MX composed by a group-IV element (M=Sn or Ge) and chalcogen (X=S or Se). Such LMs have strong anisotropy and non-zero band gap.[27-28] The spectral characterization of group IV-VI compounds such as Raman spectra, refractive index and photoconductivity already have been investigated by a lot of research groups.[29-30]

The large monochalcogenide group is divided on IV monochalcogenide (GeS, GeSe, SnS and SnSe) semiconductors and group-III (GaS, GaSe, GaTe) LMs. The structures of monolayers from group IV-LMs represent orthorhombic formation with four atoms per unit cell. The distance between each layer is about 3.5 Å.[29] Between the two perpendicular in-plane directions the layer structure is greatly anisotropic (Figure 1.3). The orthorhombic structure of the monochalcogenides is presented as rectangular two-dimensional Brillouin Zone (BZ) with high-symmetry points for bulk along k_z and for monolayer and bilayers at the k_x- k_y plane (Figure 1.3c).

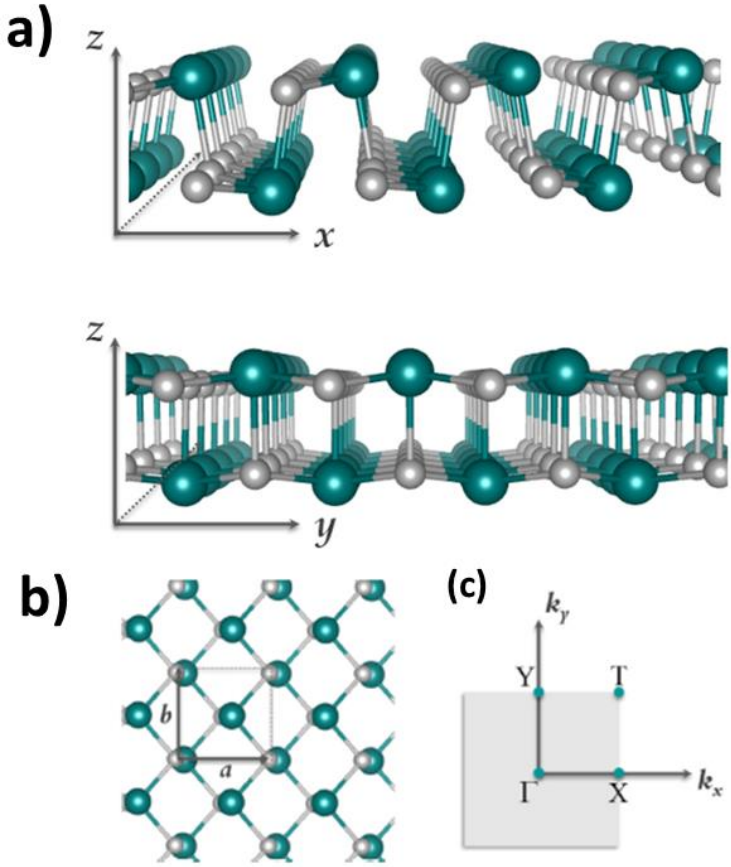

Figure 1.3. a) Side view of SnS monolayer (representing a typical group-IV monochalcogenide monolayer) at the *x*–*z* and *y*–*z* planes; b) The top view showing the lattice vectors a and b along the x and y-directions; c) Two-dimensional BZ and the high-symmetry points Γ, X, T, and Y. Reprinted with permission from Ref.[29]

The monochalcogenides LMs are characterised by a large bandgap for bulk crystals, beginning from 0.8 eV for SnSe material to 2.0 eV for GeS.[34] Cheng *et al.* calculated the bandgaps which are 1.65, 1.15, 1.46 and 0.88 eV for GeS, GeSe, SnS and SnSe monolayers, respectively.[30] Xu *et al.* determined the direct bandgap for GeSe monolayer and indirect for another monochalcogenides.[32]

1.2 The two-dimensional material obtainment and their characterisation

There are a few typical routes for fabrication the two-dimensional (2D) materials, see Figure 1.4. The most popular from them is top-down mechanical exfoliation method and bottom-up deposition methods, for instance, the chemical vapour deposition (CVD), plasma enhanced chemical vapour deposition (PECVD), molecular beam epitaxy (MBE), metal-organic chemical vapour deposition (MOCVD). Mechanical exfoliation is good in proof of concept the research development.[33] On a larger scale, when device fabrication is needed, must be used continuous films which are synthesized by the bottom-up methods. Moreover, most research groups used the CVD grown technique which gives films with higher yields, uniformity and continuity of layers.[35]

By using mechanical exfoliation, the 2D materials with high quality and size of crystals in micrometre scale can be obtained. Electrochemical exfoliation also used to produce the large 2D films but with low crystal quality.

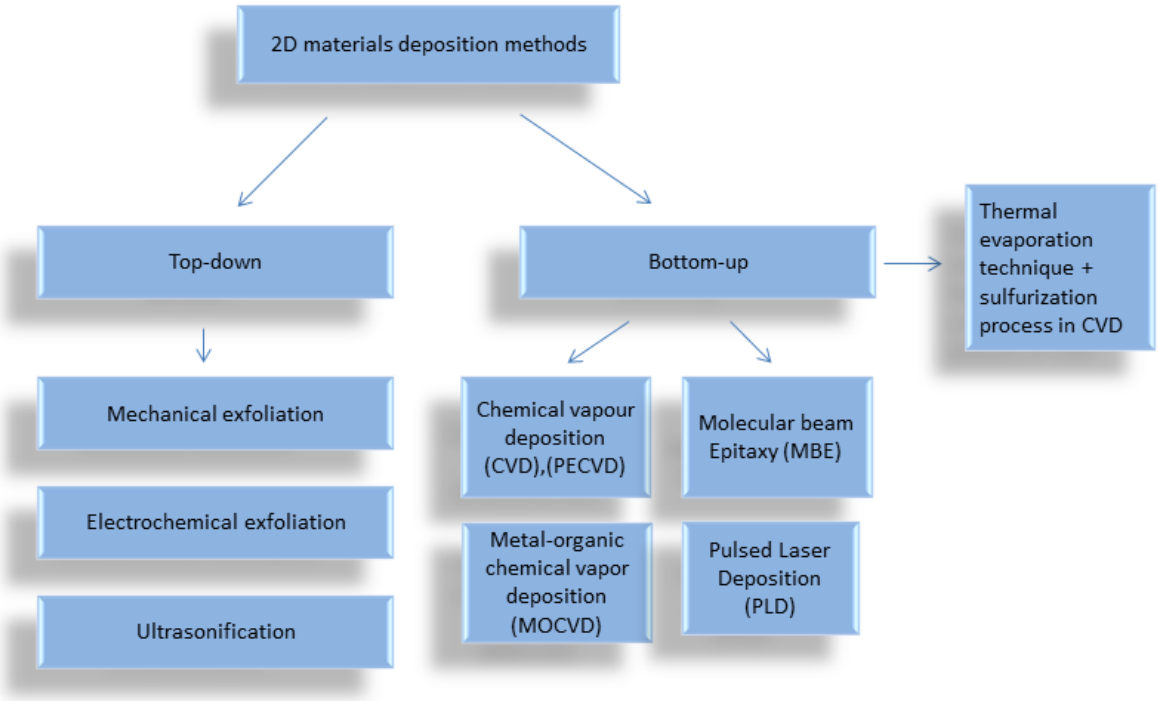

Figure 1.4. The two-dimensional deposition methods.

To summarize, the most commonly used methods for obtaining the two-dimensional few-layers and monolayers can be grouped into two major categories:

a) Top-down methods, which include the monolayer exfoliation from bulk vdW crystal. A few representative top-down strategies are: tape exfoliation, metal exfoliation, intercalation, and liquid mediated exfoliation. During exfoliation, the interlayer vdW bonding in the bulk crystal is overcome by external mechanical forces. Tape or metal thin film-based exfoliation mechanically cleaves the bulk crystals and produces few-layers and single monolayers.

b) Bottom-up methods, which based on using the molecular precursors to formation the 2D crystal networks. CVD crystal qualities are to date inferior to tape exfoliation due to the higher defect densities.

Nowadays, mechanical exfoliation remains one of the most important techniques for material study and creating the test devices.[36-47] Therefore, mechanical exfoliation is the most popular method to study the TMMCs and TMDCs materials and their further application in microdevices. The main advantage is to obtain thin layers with high crystal quality, low quantity of defects and excellent electronic and optical properties.[41] Another advantage is the possibility of applying the exfoliated flakes to various substrates and fabricated photonic structures. Mechanical exfoliation, also known as micro-mechanical exfoliation, uses small mechanical forces during the process. In bulk crystal, each monolayer is held together by weak vdW forces. During exfoliation, the vdW forces between adjacent

layers are breaking and it is possible to obtain the single monolayer (1-L) with thickness of about 0.65 nm. Mostly, bulk MX_2 crystals are indirect bandgap semiconductors, but when the thickness is reduced to 1-L, the bandgap becomes direct.[34-35]

The polydimethylsiloxane (PDMS) gel film transfer technique was applied for all fabricated samples.[36-37] The exfoliation has been entirely carried out in Clean Room laboratory. For mechanical exfoliation of MX and MX_2 flakes, the Schubert tape and commercial viscoelastic PDMS stamp (Gelfilm by Gelpak) were used, see Figure 1.5. The bulk MX and MX_2 crystals were supplied by 2D semiconductors and HQ graphene companies (Figure 1.5a). During mechanical exfoliation, the top covering film of the PDMS gel was removed and the free-standing gel film was carefully placed on a glass slide. In turn, a piece of tape was used to move the flakes on a stamp, see Figure 1.6. Later, thin flakes on PDMS were checked by optical microscope and the monolayers and few-layers were selected for further transfer (Figure 1.7). The flake transfer begin from placing the PDMS-glass slide on XYZ stage. By using the appropriate knobs, the focus is set on the flake and transfer process can be observed. During transfer, PDMS moves down to the sample and sticks to the target substrate. After the flake has been transferred to the substrate, a slide with PDMS moves up and detaches from the substrate. Figure 1.8 shows examples of exfoliated flakes MX and MX_2 layered materials on SiO_2 glass slide.

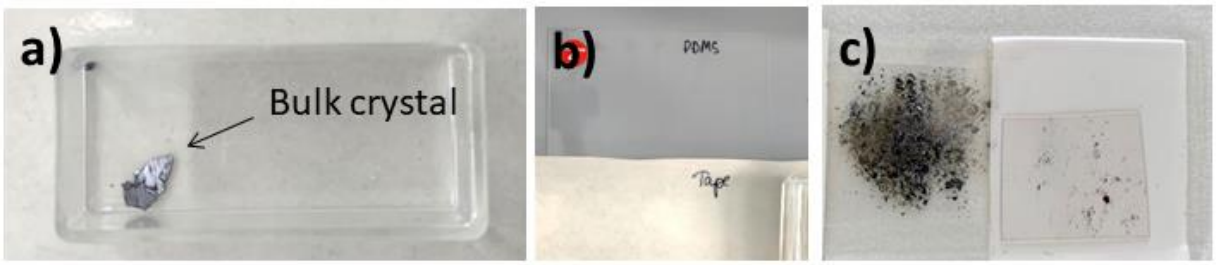

Figure 1.5. Materials used for mechanical exfoliation: a) Bulk crystal; b) PDMS layer and Schubert tape; c) Example of exfoliated flakes from MoS_2 crystal.

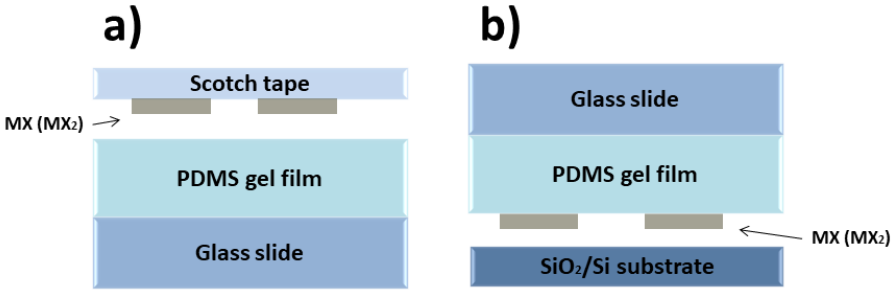

Figure 1.6. Schematic of the PDMS gel film transfer technique: a) Scotch tape with exfoliated MX and MX_2 flakes on PDMS (Gelfilm by Gelpak); b) Transfer of MX and MX_2 flakes from the gel film onto SiO_2/Si substrate.

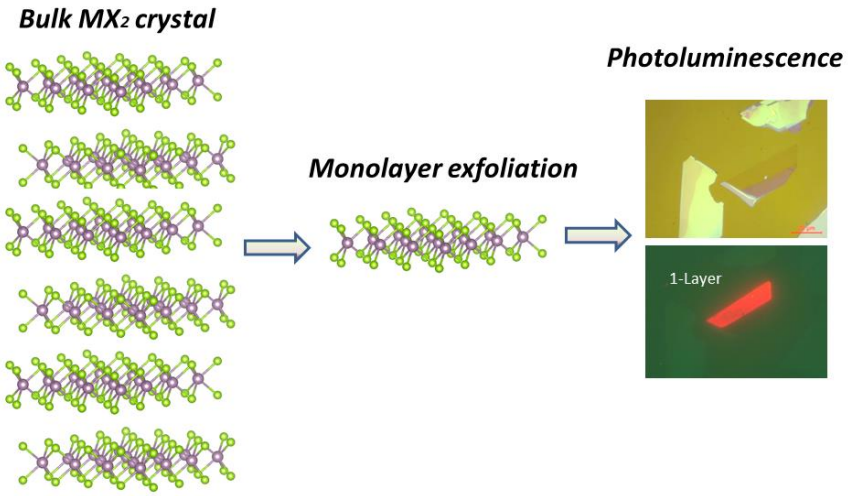

Figure 1.7. Monolayer exfoliation principle from bulk crystal.

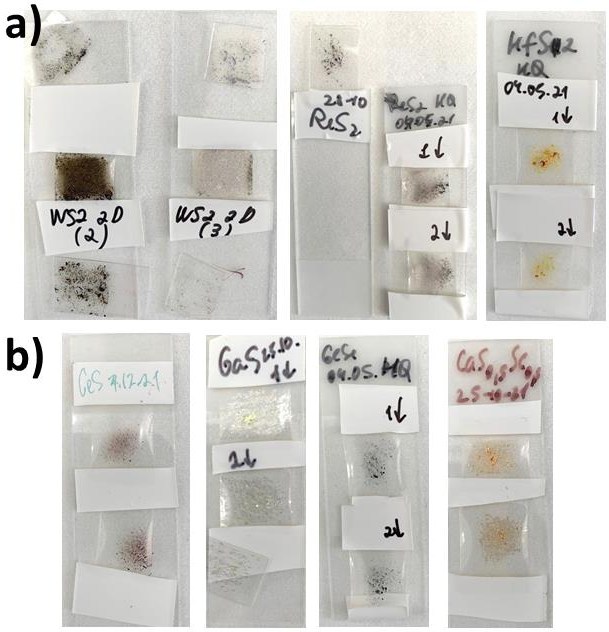

Figure 1.8. Images of exfoliated samples with Schubert tape: a) Samples of exfoliated MX_2 LMs (WS_2, ReS_2, HfS_2); b) Samples of exfoliated MX LMs (GeS, GaS, $GaS_{0.5}Se_{0.5}$).

1.3 Characterization of two-dimensional materials using Raman spectroscopy

Raman spectroscopy is used for study the characteristics of exfoliated materials.[48-54] Raman spectroscopy is the most commonly used powerful tool for 2D materials characterisation, where such material properties as doping type, ability of defects, layer number, interlayer coupling, band structure and Raman spectra can be investigated (Figure 1.9). In this PhD work, only exfoliated thick/thin/few-layers and monolayers from groups MX and MX_2 layered materials were examined by Raman and photoluminescence (PL) spectroscopy.

Raman scattering involves the inelastic scattering of the incident laser light in a 2D material, where the energy of the scattered light either decreases by exciting an elementary

excitation of the solid material (*i.e.* a phonon) or increases by absorbing a phonon. Raman spectra provide the intensity of the scattered light as a function of the energy shift from the incident laser light (measured Raman shift).[48] According to Raman spectroscopy, Raman peaks of lattice vibrations (*i.e.* phonons) in 2D materials reveal several prominent features, which involve the peak intensity, peak position and line shape.[48,50-54] These lattice vibrations give the intralayer Raman modes in high-frequency region and interlayer Raman modes in the low-frequency region (*i.e.* < 100 cm^{-1}).[49-51] In graphene and transition metal dichalcogenides these modes are dependent on the number of layers, where such a correlation is examined for exfoliated 2D materials.

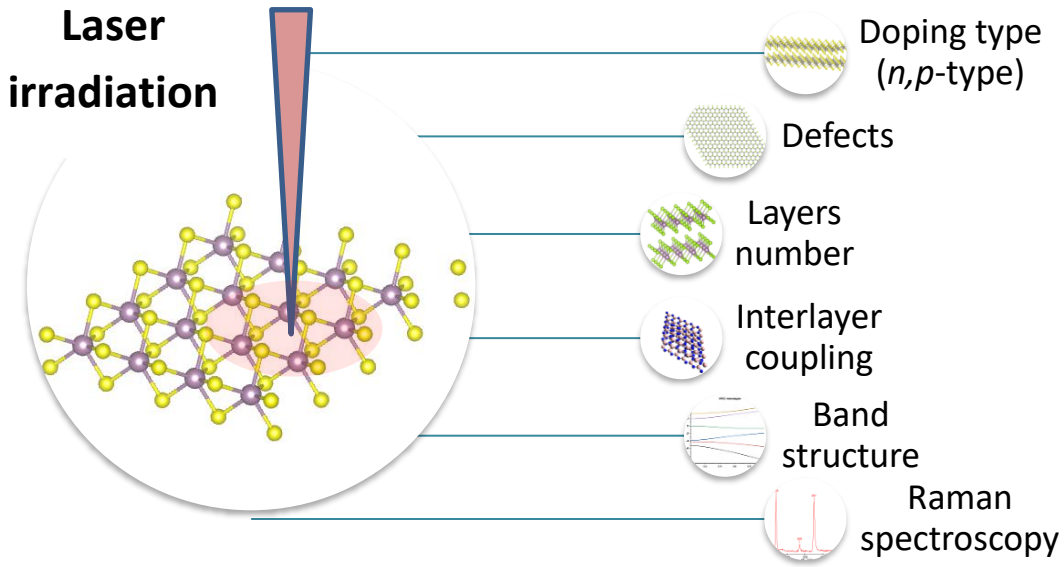

Figure 1.9. Applications of Raman spectroscopy.

1.4 Degradation of exfoliated layered materials under ambient conditions

The MX and MX_2 materials are much more favoured due to their spectroscopic properties and appearance of direct gap in monolayer flakes. These materials founded their application in optoelectronic devices,[55-63] photodetectors,[64-65] solar cells,[66] energy storage,[66-67] spintronic applications,[68] valleytronics.[69] There are a lot of device construction possibilities where such materials can be used but the main obstacle seems to be their stability under ambient conditions. It is reported that stability of these materials declines as the metal moves down to the element group in periodic table, in accordance with the order of the metallic character.[70-71] Understanding the degradation mechanism of layered materials enables the fabrication of more stable low-dimensional semiconductor devices, where the protective encapsulation layer can be added for less stable materials. Therefore, better understanding the sensitivity of two-dimensional materials to oxygen and water molecules after exposure to air provides a new perspective on fabricating the optoelectronic devices with desired properties.

Likewise, the rate of oxidation increases as the chalcogen changes from S to Te, due to the electronegativity of the elements.[70] As the atomic radius of transitional metals increases,

their air stability also significantly decreases and the oxidation mechanisms are quite different from one to another.[72] In general, oxidation processes mostly depend from the reaction between the active species in the air and exposed metal atoms by defects, such as surface vacancies, edges, and grain boundaries.[72-75] Moreover, MX_2 layered materials show larger oxidative reactivity at the edges and surface defective sites.[76-78] It is predicted, that the vacancy defects can reduce the chemical stability of materials.[79-83] For instance, perfect MoS_2 monolayer in room temperature is inert to O_2 molecules, while the monolayer with a sulphur vacancy gets oxidized easily.[83] Such tendency could be observed in similar layered materials.[79,84-86] Surface defects in MoS_2 could lead also to appearing of triangular oxides or triangular etch pits during the in-plane anisotropic oxidation.[80]

The MX_2 layered materials has the different affinity towards oxygen and water, which further induces oxidation of these materials.[70-71] In addition, light can be another essential factor that triggers the oxidation due to electron excitation and charge transfer processes.[70] So far, a lot of research groups presented and explained the oxidation effect in such popular MX_2 as MoS_2,[79-83] $MoSe_2$,[81] $MoTe_2$,[83-88] WS_2,[76,87-91,90,108] WSe_2,[77-78,91-95] WTe_2,[87-88,96-99] HfS_2,[100] $HfSe_2$,[74,100-105] $ZrSe_2$,[105] ZrS_2,[106] ReS_2[107]. Oxidation mechanism in these materials has been studied at elevated temperatures,[89,112-115] under intense laser illumination[124-125] and upon exposure to oxygen plasma or ozone.[91-94,102,111]

Plasma treatment is the way to selective oxidise layered materials, where N layer is reduced to N-1.[91-94,111] Moreover, such oxidation is self-limited and affect only the top-most layer. For instance, MoS_2 few-layer may degrade under UV-ozone treatment, where an oxide layer ($MoSO_2$, MoS_2O) appears on the material surface. After 30 min of UV-ozone treatment, the characteristic Raman peaks for MoS_2 disappeared, which shows that an oxide layer might be eventually formed and 2-L MoS_2 could be thinned to monolayer.[91] Referring to this, layer-by-layer oxidation with controlled oxygen plasma treatment can be used to thin the exfoliated flakes.[90] Kang *et al*. discerned increase in PL intensity and a blue shift of the PL peak positions after oxygen plasma treatment for bilayer and few-layer WSe_2.[91] Because of the low kinetic energy of the oxygen radicals in the remote oxygen plasma, the oxidation is self-limiting. Authors also confirmed that the oxidation will only affect the topmost layer of the WSe_2 flakes. The oxygen ions do not penetrate further into the flake and oxidize the underlying layers, even with longer exposure times. Both the Raman and PL spectra before and after oxygen plasma treatment indicate that the bilayer WSe_2 is converted into the monolayer WSe_2, and the flake is changed from an indirect to a direct band gap semiconductor.

Li *et al.* mentioned that ZrS_2 and HfS_2 can absorb the water molecules, due to the long Hf/Zr–S bonds in comparison with another TMDCs materials.[73] During oxidation in 1T-MoS_2, molecules are adsorbed on the flake surface and dissociate directly at molybdenum atoms at the edge, forming intermediate S-O-Mo structures that facilitate the subsequent formation and detachment of SO_2.[79-82] According to oxidation on MoS_2 surface, there are limited absorption of molecular oxygen due to large energy barrier at room temperature.[81] Hou *et al.* noticed that oxidation of few-layer MoS_2 takes longer than monolayer to fully oxidize,

which means that thicker flakes are more stable than monolayer. The similar dependency was observed in WTe_2 flakes by Fan *et al.*[97] Authors noticed faster degradation in thinner flakes whereas degradation discerned mostly on top surface which can protect inner layers from the further degradation. In HfS_2 material oxidation process is faster in defect sites of the flake.[100] In HfS_2 and $HfSe_2$ layered materials the controlled layer by layer oxidation was also detected.[100-103]

The oxidation rate is highly dependent on the initial adsorption of oxygen molecules on the surface.[105-106] At first, the informed reactive molecular dynamics (RMD) simulations were performed by Yang *et al.*, where the adsorption of oxygen in ZrS_2 leads to a continuous oxidation.[106] In general, the atomic level details of the chemisorption, oxidation mechanisms in MX and MX_2, together with their energetics and kinetics, have not been explored yet, which is an essential requirement in order to successfully fabricate TMDCs-based devices.[105-107] Therefore, further work must be done to continue this issue.

The next parameter that affects the oxidation process is substrate on which the 2D material is exfoliated. For example, $MoSe_2$ on Ni (50 nm) substrate is susceptible to oxidation after several month in ambient, whereas opposite result is founded on Au.[87] Such effect is explained by the presence of a high energy barrier at the heterointerface and charge carrier separation. A few research groups presented the $MoTe_2$ encapsulated with h-BN layer, which helps to keep the Raman peak intensity stable till months.[88-90,109]

Kotsakidis *et al.* explored the role of light by irradiating WS_2 monolayers with visible light at 532, 660, and 760 nm.[110] Authors observed the oxidation process in monolayer for flakes exposed to 532 and 660 nm light (above the threshold necessary for electronic excitation), whereas samples exposed to 760 nm light doesn't show appreciable oxidation. These results indicate that oxidation of WS_2 in ambient conditions requires the photoexcitation which is wavelength-dependent, photoinduced process.

A laser heating has also been applied to oxidize the multiple layers of WSe_2 using a relatively high laser power (up to 12 mW), influencing on top-bottom layers. The oxidized flakes are reported to be stable over weeks. Whereas, the high incident laser power is not suitable for selective layer oxidation, as the irradiated laser strongly affects also the bottom layer.[92-95] It is confirmed that the laser oxidation in the in-plane direction is faster than that in the out-of-plane direction due to the layered structure of WSe_2. Similar to the thermal oxidation process, the laser-assisted reaction with oxygen in the ambient leads to the formation of sub-stoichiometric WO_3 polycrystals.[95] Ahn *et al.* showed that the rapid photodegradation of WSe_2 under air occurred at a laser power of ≥ 0.5 mW and was not observed to any extent at ≤ 0.1 mW.[96] However, in the presence of a water droplet the water-accelerated photodegradation occur even at laser power of 0.1 mW.

Yang *et al.* founded that single-layer WTe_2 degrades fairly fast in ambient conditions whereas 2-L and 3-L are more stable.[98] The 2-L WTe_2 oxidation occur mostly in initial 3 hours of exposure to ambient conditions and 3-L is stable until 2 weeks. Additionally, the self-limiting oxidation in WTe_2 is similar to WSe_2. The main mechanism of degradation of WTe_2 in ambient conditions is oxidation of both W, Te atoms and appearance of oxidation products

such as TeO_2 and WO_x.[97-99] This observation clearly demonstrates that oxidation in ambient conditions occurs only on the top surface of WTe_2, where the main reason of WTe_2 degradation is a low energy barrier for oxidation.[99]

An extreme reactivity has been noted for dichalcogenides with the Hf series. For instance, 1T-$HfSe_2$ oxidised flakes have significant surface protrusions which appears after 4h of oxidation in ambient. The thickness increased simultaneously which was attributed to the expanded interlayer distance due to oxidation.[100-103] Hf atoms react with oxygen molecules and form HfO_X layer. In this case, h-BN passivation could not completely prevent the HfS_2 layer from reacting with oxygen species and suppressed degradation effectively.[84-86]

As the atomic radius of transitional metals increases, their air stability significantly decreases and the oxidation mechanisms are quite different from one to another. Apparently, surface oxidation contributes to the degradation of TMDCs in the case of HfS_2 as well, and the oxidation mechanisms can be very different. In addition, water and oxygen can lead to different oxidation mechanisms and oxidation products. On the other hand, TMDCs like MoS_2 and HfS_2 have been reported to expose the high electrocatalytic activity towards hydrogen production and oxygen reduction based on defective sites. Therefore, understanding the reactivity of the defective sites is the necessary first step to gain insight into the oxidation mechanism and chemically tailoring the properties of TMDCs.

It is found that the oxidation of ZrS_2 and HfS_2 by oxygen adsorption occurs at the defective sites such as surface vacancies and edges.[73] These materials can attract water molecules effectively, due to the long Hf/Zr–S bonds, which provide adequate vicinity for the adsorption of water from the air. The full oxidation process requires continuous reaction with either water or oxygen which may fill the sulphur vacancy site and passivate the defective sites for further reactions. The whole degradation of HfS_2 and ZrS_2 can be divided into three steps in a cyclic order, which are adsorption, substitution, and readsorption, respectively.[73]

Wang *et al.* observed the fully conversion of HfS_2 into the HfO_2 layer in a layer-by-layer with controlled oxidation time and thermal treatment where oxide thickness was controlled by oxidation temperature and heating time.[100] Yang *et al*. in detail reported the analysis about adsorption of oxygen on ZrS_2 surface, followed by amorphization and oxygen transport into bulk, leading to a continuous oxidation.[106]

It is suggested that the energy of the dominant radiative transition increases as the material thickness is reduced. From bulk to monolayer, ReS_2 remains a direct-bandgap semiconductor, its PL intensity increases, whereas the Raman spectrum remains unchanged with increasing number of layers.[107] To sum up, the oxidation process in exfoliated MX and MX_2 layered materials requires a wide range of researches in terms of stability in ambient conditions depending of the number of layers, number of defects, and type of material.

The stability of exfoliated MX and MX_2 layered materials in ambient conditions has not been intensively and systematically investigated so far, therefore this topic is the subject of research in the presented thesis.

2 Sol-gel SiO_x:TiO_y material platform

The traditional Si photonics has shown the great progress in the field of telecommunication (for 1550 nm and 1310 nm) wavelengths. However, Si platform cannot be used for building devices in visible wavelength due to its bandgap (1.1 eV), where the visible light is absorbed and material is non-transparent. Therefore, there is a need to develop the new materials on visible wavelength range. The sol-gel SiO_x:TiO_y (high refractive index of $n \approx 1.80$ at wavelength 632.8 nm) has been used as material platform for fabrication the photonic microstructures due to transparency for frequencies in visible spectrum and low optical losses.[116-123]

Sol-gel SiO_x:TiO_y is a novel platform for developing photonic structures like waveguides, ring-resonators, integrated circuits,[116-117] grating couplers[118] and further their integration with two-dimensional materials. The high refractive index of the sol-gel layers allows for a wide application in integrated optoelectronics. Moreover, sol-gels based on metal oxide are the most resistant to acids, organic solvents and bases. Therefore, sol-gel on metal oxides SiO_x:TiO_y was used as material platform for fabrication the microphotonic components like waveguides, microdiscs and further device creation.[123]

The two compound SiO_x:TiO_y films were fabricated via the sol-gel method and dip-coating technique in Lukasiewicz Polish Centre for Technology Development as part of the project implementation. Sol-gel layers are produced form the liquid sol-gel SiO_x:TiO_y by dip-coating technique. During the dip-coating, the withdrawal speed (*v)* from the sol was controlled, having the influence on the thickness of the obtained sol-gel film (Figure 2.1). In solution, as sol precursors were used tetraethyl ortosilicate (TEOS), tetraethyl ortotitanite (TET) and ethyl alcohol (C_2H_5OH).

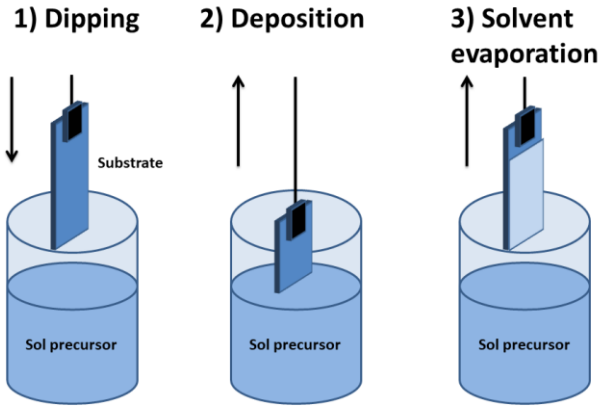

Figure 2.1. Sol-gel dip-coating fabrication method.

The received film thickness and refractive index were determined by ellipsometry measurements. The substrate SiO_2/Si was used to deposit sol-gel layers. After applying the sol-gel, the layered samples were annealed in 500°C for 1h. A detailed description of the sol-gel preparation method is reported in Ref.[116-117]

Once the sol-gel platform has been prepared, the next step is the fabrication of photonic microstructures. The sol-gel layers represent the ideal material base for fabrication photonic waveguides for the VIS-NIR spectral range, due to low propagation losses (0.3 dB/cm[116]), high optical quality and good transmission properties. Additionally, single mode waveguides with desired dimensions can be fabricated from a prepared sol-gel layer.

The hybrid integration of manufactured structures with two-dimensional materials is a new direction of research and a task to be implemented in this PhD study. First of all, such integration will allow the construction of new microdevices with interesting characteristics (Figure 2.2).

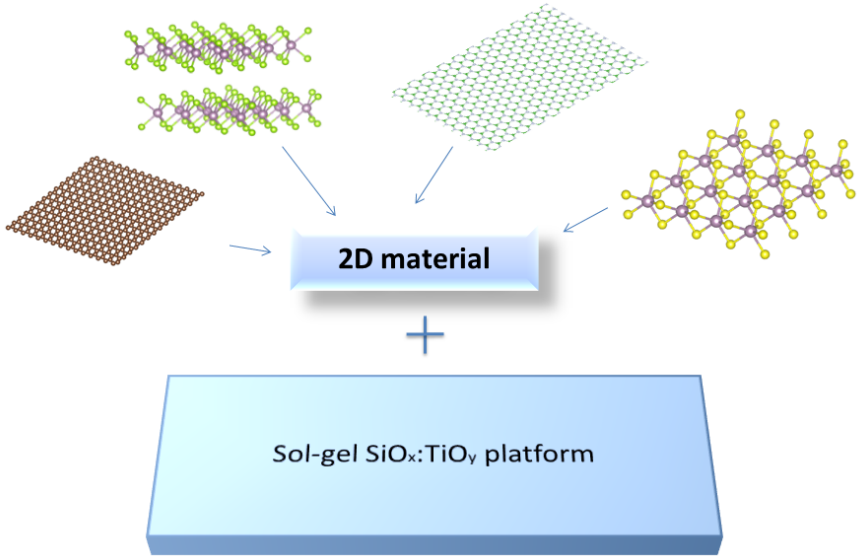

Figure 2.2. Hybrid integration of layered materials with sol-gel SiO_x:TiO_y platform.

3 Methods and techniques for microdevice fabrication

3.1 Techniques for fabrication sol-gel microstructures

For the fabrication of photonic structures on previously prepared sol-gel SiO_x:TiO_y layers, the following techniques and processes have been conquered and applied: photolithography, wet and dry etching, metal evaporation. Such techniques were used in CleanRoom laboratory (ISO-5/6) under the highest purity. The following sections describe each technique in detail.

3.1.1 Photolithography

Photolithography is a base process for fabrication microsystems (MEMS).[124] The photolithography defines and transfers a designed pattern on photosensitive polymer – photoresist (Figure 3.1). Photolithography consist from the three steps: substrate coating with photoresist; exposure the resist layer through patterned mask by UV light; developing the pattern. The photolithography process starts from the task specification (which structure

we want to obtain at the end of the process), preparation of CAD design for photolithography mask and further mask fabrication. For our purposes, mask was produced by Compugraphics (USA) with design created at KLayout software. The next step is the lithography process starts from substrate cleaning; substrate coating with photoresist; photolithography (exposure the photoresist) and later developing (washing the unexposed area). The next following steps include sample characterisation, where the received pattern is analysed and the substrate is divided into smaller samples.

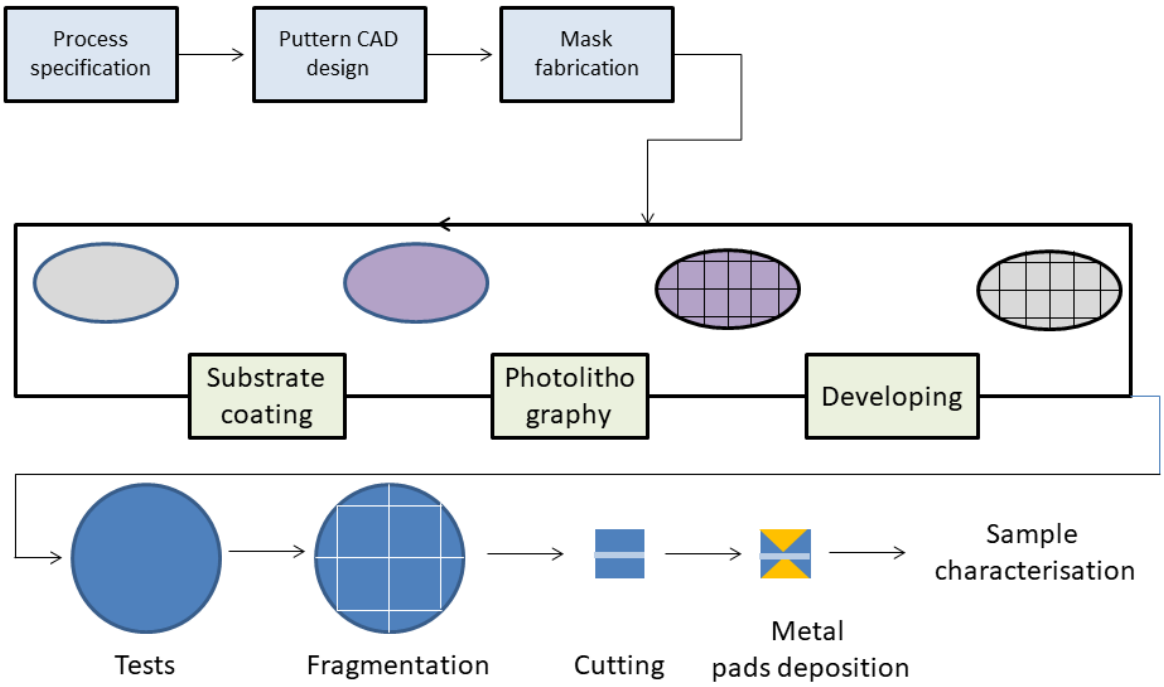

Figure 3.1. Photolithography process circle.

3.1.2 Wet and dry etching

After the photolithography process, samples were wet or dry etched, depending from microstructure application.[125-126] Wet etching is a bath solution process, where the sol-gel layer is etched selectively (Figure 3.2). As etching solution was used the buffered oxide etch (BHF). Etching is carried out according to the reaction (1):[125]

$$SiO_x{:}TiO_y + BHF \rightarrow H_2 + SiF_6 + TiF_6 + 2H_2O \quad (1)$$

The wet etching was applied to fabrication of such microphotonic structures as microdiscs due to the possibility of obtaining the appropriate microdisc shape. The wet etching of structures was carried out for the sol-gel SiO_x:TiO_y layer with a thickness of 0.2-0.3 µm. This process can only be used for etching structures on Si and SiO_2/Si.

Dry (plasma) etching represents the combination of several physical processes, which include the chemical etching by reactive species (spontaneous etching), ion assisted chemical etching and physical sputtering. Etching process is very anisotropic, selective and

high resolution structures were obtained. Due to this, plasma etching was applied to fabrication the photonic waveguides. For dry etching, the gas mixture CHF_3+ Ar + O_2 was used. The etching rate of sol-gel is 95 nm/min. The plasma etching of sol-gel SiO_x:TiO_y occurs on a few reactions (2-3):[125]

$$CHF_3 + SiO_x \rightarrow SiF_4 + CO + CO_2 \quad (2)$$

(reaction strongly assisted by the temperature of the Si wafer).

$$CHF_3 + TiO_y \rightarrow TiF_4 + CO + CO_2 \quad (3)$$

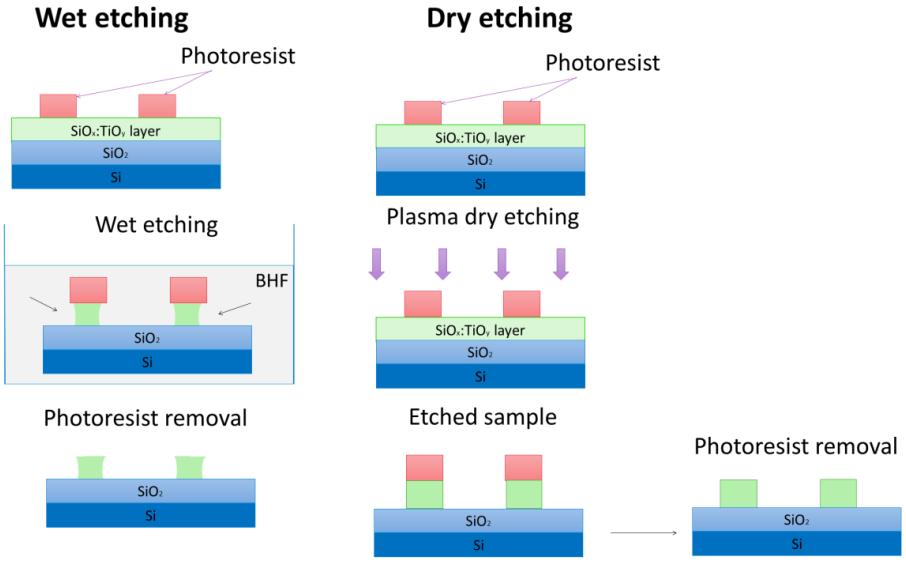

Figure 3.2. Schematic of wet and dry etching processes.

3.1.3 Nanoimprint lithography (NIL)

Nanoimprint lithography (NIL) is technique for fabrication the photonic microstructures such as waveguides, ring resonators and gratings form liquid sol-gel. The main advantage of this technology is that no special equipment is needed. The simplicity of NIL lies in the fact that it is easily reproducible and the fabrication of microstructures is etch-less. However, there are parameters that must be controlled during process: applied force during imprinting, amount of liquid sol-gel; optimization of annealing temperature after sample fabrication. NIL allows for resolutions below 100 nm without the light diffraction problems associated with conventional lithographic techniques. The pattern creation mechanism is based on the mechanical deformation of the polymer mask, which is performed by pressing. The first stage of the NIL process involves preparing the polymer mask with microstructures (stamp). Sol-gel structures obtained by imprinting the stamp in the sol-gel layer. Then the structures are hardened in an oven at 500°C during 1h.

The main advantage of NIL is possibility of applying the stamp multiple times (up to 5 replicas), which also helps to save time on producing the new stamps.

3.2 Metal contacts preparation

Two-dimensional transition metal monochalcogenides (MX) and dichalcogenides (MX_2) are promising materials for the creation of thin optoelectronic devices.[127-130] However, low-resistance metal contacts preparation for these devices require a lot of experimental work in contact improving.

The most important technique for fabrication the metallic contacts to semiconductor devices is physical vapour deposition (PVD). This method consists of using an appropriate vacuum chamber, from which a sufficiently low concentration of air particles is obtained by pumping out the chamber. Vapor deposition of thin layers is carried out at pressures of 10^{-7} mbar or lower. Vaporization relies on heating the vaporized material to temperature at which the partial pressure of its vapors is higher than the pressure in the device. In PVD technique, the metal is melted by using an electron beam. After reaching the appropriate melting temperature, material is evaporated on sample. The gas pressure near the substrate should be low enough to keep its surface free of adsorbed gases. Bringing the steamed material to the boiling point is carried out by heating with an electron beam. Due to heating with an electron beam it is possible to obtain layers of hard-melting materials like platinum (Pt) and palladium (Pd).

The contact quality and contact resistance are determined by the contact metal. When the metal is deposited on a semiconductor, the Schottky contact creates a potential barrier represented by Φ_B, depending upon the work function of the metal and the electron/hole affinity of the semiconductor. The Schottky barrier height for electrons can be increased by increasing the work function of the contact metal. On condition, when the metal and the semiconductor are brought into contact, the Fermi level matching invariably causes the charge to flow from one side to the other and a dipole layer is built up at the interface.[131] The depletion or accumulation layer is formed at the interface of the semiconductor and metal. Depending on the *n*- or *p*-type semiconductors, the downward or upward band bending at the interface occurs by the charge transfer process and Fermi level alignment. The lateral interfaces between the layered materials and different metal electrodes already was investigated for GeSe,[133-136] GaSe,[134,136,138] GeS,[134,136,139] SnS,[134,136,140-141] SnSe,[134,136,142-143] and MoS_2[137,144-154] $MoSe_2$,[137,144,146,148-153] and WSe_2,[137,144,146,149-156] WS_2,[137,144,146,149-156] WTe_2,[137,144,146-156] $MoTe_2$.[137,144,146,149-155]

The fabrication of low-resistance metal contacts is the most important task during the device fabrication.[146-162] Here, the high contact resistances between the metals and the two-dimensional materials significantly degrade the performance of fabricated devices on these materials. The one way to lower the contact resistance is to select a proper work-function metal. Against, the detailed physics of the interface between the metal and the MX (MX_2) layered materials plays an important role, which should be understood to achieve low contact resistances. The ohmic contact (non-rectifying) appears when $\Phi_B << K_BT$ (K_BT = Boltzmann constant and T = absolute temperature), with linear current–voltage (I–V) characteristics. In other ways, the contact leads to Schottky contact of a rectifying junction

with non-linear *I*–*V* characteristics. In practice, the Schottky contact with a non-zero interface contact resistivity appear between an undoped semiconductor and metal.

At the metal-2D semiconductor it is difficult to achieve ohmic contacts due to tunnelling and weak dependence of depletion width from the carrier concentration. The substrate on which the 2D semiconductor was transferred also influences on metal-semiconductor junction where the substrate can create the interface states and affect the carrier injection. Moreover, substrate can induce rather *n*-type doping to the 2D semiconductor. Therefore, *p*-type doping is difficult to obtain.[150]

Thus, when selecting the appropriate metal for 2D semiconductor, the few approaches must be taken into account:

1) Avoiding the highly reactive metals which can react with the semiconductor.

2) Selecting a low vaporization temperature metal as the kinetic energy of evaporated atoms is low and therefore damage of 2D semiconductors during the metal deposition process is minimized.

3) The work function of the metal should match the conduction band of the 2D semiconductor for electron transport and the valence band for hole transport.

4) Selecting metals with appropriate work functions matching with semiconductor band edges to lower the barrier for carrier injection. Therefore, *n*- and *p*- type devices based on 2D semiconductors rely on selecting the high and low work function metal for contacts deposition.

The top, edge and combined contact configurations are possible during the contact preparation (Figure 3.3).

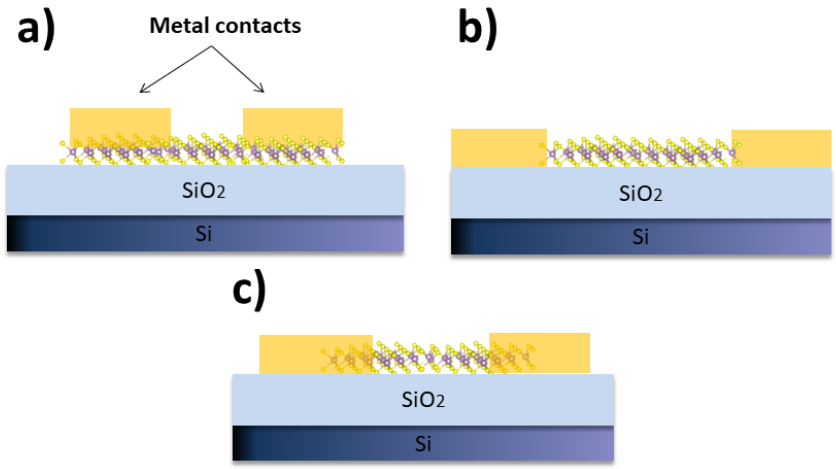

Figure 3.3. Schematic contact configuration: a) Top contact; b) Edge contact; c) Combined contact.

The edge contacts are more desirable, where for this contact type the favourable in-plane carrier injection and smaller tunnel barrier width are noticed. The edge contacts can lead also to the low contact resistance. In case of top contacts, a wide tunnel barrier and the unfavourable out-of-plane carrier transport is noticeable. For this configuration, the contact resistance mightily depends on the contact area of metal-semiconductor with weak coupling

between them. In this study, the top contacts were deposited on bulk crystals and the combined contacts on the exfoliated thin and thick flakes.

4 Photonic microstructures and microdevices

It is possible to enhance the potential of 2D-based optoelectronics by their integration with photonic structures such as waveguides (WGs), resonators, microdiscs, microlasers, photonic structures *etc.*[163,170-171] The integration of photonic structures like waveguides, ring resonators, integrated circuits with MX_2 materials allows for fabrication the novel photonic devices with strong light-matter interaction.[164] For instance, monochalcogenides from group IV-VI are characterised by high chemical stability, low toxicity and giant potential in optoelectronics, piezoelectrics, photodetectors, sensors, Li-batteries and thermoelectrics.[27-35] Photovoltaics is the main prospective application of group-IV LMs which act as absorbers.[30]

Among photonic structures, microdiscs are to be widely used in hybrid optoelectronic circuits. They mainly operate in integrated optical components for:[164]

1) Multiplexing and demultiplexing of channels. Microdisc can perform a wide range of optical signal processing functions such as filtering, splitting and combining of light, switching of channels. Such multiplexer it is like wavelength-selective filter that can combine or separate the different wavelengths of light by carrying, controlling and light manipulating in optical transmission systems.
2) Micrometer-size ring resonators. Ring resonator consist of a bus waveguide which coupled to a micrometer-size microdisc. With such resonator the characteristic size-dependent frequency spectrum of the ring allows only selected wavelength channels to be transmitted or shifted to another waveguide. By integrating arrays of such resonators on a single optical chip, the realization of complex functions would be possible.
3) Microdiscs in terahertz radiation. Terahertz radiation has promising applications in security and medical diagnostics. Therefore, such application is require the development of compact, low-power and high-quality terahertz lasers.

The main conception in fabrication of microdiscs is observation and measurement the whispering gallery modes (WGM).[165-171] WGM modes represented as closed-trajectory rays which confined in microstructure by partial reflections from the walls. Such WGM structures have already found their application in areas such as optoelectronics and biological science.[169-171]

The planar waveguide (WG) is the main component in integrated optical circuit which interconnect the main elements.[169] These structures guide the light across an entire circuit. There are a few cross-sections of waveguide – strip and rib waveguides. In this thesis we will work only with strip waveguides, where the optical properties like propagation of electromagnetic wave, mode shape and effective refractive index depends on the waveguide width *(W)* and thickness *(H).*

Photodetectors (PD) are the optoelectronic devices that convert optical signals to electrical and have a wide range of applications in photonic circuits, signal processing, imaging and sensing systems. Detectors are an excellent basis for their integrating with 2D materials. The electrical characteristics of such integrated devices have already been presented by many research groups. For these hybrid devices, a protective layer should be added to avoid the material degradation. As a solution to maintain device characteristics, the thin film with PMMA or thin Al_2O_3 can prevent the electrical property degradation.[172-177]

EXPERIMENTAL PART

5 Two-dimensional materials as active part in microdevice fabrication

In this work, each sample was characterized by scanning electron microscopy (SEM), optical microscopy and Raman spectroscopy. Optical images are obtained by Leica optical microscope using a 50× objective lens. The morphologies of the sample surfaces were investigated using a FEI Helios 660 Scanning Electron Microscope in a high-vacuum. The SEM micrographs are taken at 2 kV accelerating voltage with a current of 25 pA. For measuring the Raman spectra and PL map, the confocal micro-Raman spectrometer (WiTEC) with grating 600 g/cm and laser of 532 nm wavelength was used. Laser power of 0.05 mW was chosen to avoid the sample heating. Measurements were carried out in ambient air at room temperature. The Raman signal was collected in a backscattering configuration with a resolution down to ∼ 200 nm. The spectra were taken with the same accumulation time. The repeatability of measurements and signal intensity were calibrated according to the Si peak before recording the each spectrum. The PL spectrum was obtained in the same spectrometer with grating of 300 g/cm. The laser beam with diameter of ≈ 1 µm was used with a 100× objective lens.

5.1 Mechanical exfoliation of MX and MX_2 materials

After transferring the 2D material to the target substrate (SiO_2/Si), the size estimation was performed for each flake. For better flake identification, each target substrate was structured by a laser with mesh design (Figure 5.1). The longest lateral dimension of the exfoliated flakes was obtain between 40 to 120 µm. The thin and few-layered flakes with large surface area were identified and further used for material study and device fabrication. Table 1 shows the summary of the difficulty of exfoliating the 2D materials. The easy and medium exfoliation was noticed for all TMDCs materials, whereas these flakes could be thinned down to monolayer. In case of TMMCs, mechanical exfoliation was more difficult and monolayers were hard to obtain.

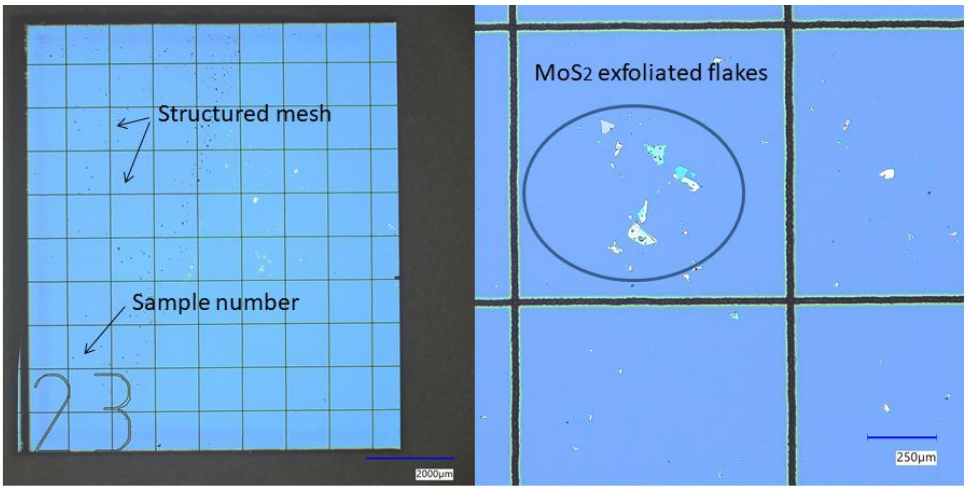

Figure 5.1. View on SiO_2/Si substrate with structured mesh and exfoliated MoS_2 flakes.

Table 1. Summary of the difficulty of exfoliating the 2D materials.

Material	Hard	Medium	Easy
TMMCs			
GeS	x		
GeSe	x		
GaS	x		
GaSe	x		
TMDCs			
MoS_2			x
WS_2			x
WSe_2			x
HfS_2			x
$HfSe_2$			x
ZrS_2		x	
$ZrSe_2$			x
ReS_2	x		
$ReSe_2$	x		

5.2 Setup for mechanical exfoliation and transfer of two-dimensional materials

The existing commercial transfer setups for 2D materials are very expensive. Mainly, the high price is associated with ability of precision optics and expensive mechanical components. For example, the experimental setup from HQ graphene starts from 20890 EUR. To reduce costs, the best solution is creating the own transfer system according to the needed application.[35-36] For our research, a special low-cost experimental setup was created to transfer the thin flakes on a target sample (Figure 5.2). The cost of creating the our experimental setup is only 2808 EUR.

The our experimental setup consists from such elements:

- 16 mm Cage Rotation Mount for Ø1/2" Optics (Thorlabs);

- Pitch and Yaw Accessory Tilt Platform with Micrometers (Thorlabs);

- 515 nm, 10 mW, Ø5.6 mm, A Pin Code, Laser Diode (Thorlabs);

- Adjustable Collimation Tube with Optic for Ø5.6 and Ø9 mm Laser Diodes, f = 3.1 mm, NA = 0.68, AR Coated: 350 - 700 nm (Thorlabs);

- two stages XYZ with 3" Dovetail Rail, 250 mm Long (Thorlabs);

-optical metallurgical microscope Delta Optics with camera (DLT-Cam Pro 6.3 MP);

-laser diode driver model 505B, Newport.

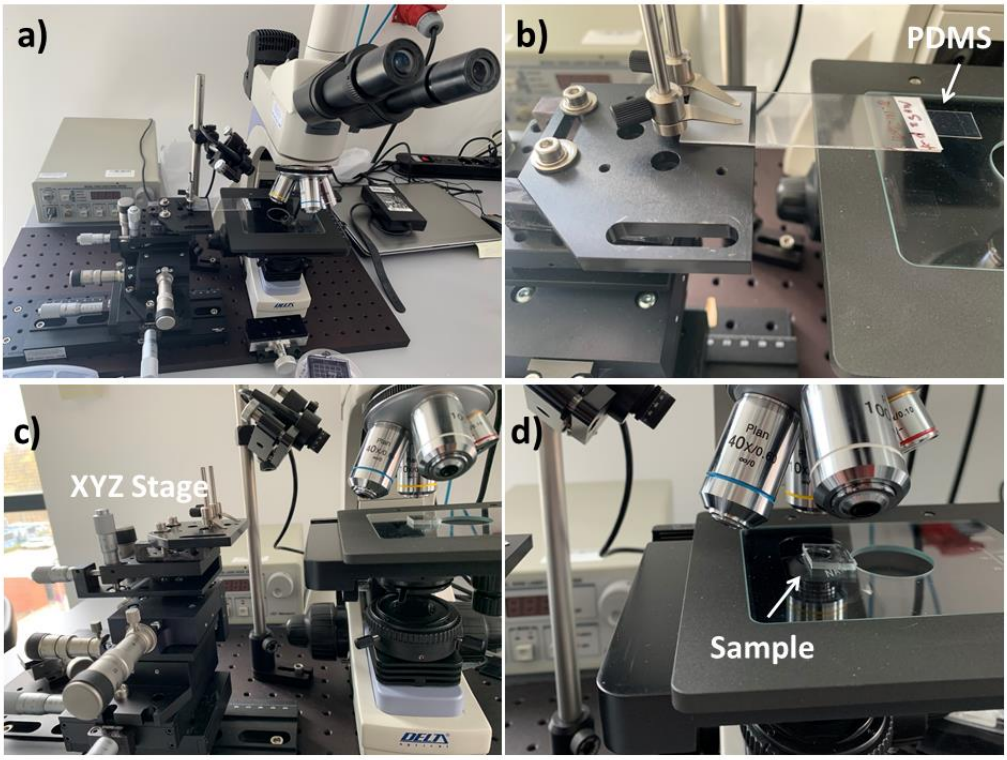

Figure 5.2. Images of 2D material transfer setup: a) View on the transfer setup; b) Stage with PDMS and glass slide; c) View on the XYZ stage and laser diode; d) Zoom on a sample.

During the device fabrication processes, the transfer setup was used on the one hand to transfer the thin flakes from PDMS stamp and further to transfer the MX (MX_2) flakes on the previously fabricated sol-gel waveguides (Figure 5.3). Additionally, setup was used to make the heterostructures like WS_2/h-BN/WS_2. The main advantage of the transfer system is the presence of two lighting modes, which are very useful for achieving optical contrast during transfer – reflected light mode *(RL)* and transmitted light mode *(TL).* By using transmitted light, the flake contrast during transfer is more pronounced and sharp, owing to better identification of flake thickness (Figure 5.3c). The presence of a laser diode in the setup and power supply allows for checking the photoluminescence from exfoliated MX_2 monolayers and few-layers.

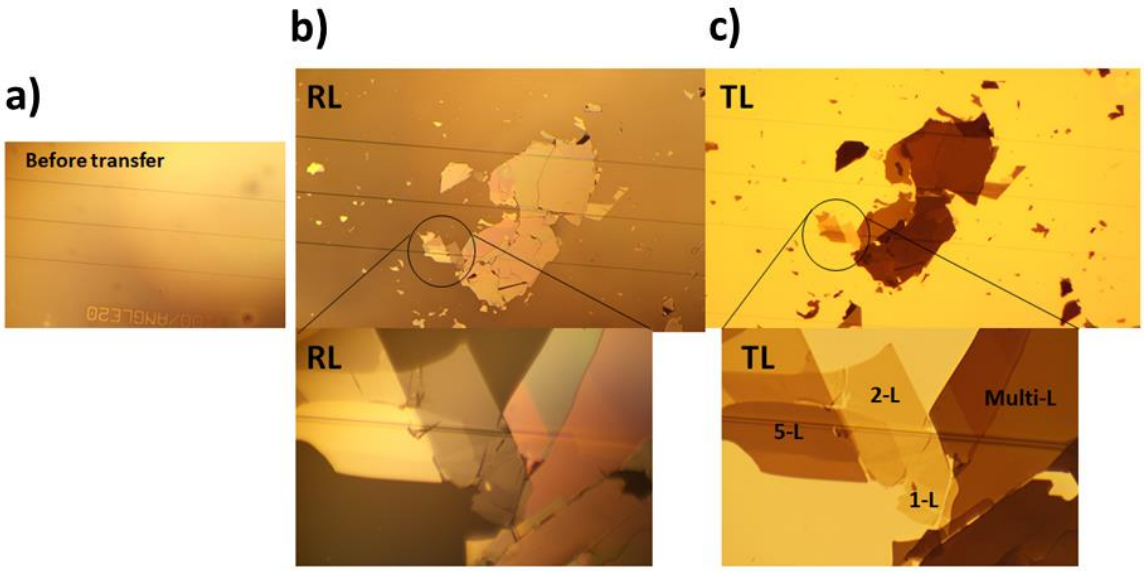

Figure 5.3. Images form optical microscope of: a) Waveguide before flake transfer; b) Transferred flakes on sol-gel waveguides in *RL* mode; c) Transferred flakes on sol-gel waveguides in *TL* mode.

5.3 Setup for graphene transfer

In work, graphene was used as a transparent electrode and to create heterostructures from two-dimensional materials, further device fabrication. For the described application, graphene transfer has been improved. An example of using graphene as a transparent electrode is described in the publication ***P4***.

The graphene synthesis was performed by the research team of PORT Lukasiewicz Research Institute. Graphene layers were synthesized through the chemical vapour deposition (CVD) on a copper (Cu) foil (purchased from Alfa Aesar), which was used as catalytic substrate. The electrochemical delamination method was applied to transfer the Gr layer from the Cu substrate directly on a target substrate (silicon dioxide on silicon (SiO_2/Si), aluminium dioxide (Al_2O_3), gallium nitride (GaN)). This transfer method allows for obtaining the large Gr layers, non-destructive, low-cost and highly efficient. Moreover, the purity of the transferred Gr is higher, compared to chemical transfer methods.[178-183]

During electrochemical delamination, a polymer poly(methylmethacrylate) (PMMA, molecular weight 950 kDa, AR-P 679.04) layer was spin-coated on Gr/Cu samples and used as protection and support layer during the transfer. Next, PMMA/Gr/Cu sample was connected to the electrode and immersed in electrolyte. Solution of potassium chloride (1 M) was used as electrolyte in the electrochemistry process. During the electrochemical etching, voltage from DC supply is applied to the PMMA/Gr/Cu cathode and a glassy carbon anode, which is immersed into electrolyte. The Gr/Cu electrode is cathodically polarized at -3 V, and hydrogen bubbles occurs at the Gr/Cu interfaces due to the reduction of water (Figure 5.4). The target substrate was cleaned using the sonification during 5 min in acetone, followed by immersion in isopropyl alcohol and drying by N_2 gun. After the copper layer

moves away from the graphene, the PMMA/Gr film was transferred on a target substrate and baked at 353 K for 5 min. In the final stage, PMMA layer was removed with acetone.

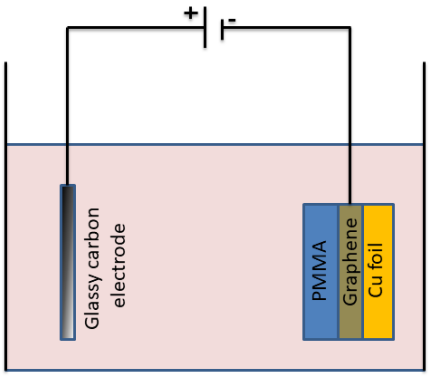

Figure 5.4. Schematic of experimental setup for graphene electrochemical delamination.

The 1-L and 2-L graphene layers were transferred on GaN, AlGaN, SiO_2/Si substrates (Figure 5.5-5.6). The thickness of transferred graphene layer was varied from one to four layers.

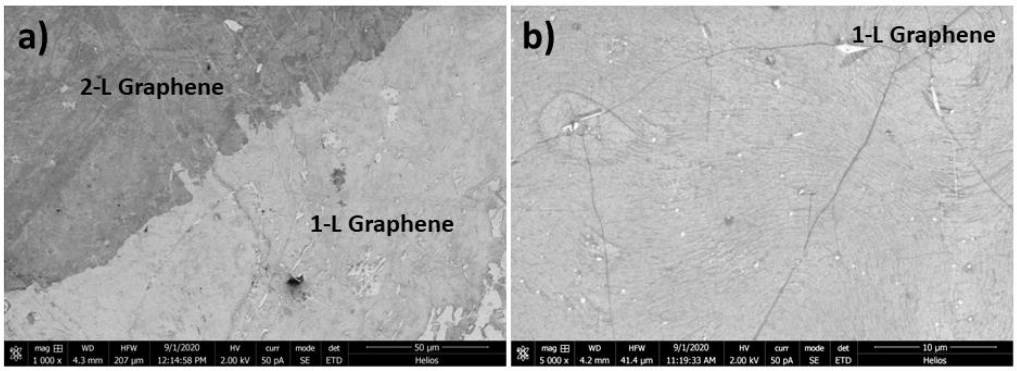

Figure 5.5. Graphene on GaN substrate: a) View on contact boundary of 1-L and 2-Layer; b) Zoom on Gr 1-Layer.

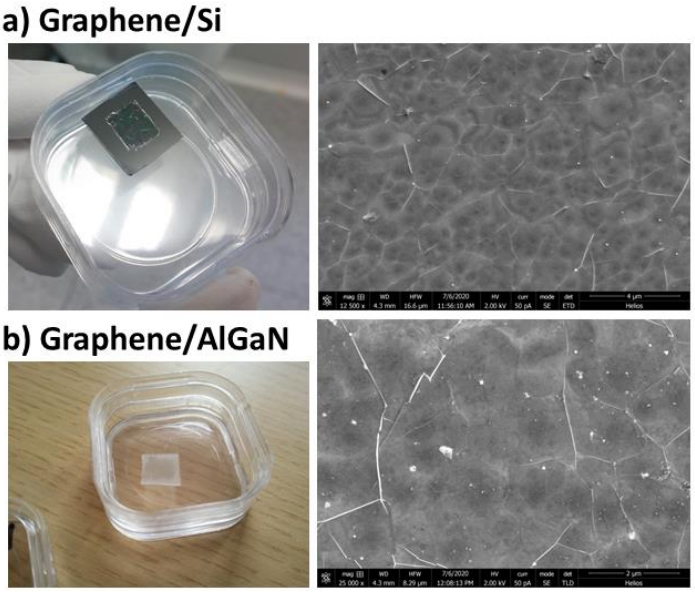

Figure 5.6. Examples of transferred Gr layer on: a) Si substrate; b) AlGaN substrate.

5.4 Two-dimensional heterostructures

A few heterostructures were fabricated to study their optical properties: graphene/WS_2, graphene/MoS_2 and WS_2/h-BN/WS_2, where h-BN is exfoliated hexagonal boron nitride. In the first heterostructures, graphene was used as a transparent electrode.

5.4.1 Graphene/WS_2 heterostructure

For heterostructures fabrication, WS_2 mono- and few-layer was exfoliated on a PDMS and transferred on SiO_2/Si substrate. Next, 1-L Gr was removed from the Cu foil and layer continuity was examined using an optical microscope (Figure 5.7). We see, that after the transfer Gr layer is continuous at least of 95% on the all sample. The Raman and PL spectra were measured for WS_2 monolayer, Gr and Gr/WS_2 (circles area on Figure 5.7), see Figure 5.8.

Raman spectra represents peaks both from WS_2 and Gr, see Figure 5.8. For WS_2 monolayer, the two peaks are visible at 352 cm^{-1} (E^1_{2g}) and 419 cm^{-1} (A_{1g}). For graphene, the *G* mode at 1349 cm^{-1} and *2D* mode at 1587 cm^{-1} are observed (Figure 5.8b). The PL for WS_2 is located at 1.95 eV (Figure 5.8d). In graphene spectrum, changes in the *G* peak positions and shape of the *2D* band indicate the number of graphene layers. Similar in MoS_2 and WS_2, the positions of the E^1_{2g} and A_{1g} lines indicates the layer thickness.

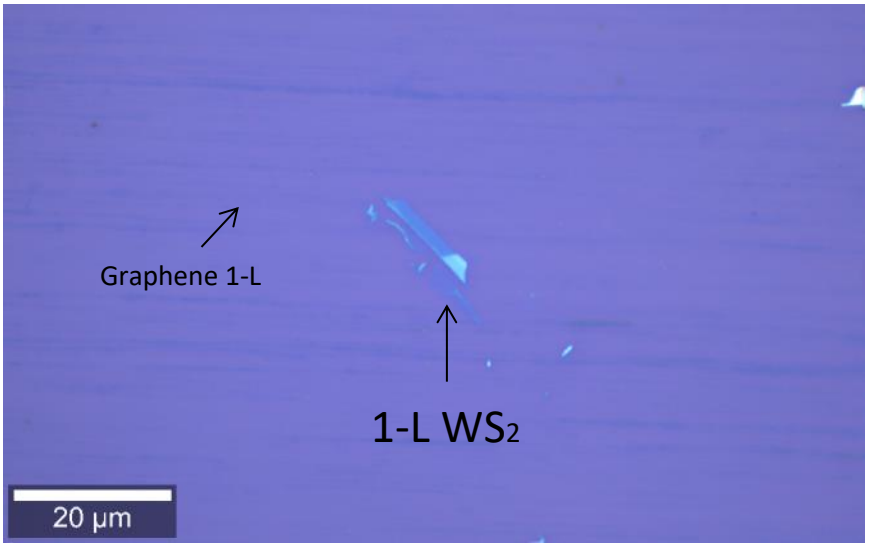

Figure 5.7. Graphene 1-L on exfoliated WS_2 monolayer, substrate SiO_2/Si. Image from optical microscope.

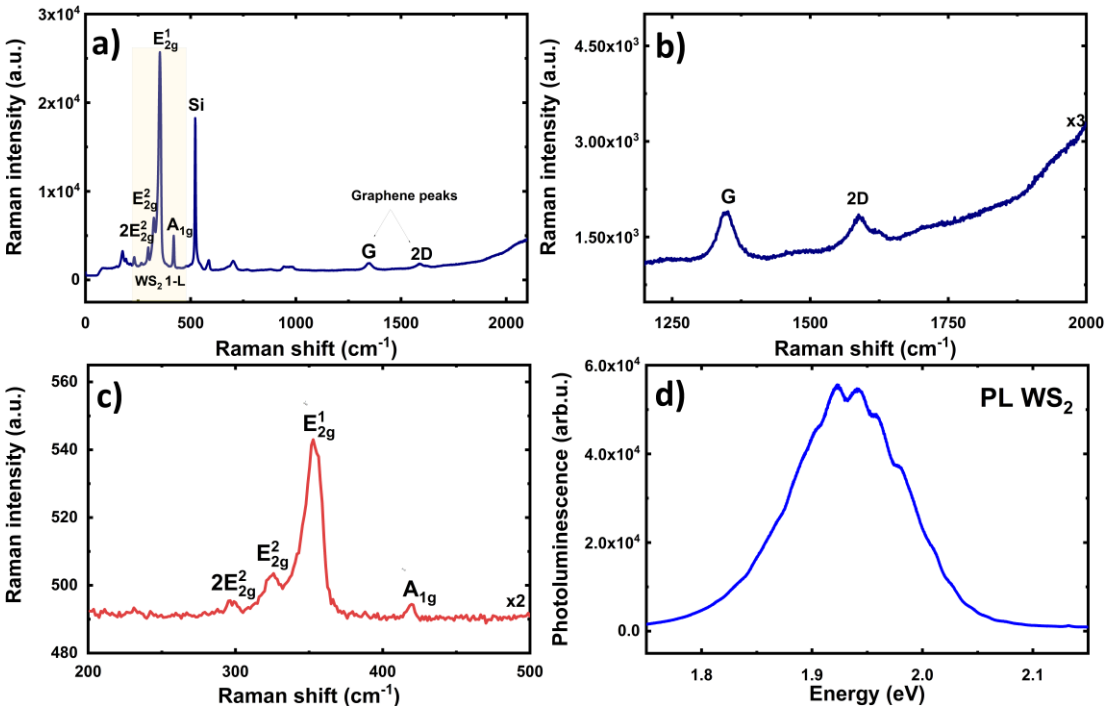

Figure 5.8. a) Raman spectrum for 1-L graphene on WS_2 monolayer; b) Zoom on Raman spectrum for 1-L graphene; c) Zoom on Raman spectrum for WS_2 monolayer; d) Photoluminescence of WS_2 monolayer.

5.4.2 Graphene/MoS_2 heterostructure

The similar fabrication technique was used for obtaining the graphene/MoS_2 heterostructure. Transferred MoS_2 flake consist from monolayer to thick flake (Figure 5.9). A few contaminations is visible on graphene, but Raman spectrum was detected from clean area (blue circle on Figure 5.9). Raman spectrum for this heterostructure is represented by monolayer MoS_2 peaks and graphene (Figure 5.10). For MoS_2 monolayer a two dominant peaks are visible at 385 cm^{-1} (E^1_{2g}) and 407 cm^{-1} (A_{1g}), see Figure 5.10a. The maximum of PL spectra is located at 0.515 eV (Figure 5.10b).

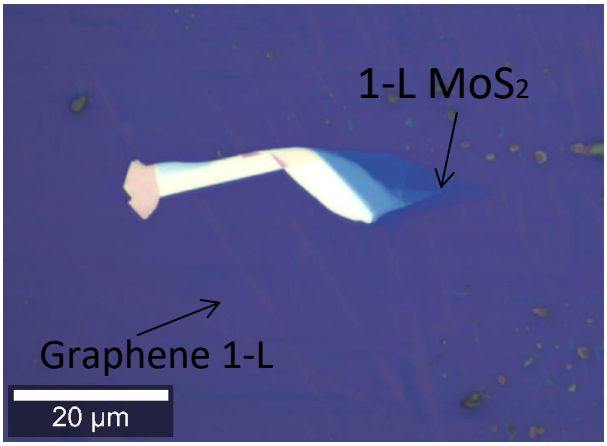

Figure 5.9. Graphene 1-L on exfoliated MoS_2 thin flake, substrate SiO_2/Si. Image from optical microscope.

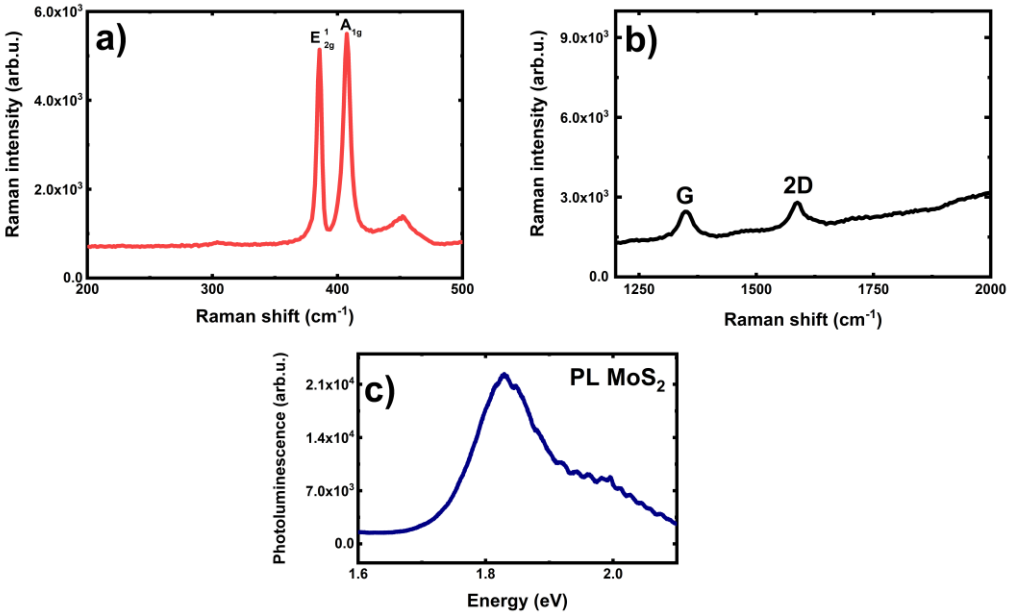

Figure 5.10. a) Raman spectrum for 1-L graphene on MoS_2 monolayer; b) Zoom on Raman peaks for 1-L graphene; c) Photoluminescence for MoS2 monolayer.

5.4.3 The WS_2/h-BN/WS_2 heterostructure

The hexagonal boron nitride (h-BN) is commonly used material for encapsulation of exfoliated flakes. In most cases, this material is used for band structure engineering of 2D crystals with atomic layer precision. In this work, a few heterostructures with h-BN were studied. The first heterostructure is h-BN/WS_2 monolayer (Figures 5.11-5.12) and the second one is WS_2/h-BN/WS_2 (Figures 5.13-5.14), which consist from WS_2 monolayer on bottom, h-BN flake in the middle and WS_2 monolayer on a top.

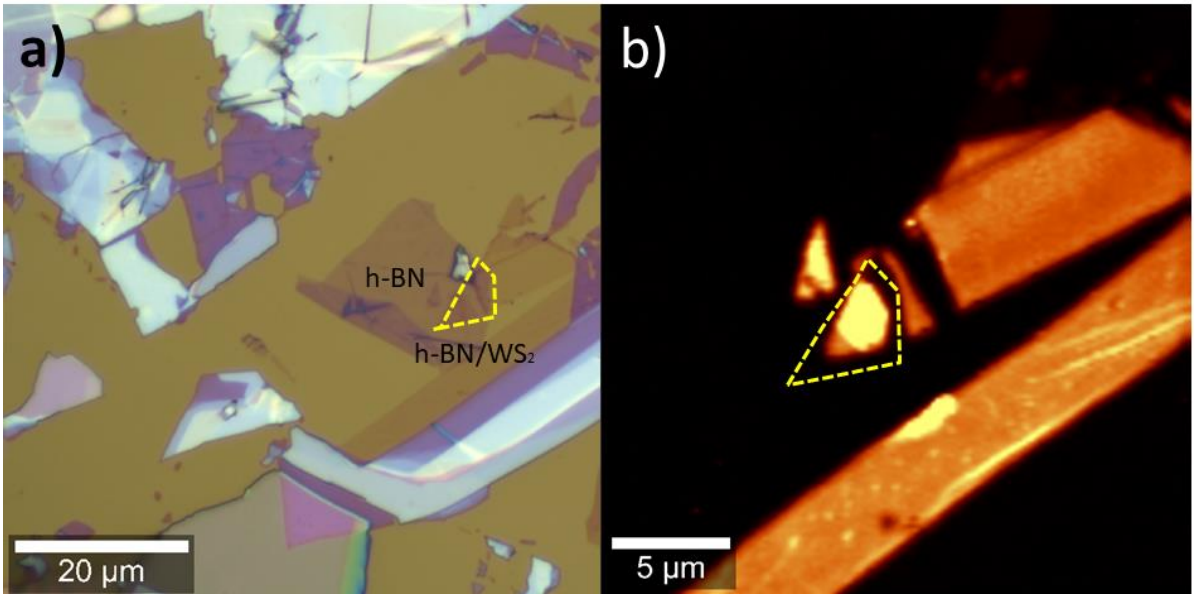

Figure 5.11. a) Image of heterostructure h-BN/WS_2 (yellow area); b) PL map of h-BN/WS_2 heterostructure.

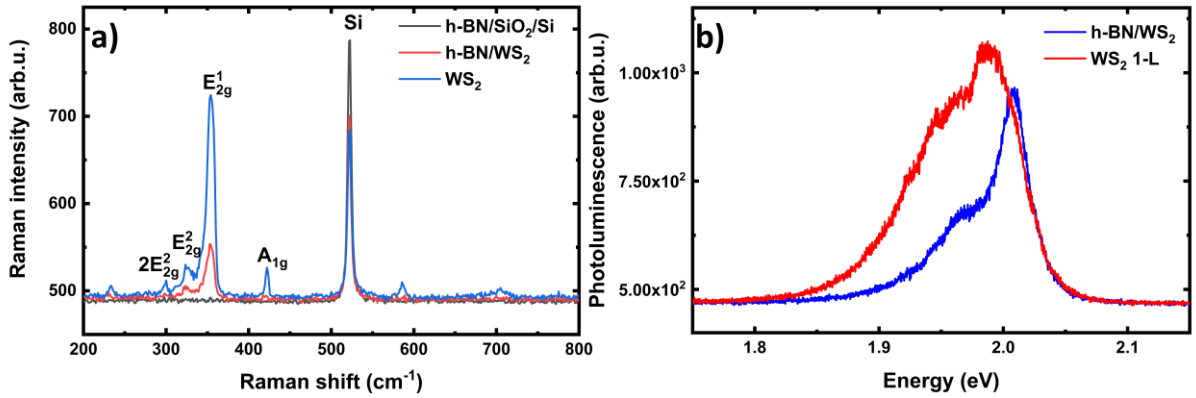

Figure 5.12. a) Raman spectra comparison for heterostructure h-BN/WS_2, h-BN and WS_2 monolayer; b) PL spectroscopy for heterostructure h-BN/WS_2 and WS_2 monolayer.

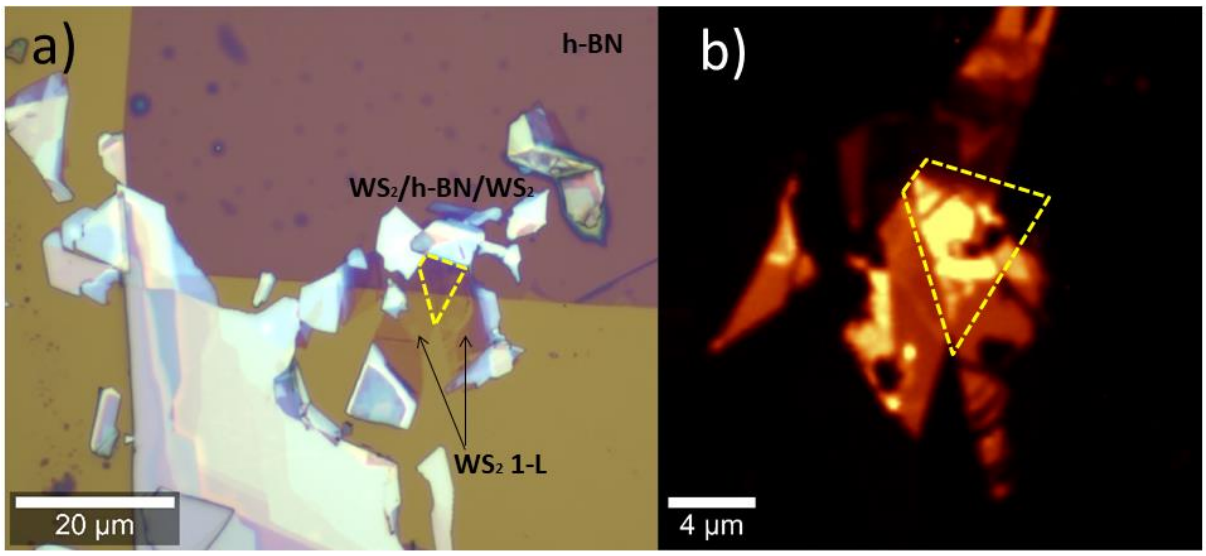

Figure 5.13. a) Image of heterostructure WS_2/h-BN/WS_2 (yellow area); b) PL map of WS_2/h-BN/WS_2 heterostructure.

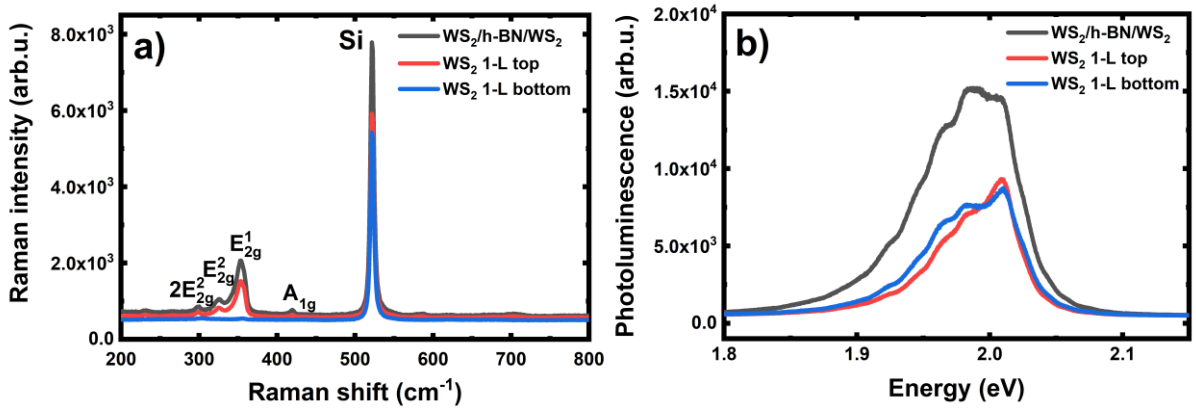

Figure 5.14. a) Raman spectra comparison for heterostructure WS_2/h-BN/WS_2, WS_2 top and bottom; b) PL spectroscopy of heterostructure WS_2/h-BN/WS_2 and WS_2 top and bottom monolayers.

The Raman spectra for both heterostructures are characterized with a few modes for WS_2 monolayer and Si substrate. Modes for h-BN at 1056 cm^{-1} and 1305 cm^{-1} are hardly detected. The main result from heterostructure measurements is that there is a noticeable increase in photoluminescence, see Figure 5.12b and Figure 5.14b. This effect also was showed on Raman maps, see Figure 5.11b and Figure 5.13b. Therefore, when an insulating h-BN layer is inserted between the WS_2 monolayers, an enhanced photoluminescence signal is observed at the stacked region WS_2/h-BN/WS_2.

Katoch *et al.* provide novel insights into the interactions between layers in h-BN based heterostructures where the intercalating an h-BN layer into the TMDCs layers could interfere the electron-hole indirect recombination and enable distinct interlayer interactions, such as Förster energy transfer from one monolayer to the other. This energy transfer gives rise to PL enhancement in the stacked region.[175] The similar effect was noticed in our WS_2/h-BN/WS_2 heterostructure. Such a conclusion indicates a high potential of applying such heterostructures for fabrication the optoelectronic devices.

6 Stability of exfoliated layered materials under ambient conditions

Systematic study of oxidation and degradation mechanism of the mechanically exfoliated flakes in ambient conditions was performed to understand the main differences between each material in terms of sensitivity upon ambient exposure. To study oxidation process, MX_2 flakes were exfoliated onto Si with SiO_2 oxide thickness of 300 nm. Samples were exfoliated in nitrogen Glovebox where O_2 and H_2O < 1 parts per million (ppm). Immediately after exfoliation, Raman and PL spectra were measured. Later, flakes are left exposed to ambient laboratory conditions for variable time intervals from exfoliation till one month. The photodegradation and oxidation processes in these materials was monitored by variation the peak intensities on the Raman and PL spectra. Both Raman and PL spectroscopy gives information about the material content and surface changing during the oxidation process.

6.1 Stability study of exfoliated monochalcogenides (MX)

The oxidation and degradation mechanism was observed in materials from group III (GaS, $GaS_{0.5}Se_{0.5}$) and IV (GeS, GeSe, SnS, SnSe) layered monochalcogenides in ambient conditions. Research on this topic is presented in detail in publication ***P1***.

6.2 Stability study of exfoliated dichalcogenides (MX_2)

The stability of materials from the dichalcogenides MX_2 group has also been researched. Table 2 presents a summary of the stability tests performed on these materials, where the low degree of oxidation (*Low oxidation*) observed for materials such as MoS_2, WS_2, ZrS_2 and ReS_2; high degree of oxidation (*Strong oxidation*) for HfS_2, $HfSe_2$, $ZrSe_2$ and $ReSe_2$.

Table 2. Qualitative of TMDCs materials degradation after one month in ambient conditions.

Material	Photo-oxidation	Low oxidation	Medium oxidation	Strong oxidation
MoS_2		X		
$MoSe_2$	X			
$MoTe_2$	X			
WS_2		X		
WSe_2	X			
WTe_2	X			
HfS_2				X
$HfSe_2$				X
ZrS_2		X		
$ZrSe_2$				X
ReS_2		X		
$ReSe_2$				X

The HfS_2 material could be easily exfoliated down to monolayer, see Figure 6.1. From Raman spectra for HfS_2 flake with thickness *d* = 379 nm, the three prominent Raman modes were detected, which are attributed to the in-plane and out-of-plane vibration of hafnium and disulfide atoms. We observe that the intensities of Raman peaks for freshly exfoliated HfS_2 flakes increase (Figure 6.2a) with increasing number of layers (Figure 6.2b). With increasing oxidation time, intensity of all peaks are drastically decreased and strong oxide layer appears on a surface. Additionally, the Raman peak position is slightly shifted in few-layer flake from 339 to 341 cm^{-1} (Table 3).

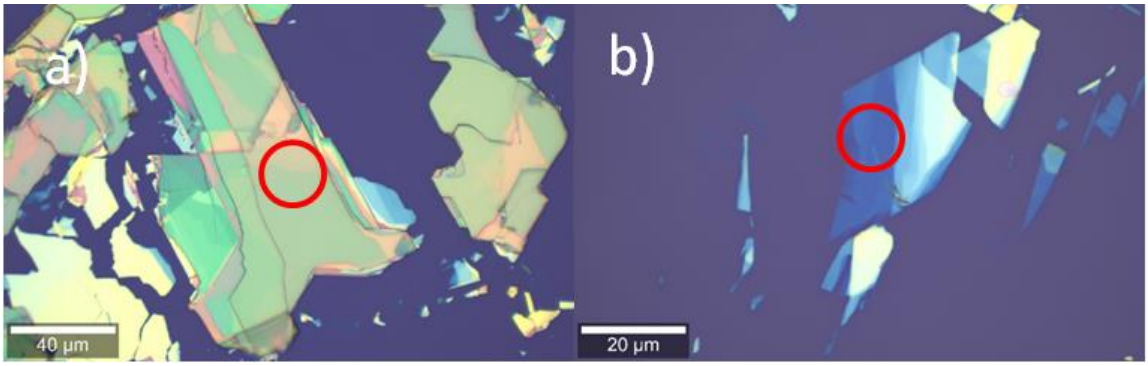

Figure 6.1. Images of freshly exfoliated HfS_2 flakes: a) Thick HfS_2 flake with thickness of 379 nm; b) Thin HfS_2 flake with thickness of 4.5 nm.

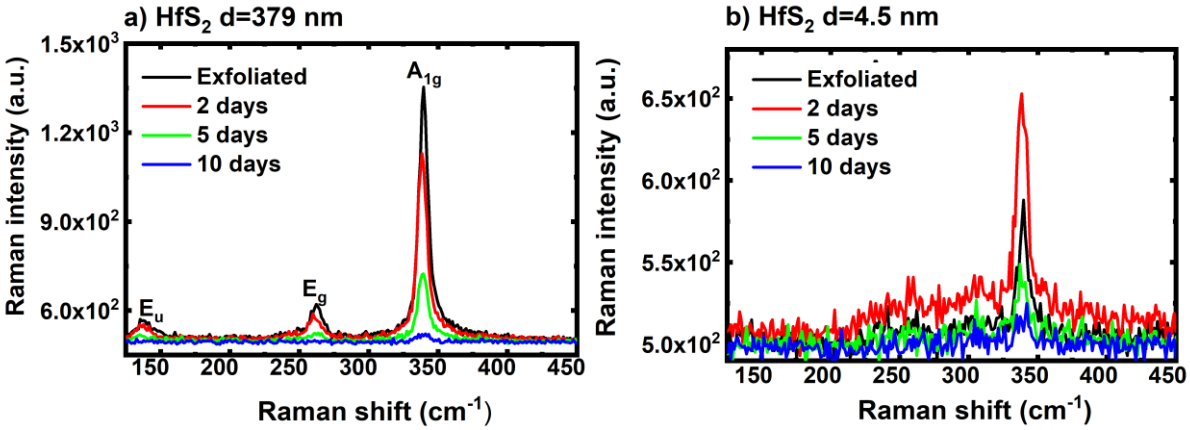

Figure 6.2. Raman spectra for oxidised: a) Thick HfS_2 flake with thickness of 379 nm; b) Thin HfS_2 flake with thickness of 4.5 nm.

Table 3. Summary of prominent Raman modes for HfS_2 flakes.

HfS_2	Raman peak position, cm^{-1}		
	E_u	E_g	A_{1g}
Thick flake (exfoliated), d=379 nm	136	262	338
Thick flake (10 days), d=379 nm	137	263	340
Few-layer flake (exfoliated), d=4.5 nm	Not observed	Not observed	339
Few-layer flake d=4.5 nm (10 days)	Not observed	Not observed	341

Figures 6.3 and 6.4 show the results of photoluminescence measurements for HfS_2 oxidised flakes. After comparing the PL spectra (Figure 6.3), the signal for thick flake is much more intense than for few-layer flake (Figure 6.3a). The oxidation effect in HfS_2 material is thickness dependent as seen from PL spectra. For few-layer and thin flake, the PL decreases with increasing oxidation time. In case thick flake, this tendency is not observed. These results suggests that in thick flake there is oxidised only the top layer of the flake but bottom ones are untouched.

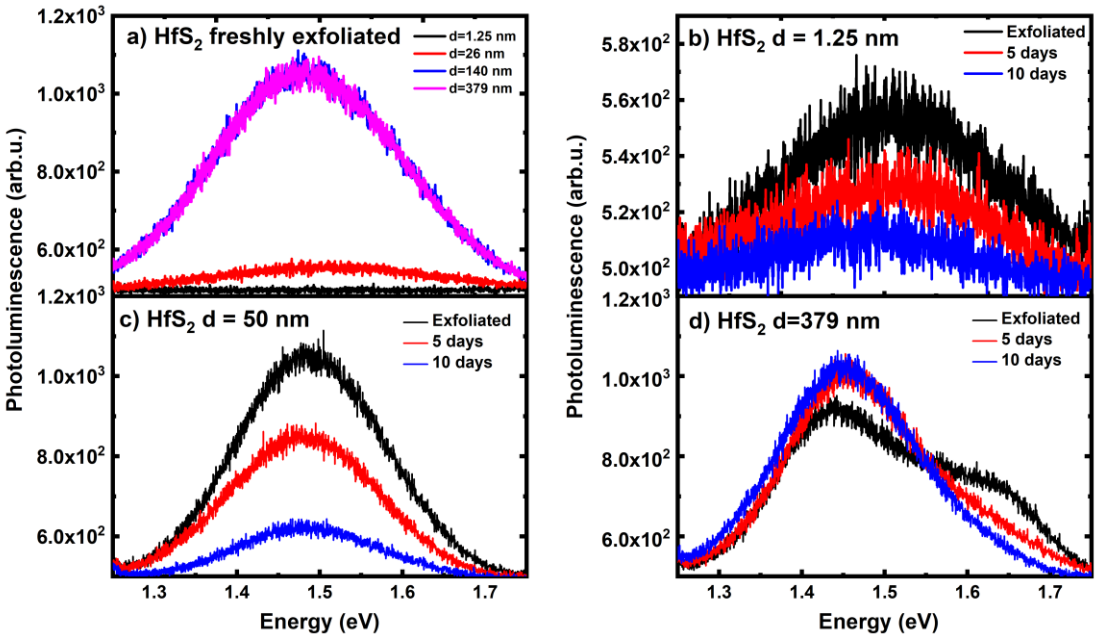

Figure 6.3. Photoluminescence spectra for HfS_2: a) Freshly exfoliated HfS_2 flakes with different thickness; b) HfS_2 few-layer flake with thickness of 1.25 nm; c) HfS_2 flake with thickness of d = 50 nm; d) HfS_2 flake with thickness of d = 379 nm.

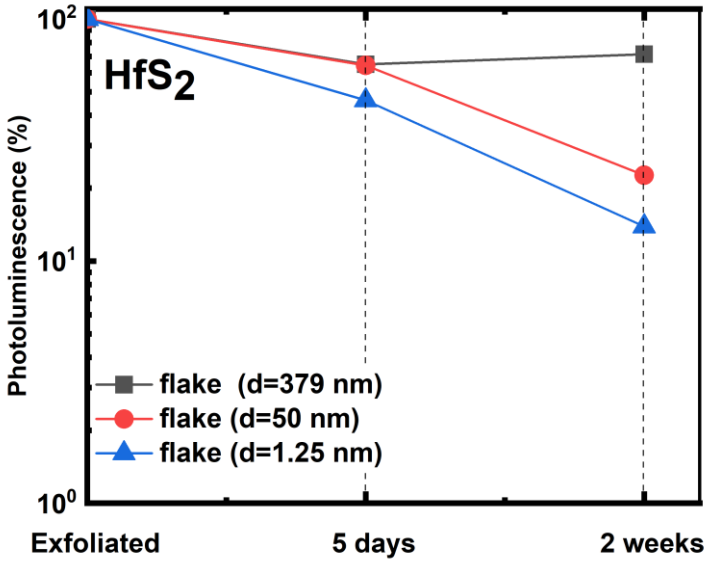

Figure 6.4. Summary of photoluminescence stability for HfS_2 few-layer, thin and thick flake with increasing oxidation time in ambient conditions.

The next studied material is $HfSe_2$, the images of freshly exfoliated and degraded flakes after four weeks in ambient conditions are shown on optical images (Figures 6.5-6.6).

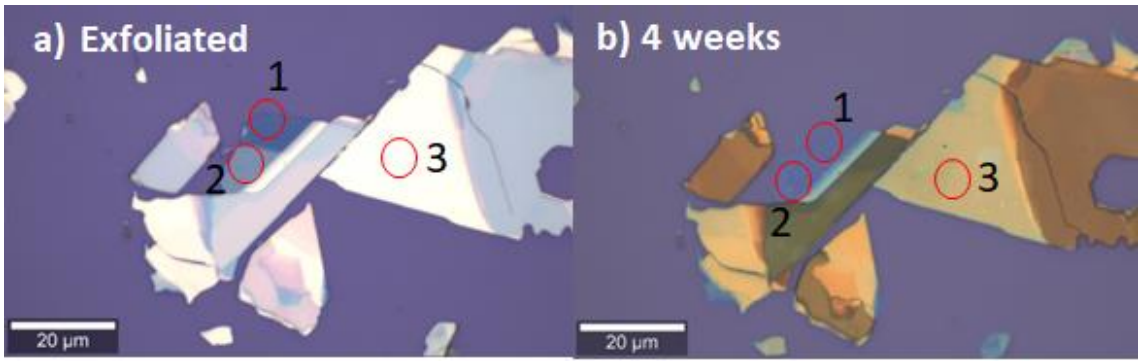

Figure 6.5. a) Image of $HfSe_2$ freshly exfoliated flakes; b) Image of oxidised $HfSe_2$ flakes after month in ambient conditions.

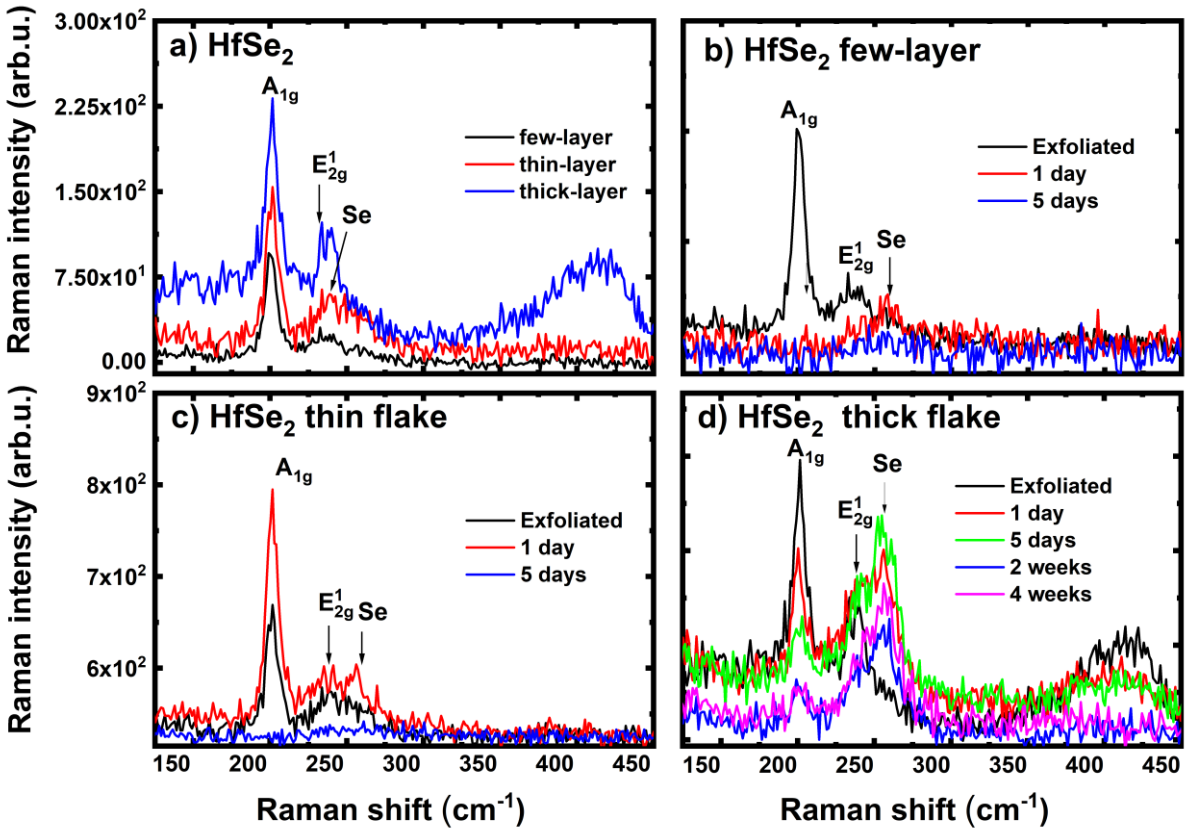

Figure 6.6. Raman spectra for exfoliated $HfSe_2$: a) Spectra comparison for freshly exfoliated $HfSe_2$ flakes with different thickness; b) Oxidised $HfSe_2$ few-layer; c) Oxidised $HfSe_2$ thin flake; d) Oxidised $HfSe_2$ thick flake.

After carefully analysing the $HfSe_2$ material, we see that the mode intensities for few-layer are more weaker than for thick flake (Figure 6.6a). The broad peak from thick flake is located at 430 cm^{-1}, whereas for few-layer is not founded (Table 4). Few-layer $HfSe_2$ is degraded very quickly and already after 24 h in ambient the flake is fully converted into oxide and no Raman peaks were detected (Figure 6.6b). The fully oxidation, in case thin flake, is about 5 days (Figure 6.6c). Whereas thick flake after 1 month in ambient, is partially converted into oxide and the broad peak from Se (260 cm^{-1}) was detected (Figure 6.6c).

Table 4. The prominent Raman modes for $HfSe_2$ flakes.

$HfSe_2$	Raman peak position, cm^{-1}		
	A_{1g}	E^1_{2g}	
Thick flake (exfoliated)	201	236	413
Thick flake (month)	199	Not observed	Not observed
Thin layer (exfoliated)	201	242	Not observed
Thin layer (5 days)	Not observed	Not observed	Not observed
Few-layer (exfoliated)	199	241	Not observed
Few layer (5 days)	Not observed	Not observed	Not observed

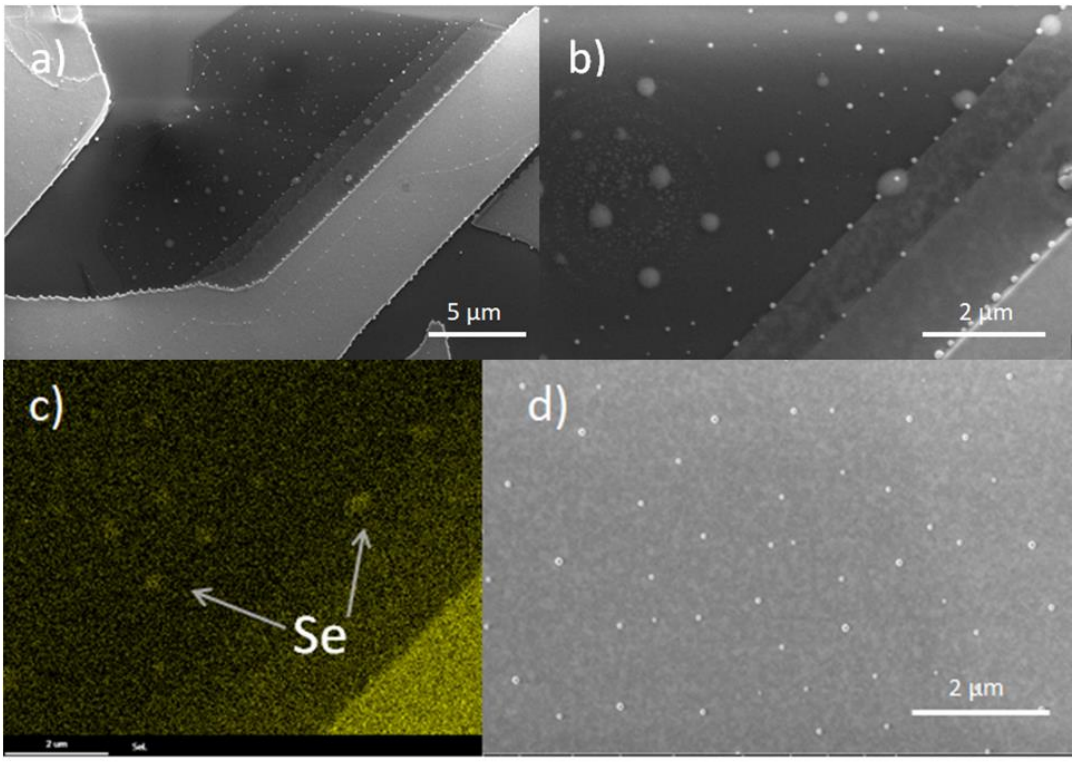

Figure 6.7. a) SEM image of $HfSe_2$ few-layer after 3 weeks oxidation in ambient conditions; b) SEM image of protrusions on top of few-layer; c) EDS map of Se element gathered from oxidised few-layer flake; d) SEM image of protrusions on oxidised thick flake.

The next materials which were studied are ZrS_2 and $ZrSe_2$. For ZrS_2 material, oxidation study was performed by using Raman and PL spectra. The few ZrS_2 Raman modes were detected (E_g and A_{1g}), which intensities are decreased significantly with increasing the oxidation time (Table 5). Such effect observed for monolayer and thick flake (Figure 6.8). Additionally, the PL spectra were measured for this material to better understand the

oxidation process (Figure 6.8). For freshly exfoliated ZrS_2 flakes the PL is much more giant. Therefore, in case thick flake, PL is more weaker (Figure 6.8a). After the two weeks in ambient, the maximum of photoluminescence for ZrS_2 1-Layer was shifted from 1.85 eV (for freshly exfoliated flake) to 1.87 eV (after 2 weeks of oxidation). For all oxidised ZrS_2 flakes the ZrO_2 peak was strongly visible, particularly in oxidised 1-Layer with maximum at 2.06 eV (Figures 6.8b-d).

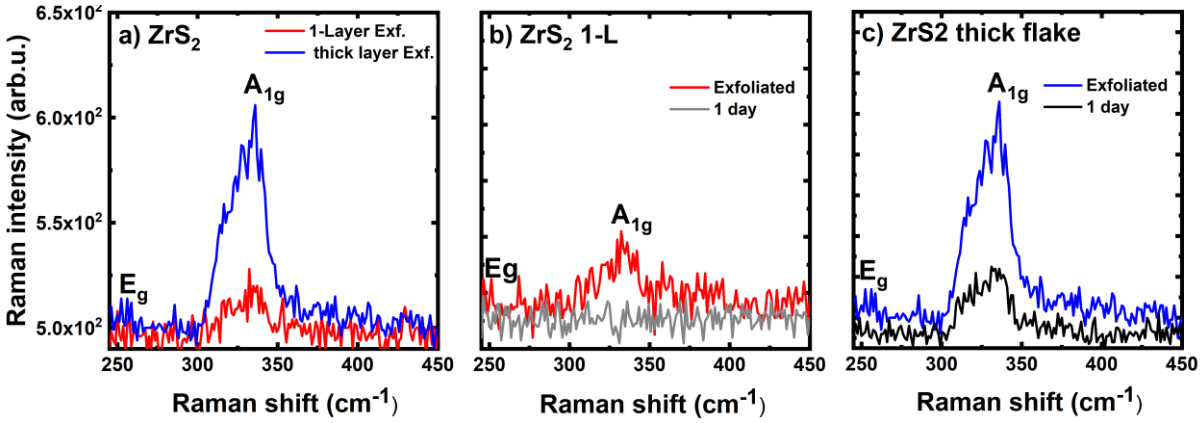

Figure 6.8. Raman spectra for ZrS_2: a) Comparison of Raman peak intensity for freshly exfoliated 1-layer and thick layer; b) Comparison of Raman peak intensity for freshly exfoliated and oxidised 1-Layer; c) Comparison of Raman peak intensity for freshly exfoliated and oxidised thick flake.

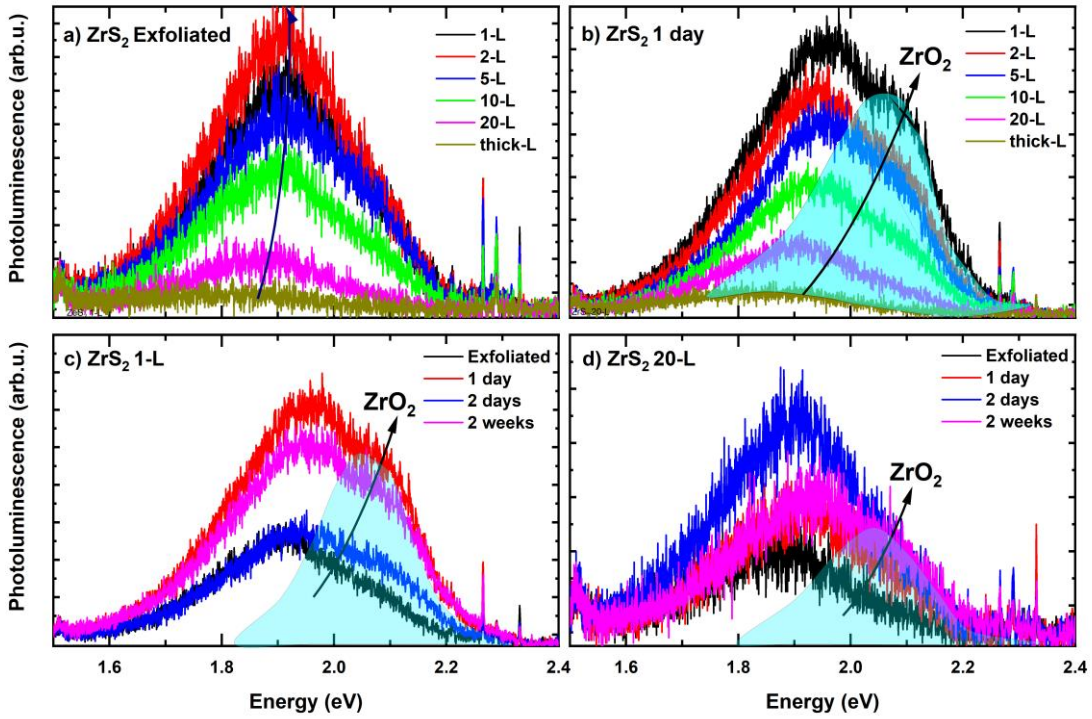

Figure 6.9. Photoluminescence for ZrS_2 flakes: a) Photoluminescence spectra for freshly exfoliated flakes with different thickness; b) PL for flakes after 1 day in ambient; c) PL spectra for oxidised 1-Layer; d) PL spectra oxidised thick flake.

Table 5. The prominent Raman modes for ZrS_2 flakes.

ZrS_2	Raman peak position, cm^{-1}	
	E_g	A_{1g}
Thick flake (exfoliated)	256	335
Thick flake (1 day)	Not observed	331
Thick flake (2 weeks)	Not observed	Not observed
1-Layer (exfoliated)	251	332
1-Layer (1 day)	Not observed	Not observed

In case $ZrSe_2$, the degradation of exfoliated flakes was visible already after 2 days in ambient conditions (Figure 6.10). The measured Raman spectra clearly show the 1-L degradation after day in ambient, thin flake after 2 weeks and a noticeable decrease in the intensity of the A_{1g} peak for the thicker flake (Figure 6.11 and Table 6).

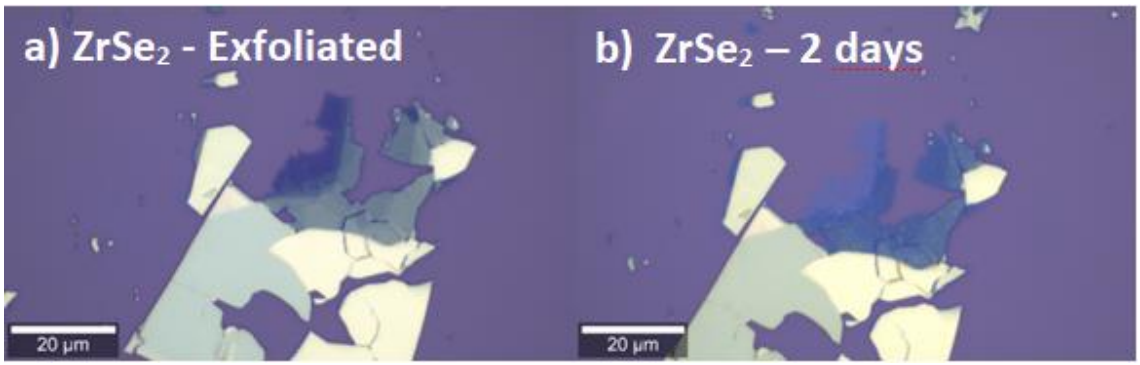

Figure 6.10. Optical image of $ZrSe_2$ freshly exfoliated flakes and 2 days of sample air exposure.

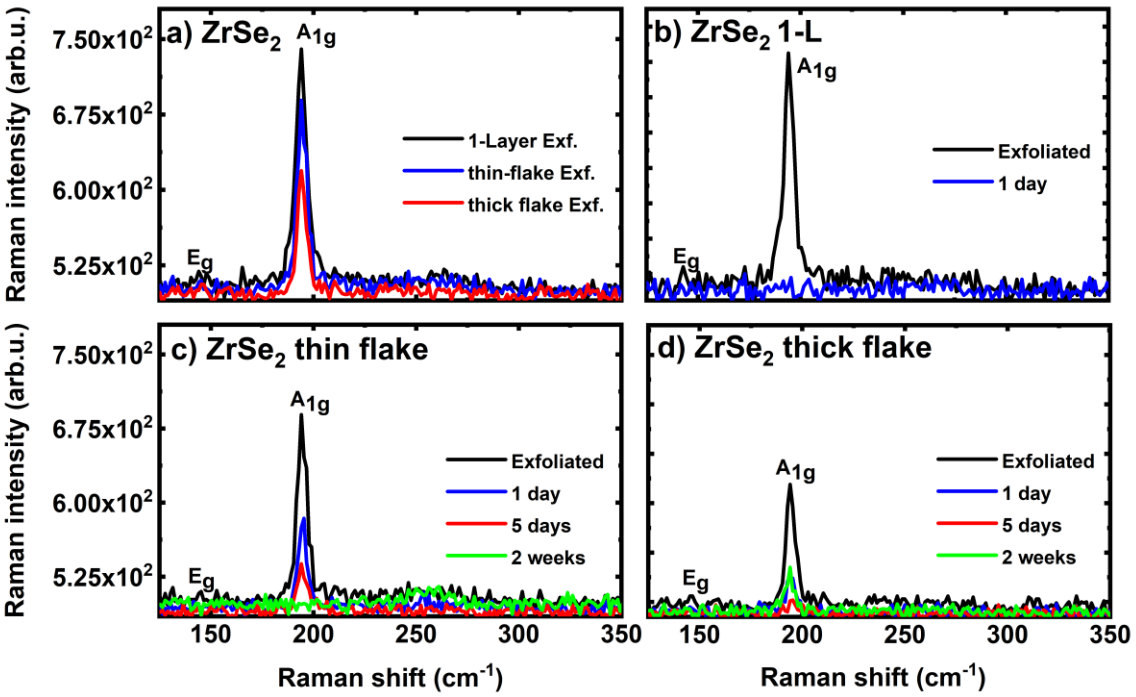

Figure 6.11. Raman spectra for exfoliated $ZrSe_2$ flakes: a) Raman spectra for freshly exfoliated $ZrSe_2$ flakes; b) Oxidised 1-Layer flake; c) Oxidised 10-layer flake; d) Oxidised thick layer flake.

Table 6. The prominent Raman modes for $ZrSe_2$ flakes.

$ZrSe_2$	Raman peak position, cm^{-1}	
	E_g	A_{1g}
Thick flake (freshly exfoliated)	144	194
Thick flake (1 day)	Not observed	194
Thick flake (2 weeks)	Not observed	194
1-Layer (exfoliated)	Not observed	194
1-Layer (1 day)	Not observed	Not observed

The decomposition of ZrS_2 and $ZrSe_2$ is associated with oxidation into amorphous ZrO_x, high-K dielectric of immediate technological relevance and S, Se accumulation in surface protrusions (Figure 6.12).

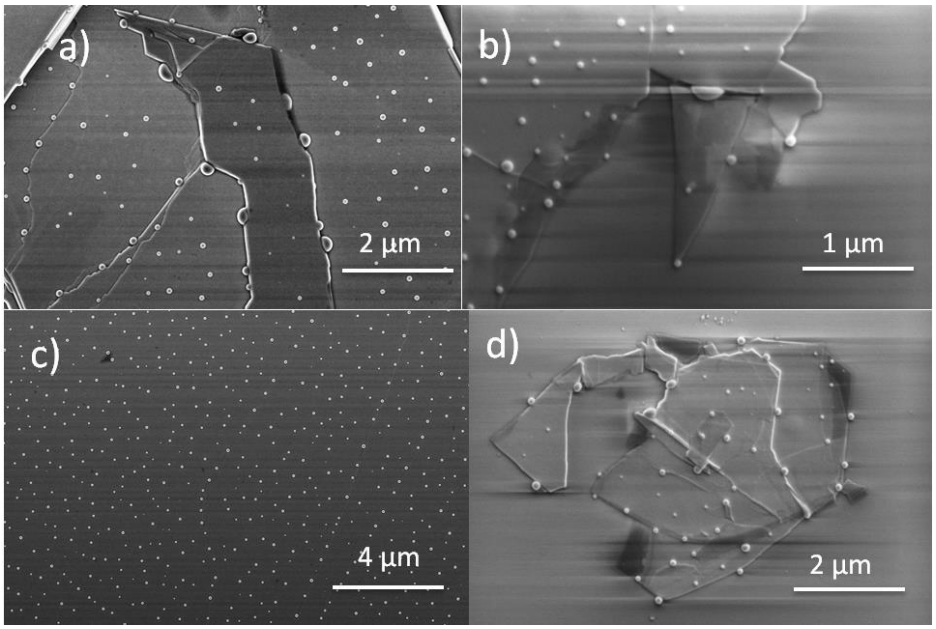

Figure 6.12. $ZrSe_2$ flake surface after 2 weeks oxidation in ambient conditions.

From the Raman spectra for exfoliated $ZrSe_2$ flakes, the intensity of A_{1g} peak, which located at 194 cm^{-1}, during the oxidation process changes. After two weeks of the sample in ambient conditions, the A_{1g} Raman peak is no longer visible (Figure 6.11). According to $ZrSe_2$ photoluminescence spectra, the maximum of which is located at 1.89 eV, the strongest signal was observed for $ZrSe_2$ 1-L and the weakest for thick $ZrSe_2$ flake (Figure 6.13a). As well as in ZrS_2 oxidised flakes, a broad peak from ZrO_2 was noticed at position of 2.02 eV (Figures 6.13b-c).

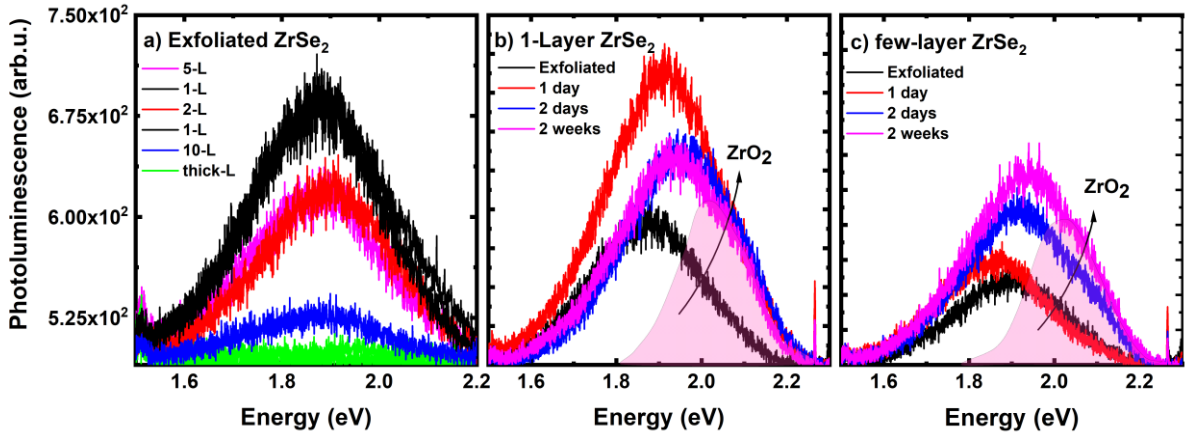

Figure 6.13. Photoluminescence for $ZrSe_2$ flakes: a) Photoluminescence for exfoliated $ZrSe_2$ flake with different thickness; b) PL for oxidised 1-Layer; c) PL spectra for oxidised few-layer.

In summary, from PL stability studies of exfoliated $ZrSe_2$ flakes, we confirmed that the $ZrSe_2$ monolayer is more prone to quick oxidation compared to thicker flake. To conclude,

monolayer oxidation occurs already after 2 days instead as few-layer was oxidised already after 5 days in ambient laboratory conditions.

The ReS_2 and $ReSe_2$ are bulk semiconductors with indirect band gap.[106] After two weeks of ReS_2 oxidation, no any bubbles or protrusions were noticed (Figure 6.14b).

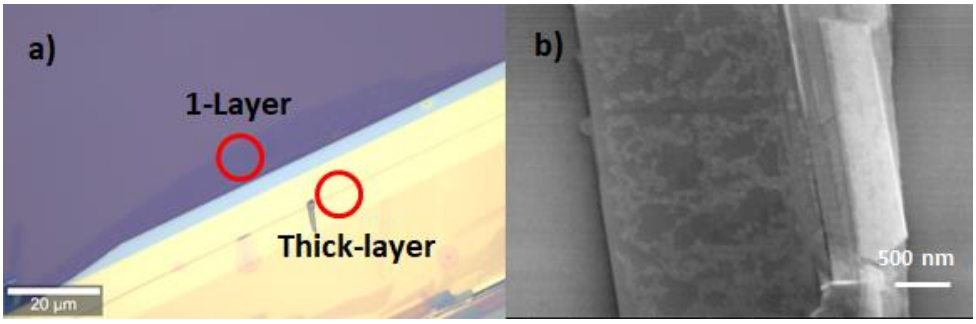

Figure 6.14. Images of freshly exfoliated ReS_2 flakes: a) Images of 1-Layer and thick flake ReS_2 flake; b) SEM image of oxidised ReS_2 thick flake surface, oxidation time - 2 weeks.

The Raman spectra of the Re based dichalcogenides are feature-rich with of 18 first-order Raman active modes in the range of 100−300 cm^{-1}, which are nondegenerate because of their low symmetry structure. For thick ReS_2 flake the two intense and characteristic vibration modes were observed at 154 and 214 cm^{-1} (Table 7). The Raman intensities were decreased with increasing oxidation time both for thin and thick exfoliated flakes, see Figure 6.15.

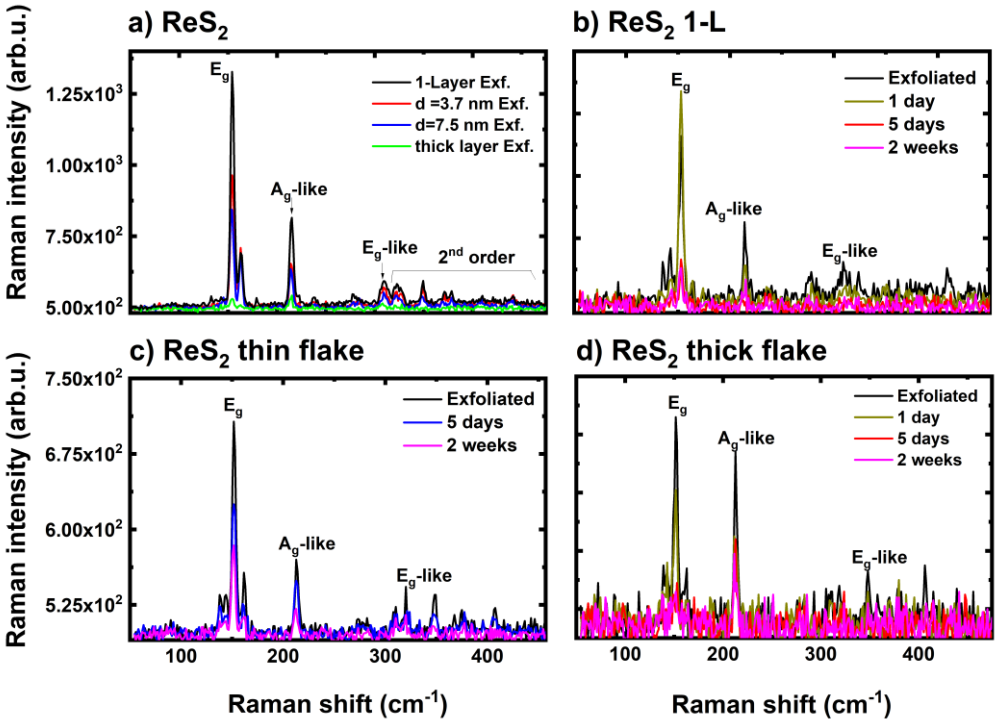

Figure 6.15. Raman spectra comparison for: a) Freshly exfoliated ReS_2 flakes with different thickness; b) Oxidised ReS_2 1-Layer; c) Oxidised thick ReS_2 flake; d) Oxidised ReS_2 4-Layer.

Table 7. Raman peak positions for ReS_2 exfoliated flakes.

ReS_2	Raman peak position, cm^{-1}		
	E_g	A_{1g}	$A_{1g-like}$
Thick flake (exfoliated)	151	212	348
Thick flake (1 day)	151	212	348
Thick flake (2 weeks)	152	211	Not observed
1-Layer (exfoliated)	152	214	309
1-Layer (1 day)	152	214	Not observed
1-Layer (2 weeks)	152	215	Not observed

It is suggested that the energy of the dominant radiative transition increases as the material thickness is reduced. From bulk to monolayer, ReS_2 remains a direct-bandgap semiconductor, its PL intensity increases, whereas the Raman spectrum remains unchanged with increasing number of layers. All the ReS_2 flakes exhibit PL at room temperature with a peak in the range of 1.5 – 1.6 eV (Figure 6.16). The dependence of PL properties with sample thickness provides a simple way to verify the weak interlayer coupling in the 1T-stucture and check for a crossover from direct to indirect band gap. The PL peak intensity for exfoliated ReS_2 is higher for the thicker flake, see Figure 6.16a. This is in a sharp contrast to the typical behaviour seen in Mo- and W-based TMDCs and confirms that ReS_2 behaves as a stack of decoupled monolayers even in bulk form.

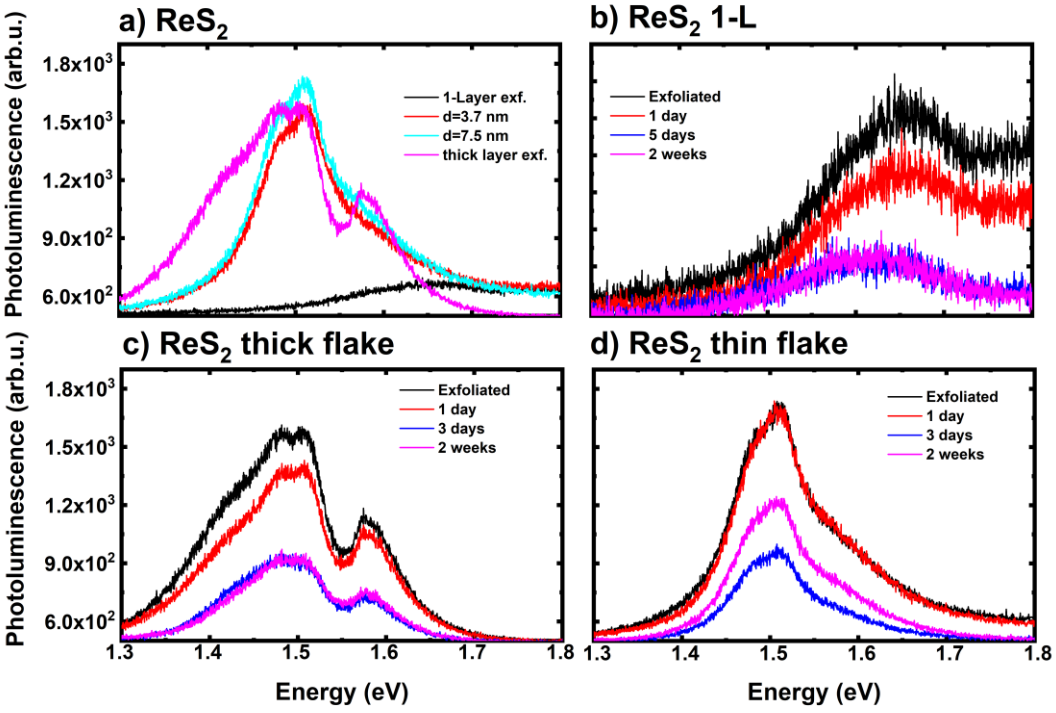

Figure 6.16. Photoluminescence spectra for ReS_2 flakes with different thickness.

The $ReSe_2$ belongs to the same structure formation as ReS_2 and shows nearly the same number of active vibrational modes on its Raman spectrum. Degradation of ReS_2 and ReS_2 materials is accompanied by partial elimination of sulphur from the near surface region and/or formation of an oxidized Rhenium overlayer. The enhanced reactivity of these sites appears to be closely related to their ability to strongly chemisorb oxygen which is not detectable on stoichiometric basal plane surfaces.

Examples of exfoliated $ReSe_2$ flakes are presented on Figure 6.17. Raman spectra for $ReSe_2$ consist of about 12 peaks (Figure 6.18). We observed differences in intensity and position of the main Raman peaks E_g-*like* and A_g-*like* for 1,2,4-Layer and thick flake. Additionally, PL spectra were measured for 1-L, 2-L and thick flake (Figure 6.19). The peak position shifts slightly from 1.31 eV for the thin layer to 1.29 eV for the thick flake (Table 8).

In case photoluminescence, the lower PL signal intensity was obtained for thick flake and the highest for $ReSe_2$ 1-layer. The PL spectrum for 1-Layer $ReSe_2$ is right-shifted from 1.29 eV (bulk) to 1.31 eV (Figure 6.19a). From the oxidation study of $ReSe_2$ flakes, no significant changes in the Raman and PL spectra were noticed, which indicates the high stability of this material in ambient conditions.

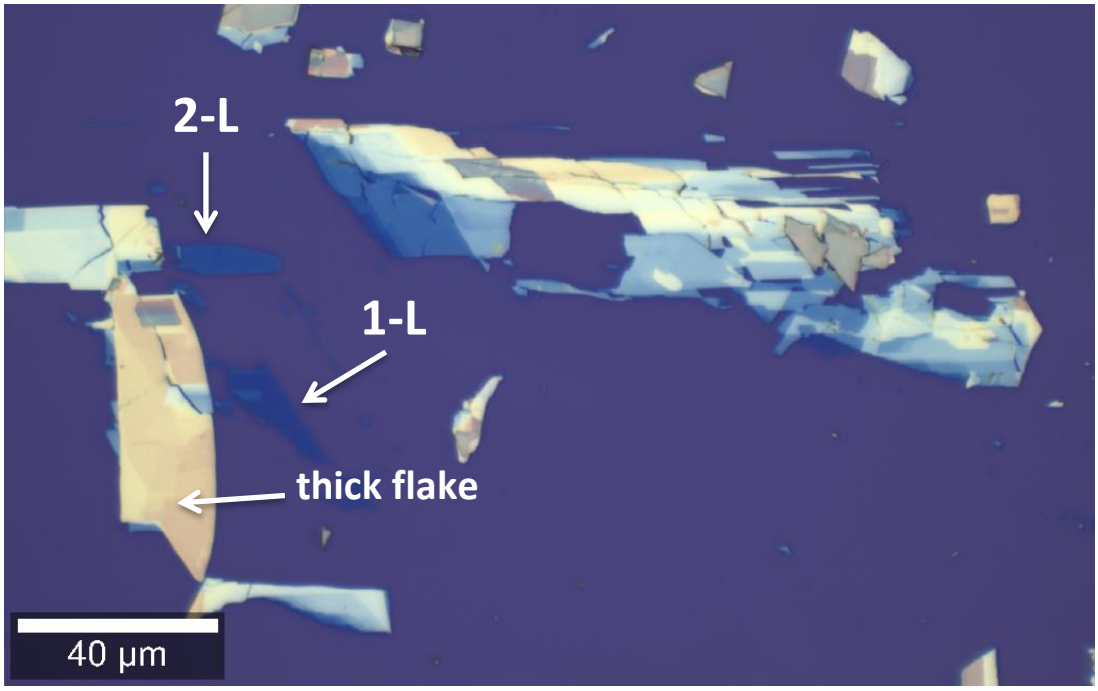

Figure 6.17. Exfoliated $ReSe_2$ flakes with different thickness from 1-L to thick flake.

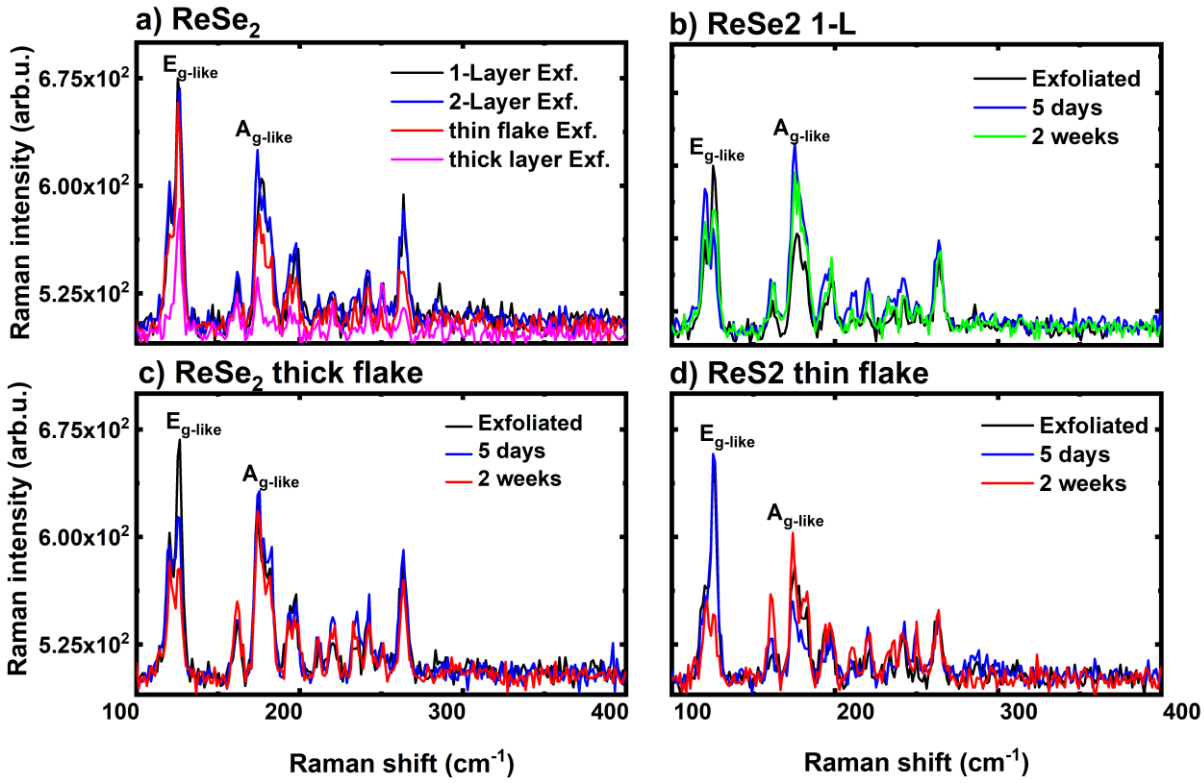

Figure 6.18. Raman spectrum for $ReSe_2$: a) Freshly exfoliated flakes; b) Oxidised 1-Layer; c) Oxidised 2-layer; d) Oxidised 3-Layer.

Table 8. Raman peak positions for $ReSe_2$ exfoliated flakes.

	Raman peak position, cm^{-1}	
$ReSe_2$	$E_g - like$	$A_{1g} - like$
Thick flake (exfoliated)	126	174
Thick flake (5 days)	126	174
Thick flake (2 weeks)	126	174
1-Layer (exfoliated)	125	175
1-Layer (5 days)	125	177
1-Layer (2 weeks)	127	177

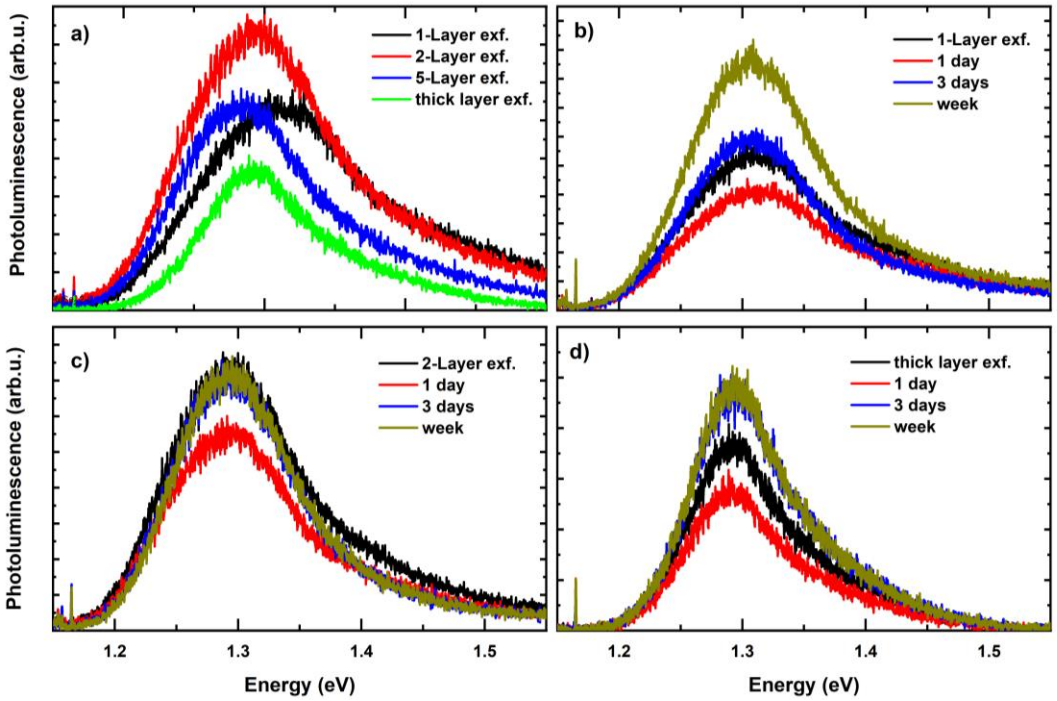

Figure 6.19. Photoluminescence spectra for $ReSe_2$: a) Freshly exfoliated $ReSe_2$ flakes; b) Oxidised $ReSe_2$ 1-Layer; c) Oxidised $ReSe_2$ 2-layer; d) Oxidised $ReSe_2$ 3-Layer.

As summary, the study of oxidation effects in exfoliated thick/thin/few-layer flakes was gathered and presented on Figure 6.20. The highest stability for exfoliated flakes was founded for ReS_2 and $ReSe_2$. Against, the lowest was detected for ZrS_2 and $HfSe_2$ layered materials.

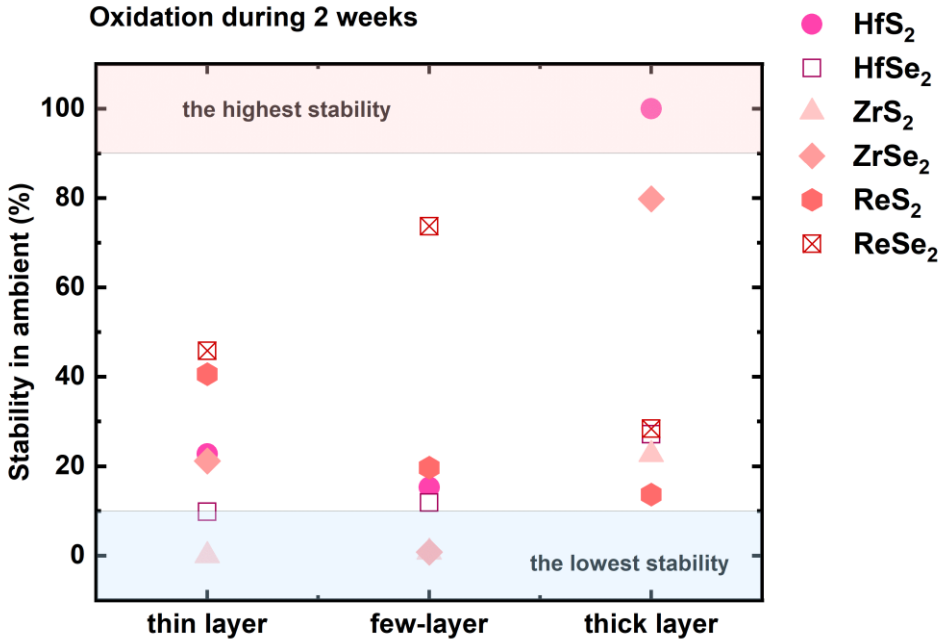

Figure 6.20. Thickness-dependent oxidation in ambient conditions during the two weeks in ambient laboratory conditions. Calculation are based on Raman peaks intensity (A_{1g}, E_g, A_g, E_{2g}, B_{3g}).

6.3 Heating effect on the photoluminescence of WS_2 monolayer

Extending the topic of stability of exfoliated layered materials, the effect of heating the WS_2 monolayer in ambient conditions was performed. To investigate the effect of heating on photoluminescence properties of the WS_2 monolayer, several experiments were carried out in laboratory conditions. First, by using a fluorescent microscope, a series of images were obtained for annealed WS_2 monolayer at temperatures from 298 K to 468 K. The annealing time at each temperature in ambient conditions was 5 minutes (Figure 6.21). After the experiment, the photoluminescence decay was observed for WS_2 monolayer with increasing temperature, where at 468 K the photoluminescence is almost unnoticeable (Figure 6.22).

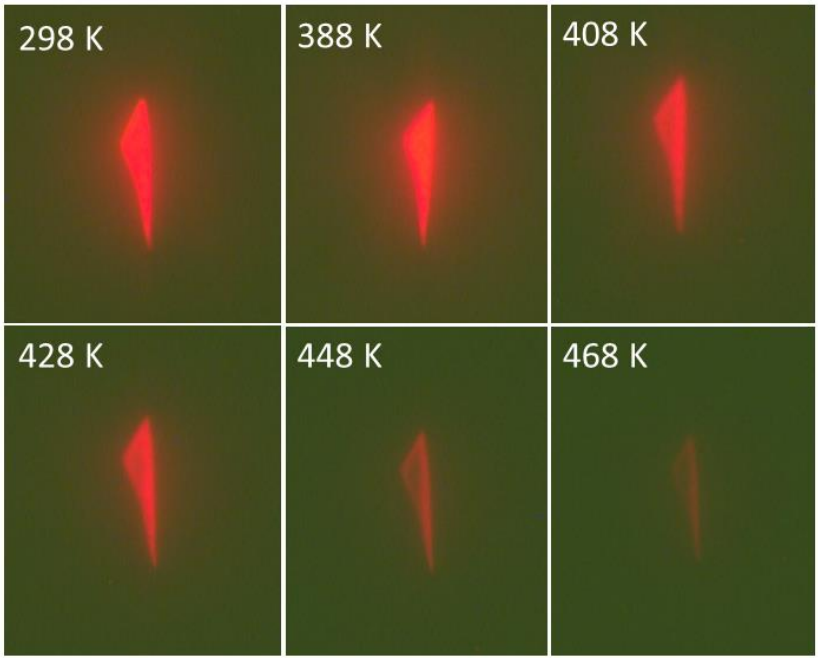

Figure 6.21. Temperature dependent photoluminescence images of WS_2 monolayer.

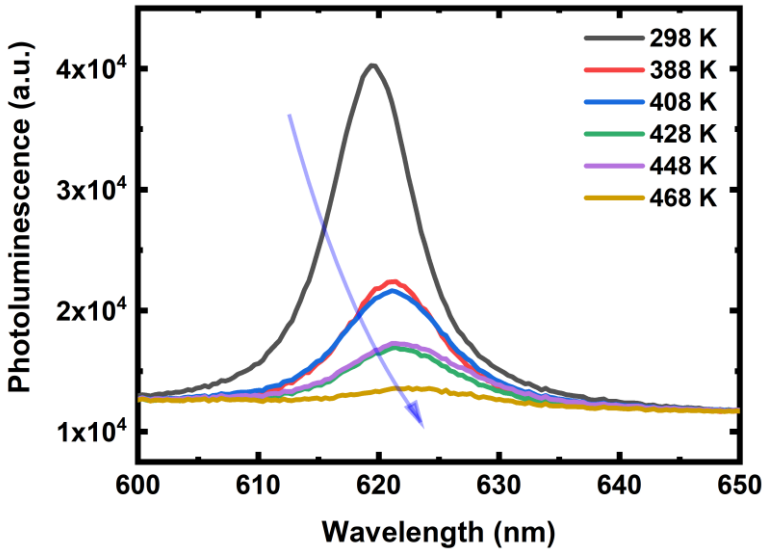

Figure 6.22. Temperature dependent photoluminescence spectra for WS_2 monolayer.

Oxidation of WS_2 material mostly observed after heating in air, whereas this material is quite stable at room temperature. Additionally, the thermal treatment in ambient conditions may cause the adsorption of O_2/H_2O from the air or defect creation due to the applied thermal energy at WS_2, which may result in either PL enhancement or quenching. Additionally, the monolayer instability can also result from the point-defects of the monolayer. Therefore, to protect the exfoliated thin flakes and monolayers, the best solution is to apply a polymer protective layer or deposit the thin layer of Al_2O_3 by atomic layer deposition, which is a frequently used technique to produce stable devices.

6.4 Sol-gel encapsulation of $HfSe_2$ and ReS_2 flakes

Typical thin dielectrics are mostly based on oxides (e.g. SiO_2, Al_2O_3, HfO_2), which intrinsically bring oxygen atoms in contact with TMDCs and can contribute to TMD deterioration. This becomes especially prevalent if elevated temperatures are encountered during the dielectric layer deposition or device operation. Thus, an exploration of a non-oxide based and environmentally stable dielectric material to be used in conjunction with TMD field-effect transistor devices, or other 2D materials such as graphene and black phosphorus, and would benefit the wider usage of such materials.

Encapsulation by spin-on polymer films has provided the fastest pathway to oxygen and moisture barriers, including use of polymethyl methacrylate (PMMA), h-BN, or graphene. Such films suffer from the finite oxygen permeability and relatively poor temperature stability, decomposing or reflowing under the further processing. More robust encapsulation strategies are therefore required, particularly considering the integration of 2D semiconductors in a front-end-of-line microfabrication process.

In this thesis, the encapsulation was performed on extremely unstable material-$HfSe_2$, which commonly used for transistor fabrication. Hf-based TMDCs are predicted to be small band gap semiconductors with large work functions and high mobility, which render them suitable materials for FET applications. In work, sol-gel SiO_x:TiO_y layer used as passivation layer instead of PMMA. Sol-gel film was found to be a good surface passivation layer to prevent the inner part from further oxidation in ambient, which is also promising as a high-K dielectric in $HfSe_2$-based devices.

Raman study degradation and encapsulation results of exfoliated $HfSe_2$ are presented on Figure 6.23. Figs 6.23a-c represent the oxidation study of 1-Layer, 5-Layer, thick flake, respectively. Both Raman spectra shows the quick degradation under ambient laboratory conditions, whereas 1-Layer degrades already after a few days. Encapsulation was tested on a thick $HfSe_2$ flake, where after exfoliation in Glovebox, sol-gel was deposited with spin-coater. For this experiment a thick $HfSe_2$ flake was taken due to larger adhesion to substrate, which is crucial during the spin-coating. The results of the conducted research is shown in Figure 6.23d.

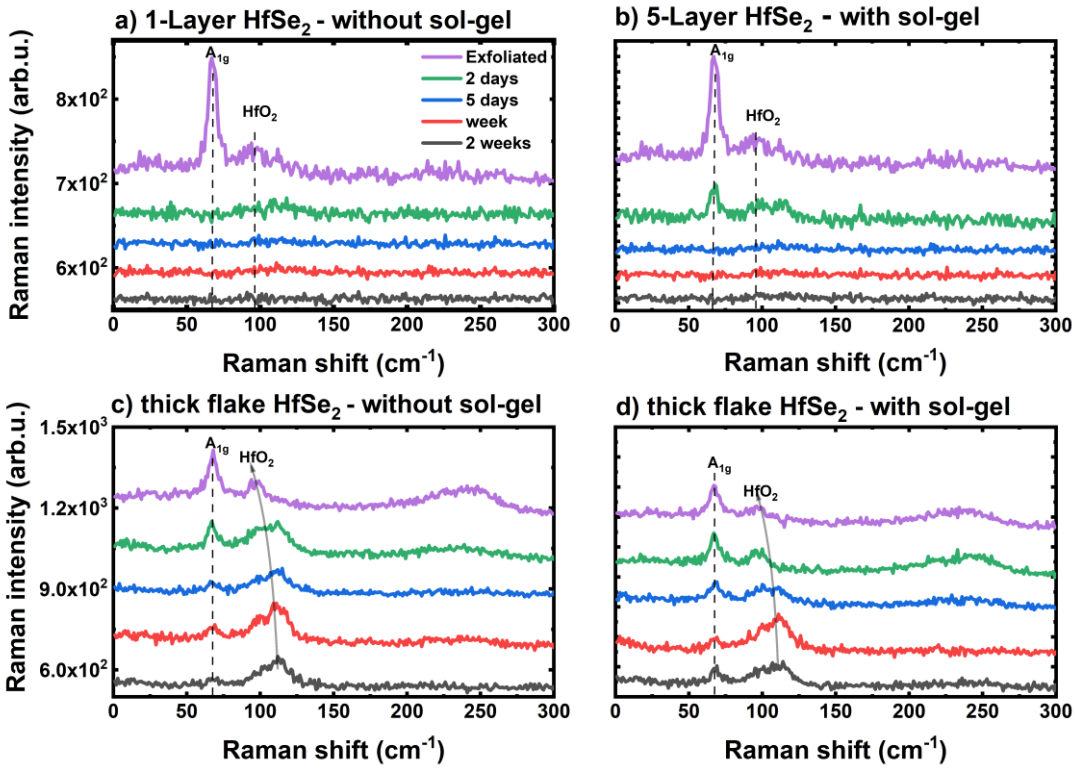

Figure 6.23. Example of $HfSe_2$ encapsulation by sol-gel. Raman study of degradation under ambient: a) 1-Layer; b) 5-Layer; c) Thick flake; d) Raman study of encapsulation thick flake $HfSe_2$ by sol-gel SiO_x:TiO_y.

Raman spectra for uncovered flakes are represented by strong A_{1g} peak and broad peak from HfO_2. The intensity of A_{1g} peak is decreased with oxidation time at ambient, see Figure 6.23a,c. After the 2 weeks of oxidation these peak were hard to detect. In the case of covered $HfSe_2$ thick flake by sol-gel, the A_{1g} peak was visible even after the 2 weeks at ambient, see Figure 6.23d. However, for encapsulated $HfSe_2$ monolayer the A_{1g} peak was disappeared after just 5 days. Additionally, the peak from HfO_2 is noticeable both for the covered and uncovered flakes. This result indicates that covering the flakes with sol-gel helps to stop further flake degradation, mainly this results was observed for thick flakes. The sol-gel encapsulation was applied also to ReS_2 exfoliated flakes. Additionally, photoluminescence study was performed for this material, see Figure 6.24.

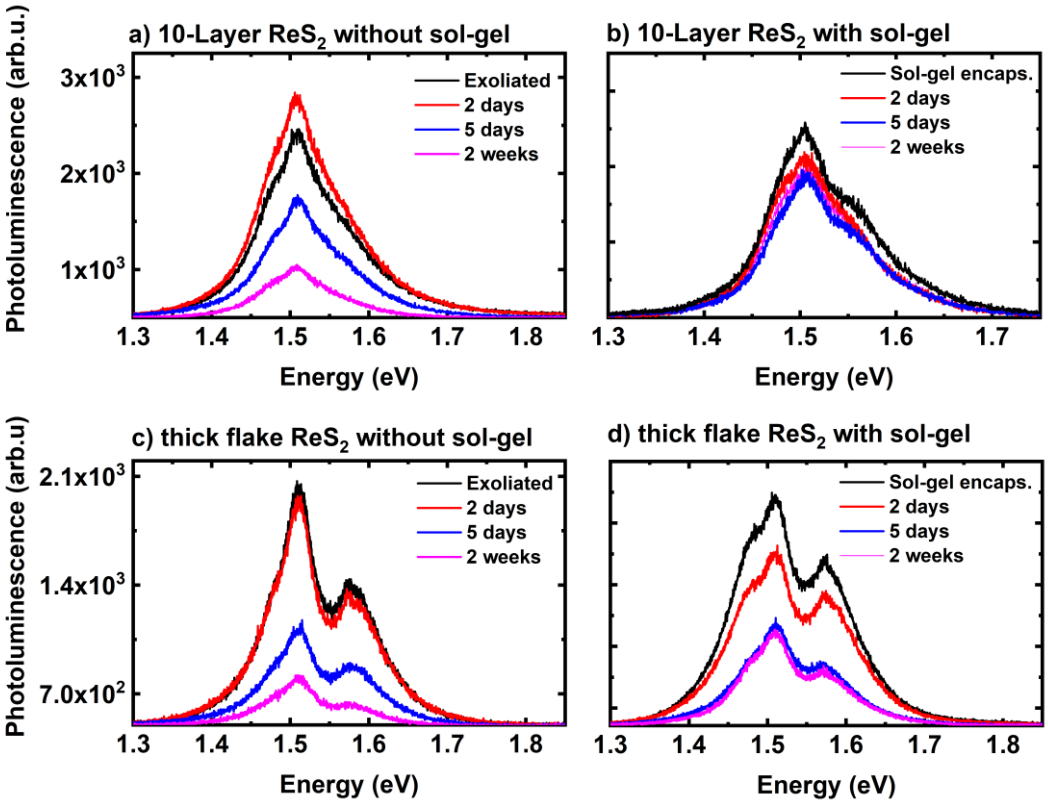

Figure 6.24. Photoluminescence study of encapsulated ReS_2 flakes for: a) 10-Layer ReS_2 without sol-gel; b) 10-Layer ReS_2 with sol-gel; c) Thick flake ReS_2 without sol-gel; c) Thick flake ReS_2 with sol-gel.

For 10-Layer and thick flake without sol-gel, the photoluminescence decreases linearly (Figures 6.24a and c). After sol-gel encapsulation of ReS_2 flakes, the photoluminescence is slightly decreased after just 2 days of oxidation. However, after five days of ambient exposure we can see that PL signal does not decrease and remains at the same level (Figures 6.24b and d). As conclusion, after sol-gel encapsulation, the $HfSe_2$ and ReS_2 flakes are slightly oxidized due to presence of H_2O at sol-gel, which causes a decrease in photoluminescence, after the sol-gel layer was applied. However, when the sol-gel was hardened and the water evaporates, photoluminescence decrease was stopped what was visible after the 5 days of oxidation.

7 Fabricated sol-gel SiO_x:TiO_y microcomponents

The schematic of sample preparation is showed on Figure 7.1. For samples fabrication was used substrate as sol-gel SiO_x:TiO_y on SiO_2/Si, where SiO_2 thickness is 3 µm. Cleaning the substrate was carried out in solutions of acetone, isopropanol and DI water. Each sample was characterised by a few methods:

1) Thickness measurements by using Bruker profilometer with stylus 100 nm.
2) Microstructure quality, smoothness, surface verification by Scanning Electron Microscope Helios 660; cross-sections realization by using Focused Ion Beam (FIB).

3) Defects inspection and quality checking by Leica and Keyence optical microscopes.

On a first stage, each sol-gel precursor solution was used for fabrication the sol-gel structures by NIL technique. The appropriate sol, which gives the maximum height and width of the waveguide was selected. Exemplary comparison of waveguide parameters obtained using a mixture of SiO_x:TiO_y sol and only sol with TiO_x content (Figure 7.1). A detailed description of the manufactured waveguides and their applications is included in publication ***P2***.

The TiO_x sol-gel, however, has a higher refractive index (n ≈ 2.05), but it is difficult to produce high and wide waveguides from this sol due to the high viscosity of the solution. Therefore, sol-gel SiO_x:TiO_y was used to produce all structures in this thesis. Examples of fabricated waveguides by NIL technique are shown in Figures 7.2-7.3.

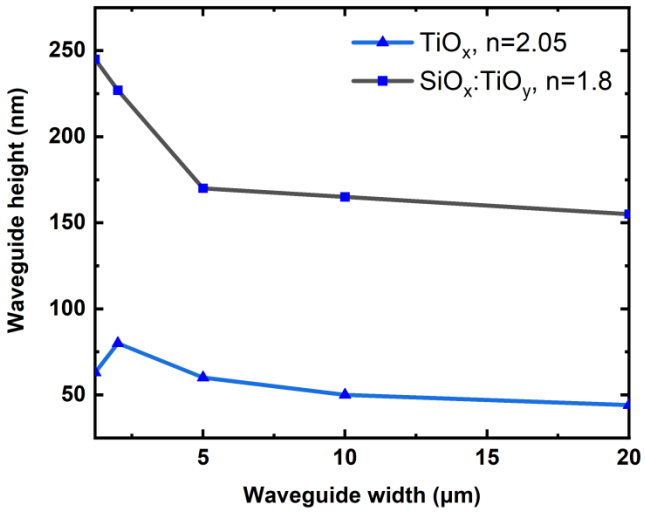

Figure 7.1. Comparison of waveguide parameters, obtained using a SiO_x:TiO_y and TiO_x sol-gels, where n is refractive index of sol-gel.

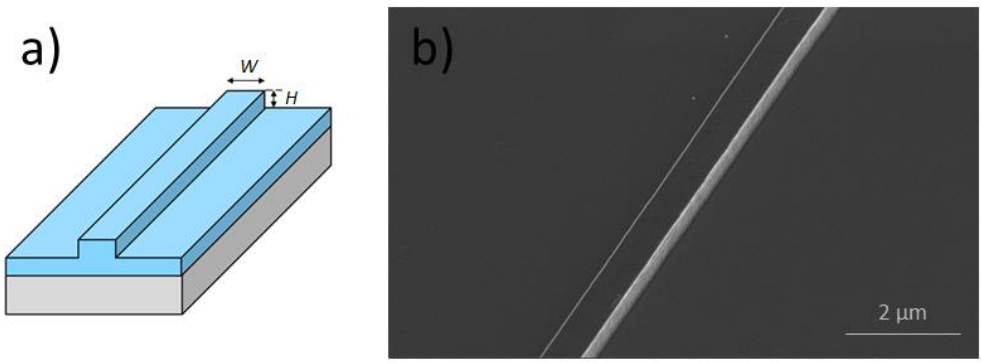

Figure 7.2. a) Schematic drawing of waveguide parameters (W – waveguide width, H – waveguide height); b) SEM image of fabricated waveguide.

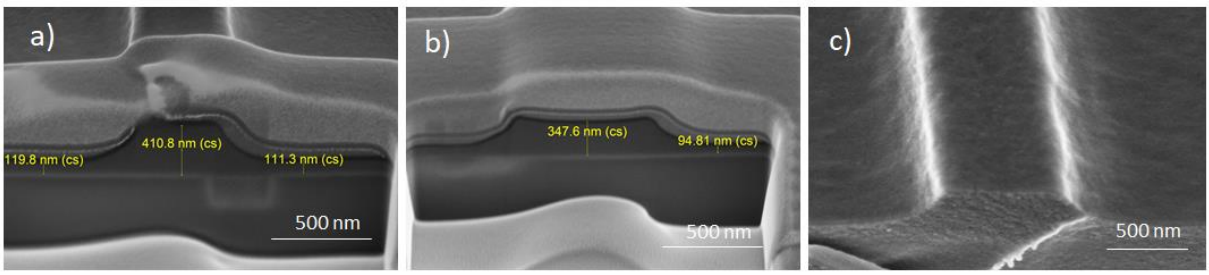

Figure 7.3. Waveguide cross-section: a) 1.2 µm wide waveguide; b) 2 µm wide waveguide; c) Waveguide cutting edge (1.2 µm).

After characterization of the microstructures, obtained by NIL, the second technique (photolithography and dry etching) was used to make a comparison of which technique is more suitable for producing target structures for the devices. Schematic of sample preparation using photolithography process is shown in Figure 7.4.

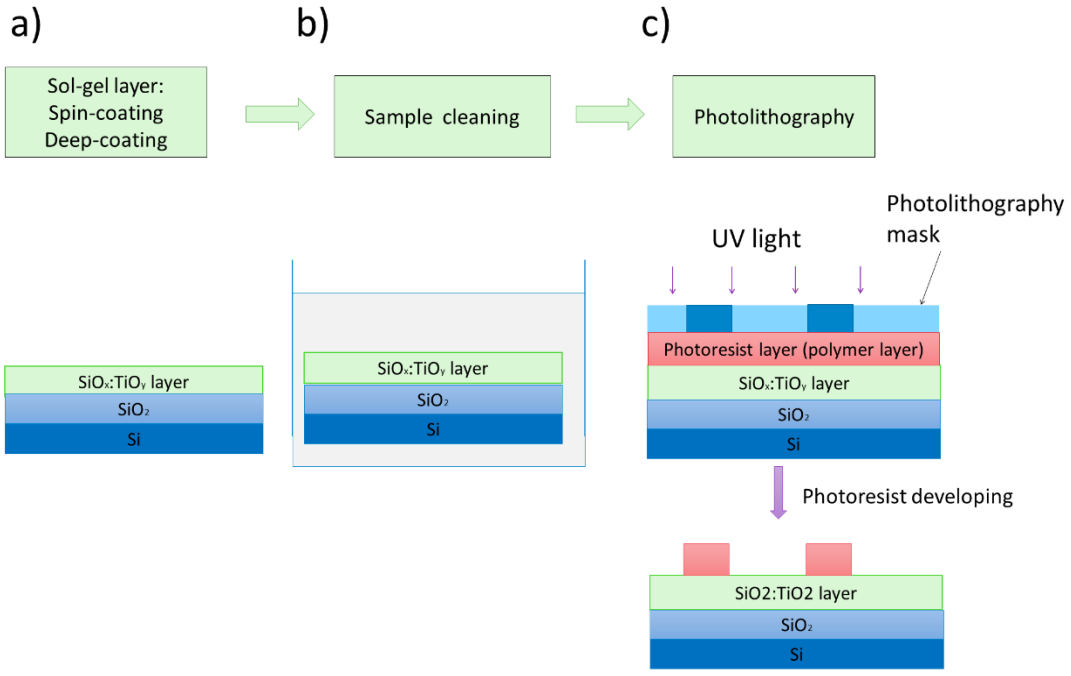

Figure 7.4. Schematic of sample preparation: a) Sol-gel coating on SiO_2/Si; b) Sample cleaning; c) Photolithography process with later photoresist developing.

The mask design, which include waveguide shapes, microdiscs and contact pads, was created in KLayout software (Figure 7.5). Examples of photoresist structures obtained with photolithography by using the previously prepared mask are shown on Figure 7.6.

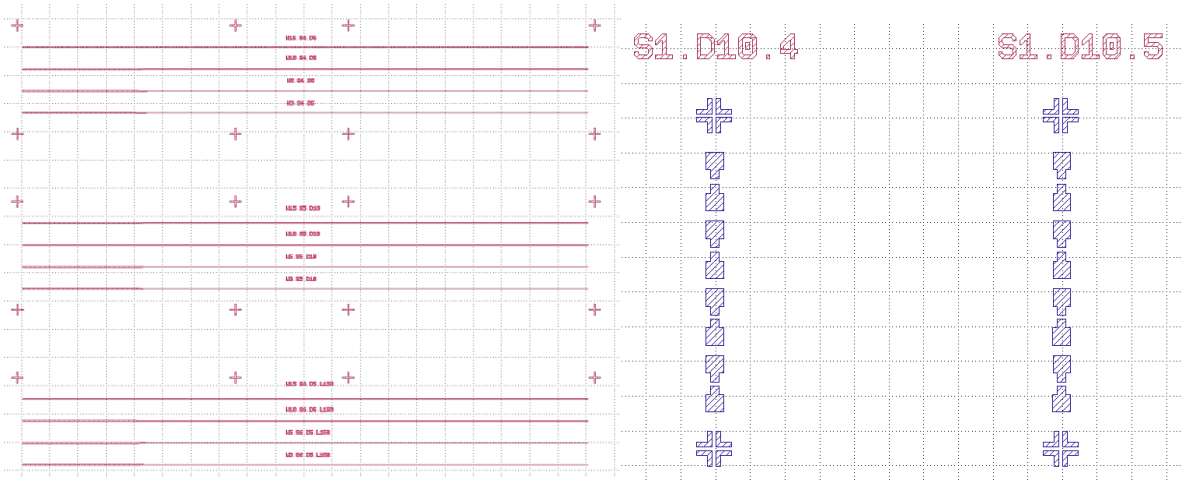

Figure 7.5. Preview of the created design for photolithography mask.

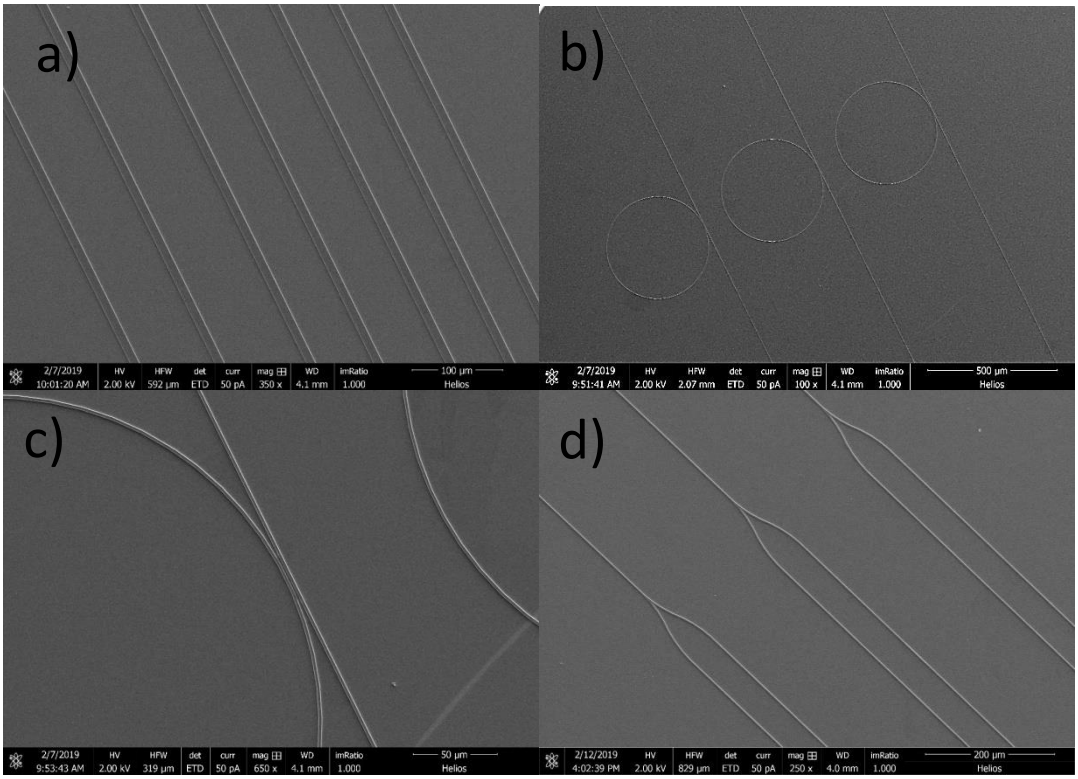

Figure 7.6. SEM images of photoresist structures obtained with photolithography: a) Set of waveguides; b) Set of ring resonators; c) Magnification of gap between waveguide and ring; d) Waveguide multiplexing components.

7.1 Fabrication and characterisation of microdiscs

For the applications described above, samples with microdiscs were prepared as follows. Each sample was covered by sol-gel layer with maximum thickness of 0.3 µm. The microdisc fabrication starts from photolithography process (Figure 7.7); wet etching in buffered oxide etch (BHF) or potassium hydroxide (KOH) solution; Rhodamine 6G dye

impregnation (Figure 7.8). After impregnation, emission and photoluminescence were measured for each sample.

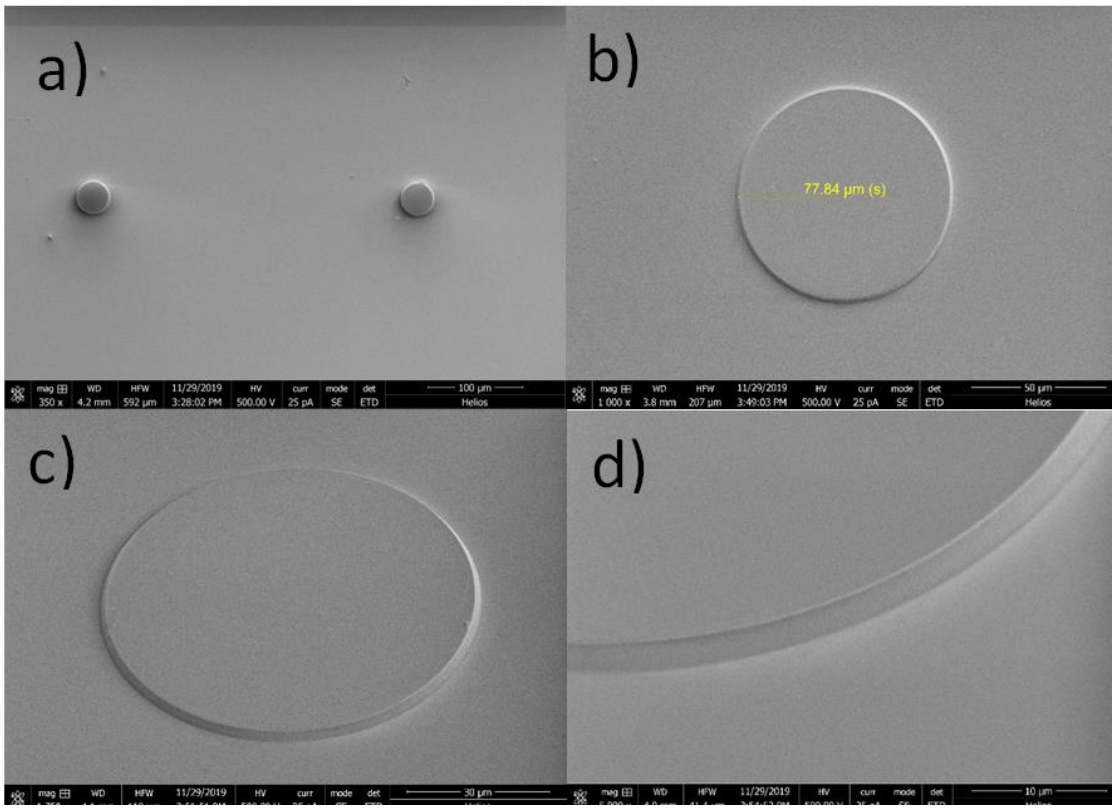

Figure 7.7. SEM images of microdiscs after photolithography process: a) View on set of microdiscs; b) Photoresist microdisc structure (view from the top); c) Photoresist microdisc structure (view from the tilt); d) Zoom on the side wall of the photoresist.

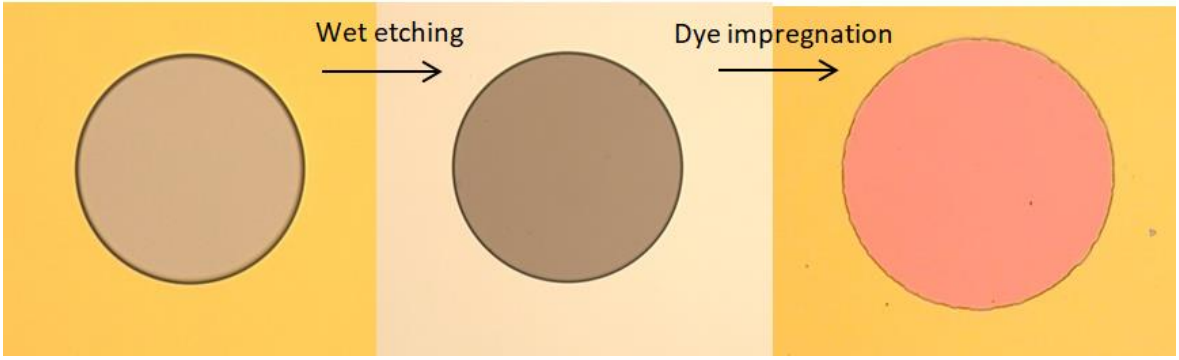

Figure 7.8. Microdisc fabrication steps: photolithography-wet etching-dye impregnation.

After photolithography process, the SiO_x:TiO_y sol-gel layer was etched in BHF or KOH solution. Photoresist, in this case, was used as mask for etching the sol-gel layer. The SiO_2 layer under sol-gel was also etched to a depth of approx. 0.5 µm, resulting in the microdisc pedestal (Figure 7.9). The total etched thickness is 1.083 µm (Figure 7.10).

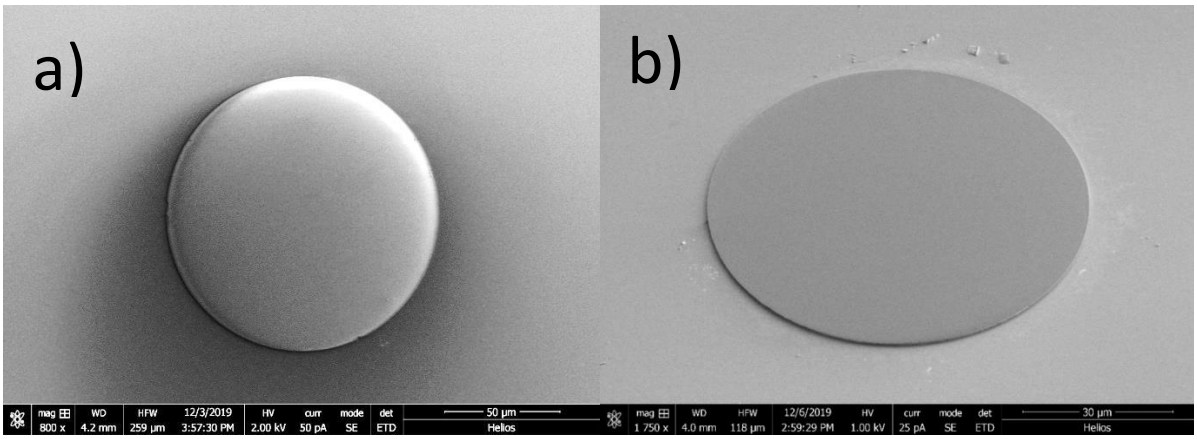

Figure 7.9. SEM images of etched microdisc in BHF solution a) View from the top; c) View from the tilt.

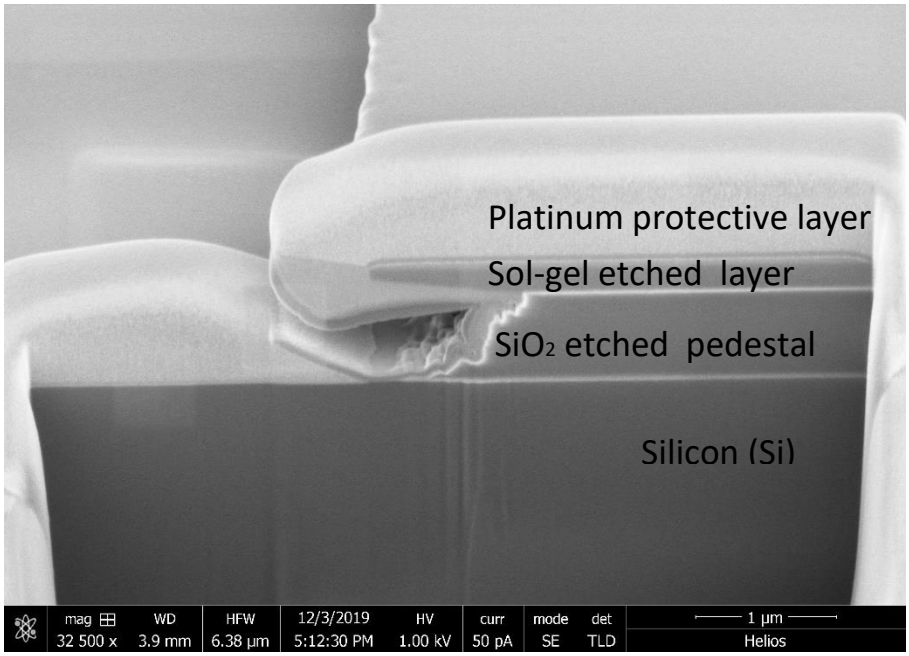

Figure 7.10. Cross-section of microdisc etched in BHF solution.

To obtain the photoluminescence from a microdisc, the impregnation of Rhodamine 6G (Rh6G) into sol-gel layer was applied.[184-185] The Rhodamine dye was immersed in Methanol (MeOH) at concentration of 10^4 g/ml. For Rh6G the maximum of photoluminescence is located at 568-570 nm. For all impregnated microdiscs the emission spectra were measured. The maximum of photoluminescence is observed at 550 nm (Figure 7.11). An efficient laser emission is detected when the samples was pumped at 532 nm.

For dye impregnation into sol-gel SiO_x:TiO_y a few methods was tested:

1) Impregnation of Rh6G in vacuum, where the sample was coated with Rh6G in low vacuum.
2) Impregnation of Rh6G by using ultrasonification (US) during 10/20/30 minutes.

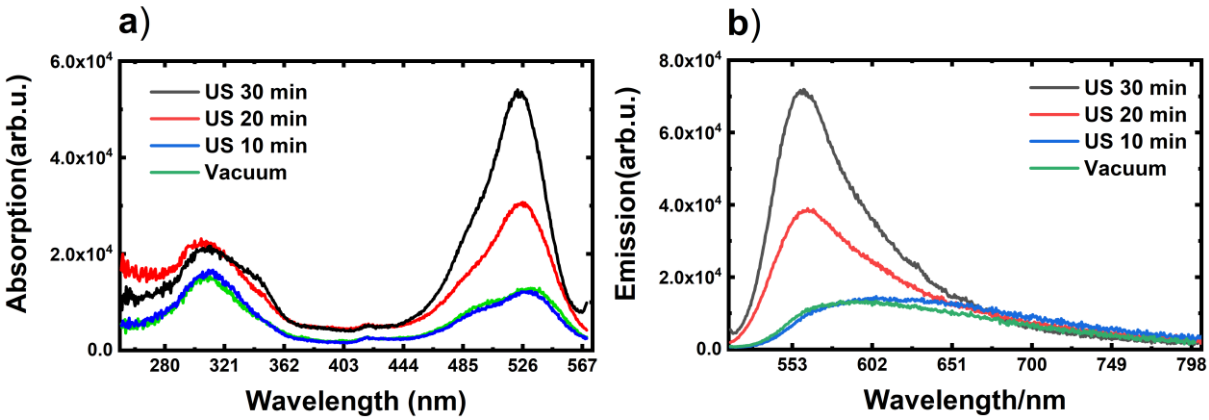

Figure 7.11. Comparison of photoemission for each impregnation method.

By analysing the two impregnation methods, the highest peak of Rhodamine absorption and emission was measured for impregnated sample by US during 30 minutes. Additionally, a few samples was etched in KOH solution, where etching process is about a two times faster (Figure 7.12-7.13).

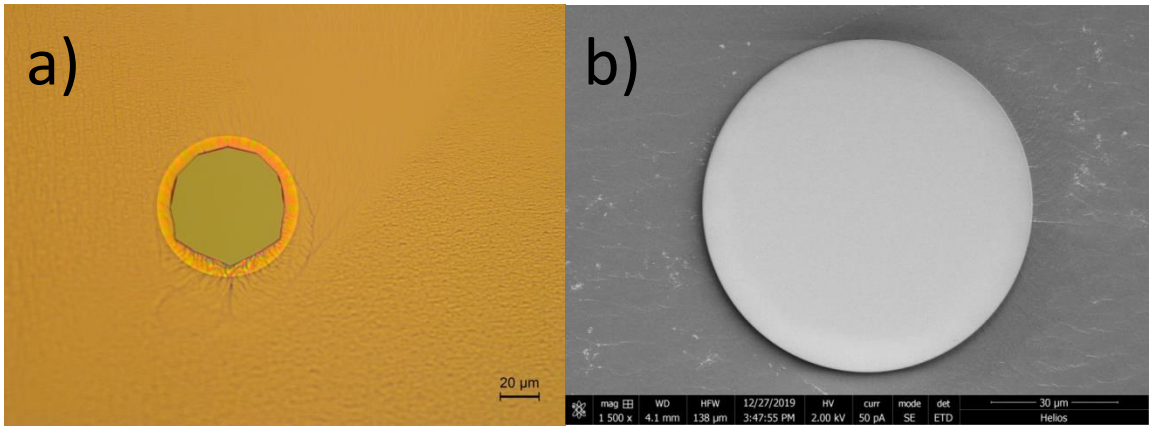

Figure 7.12. a) Image of etched microdisc in KOH solution (view from the top); b) SEM image of sol-gel microdisc structure (view from the top).

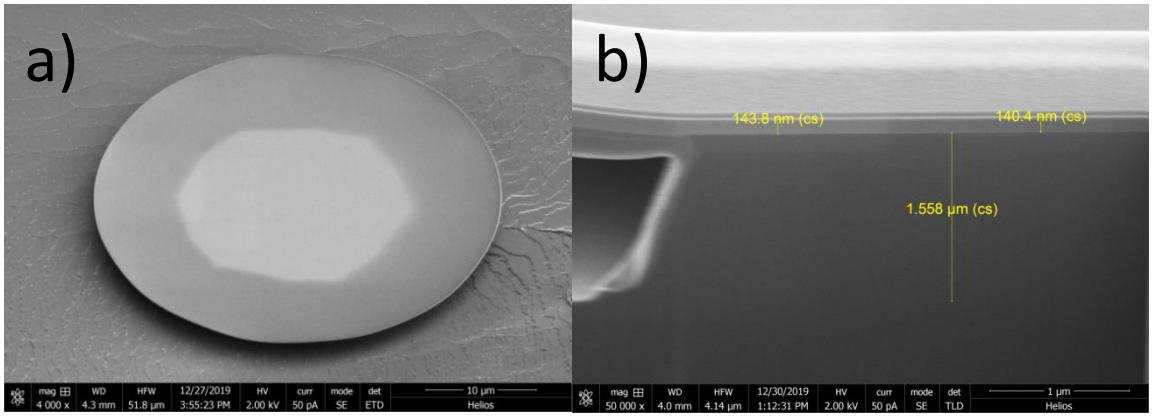

Figure 7.13. a) Image of etched microdisc in KOH solution (view from the tilt); b) Cross-section of microdisc etched in KOH solution.

7.1.1 Microdisc emission measurements

Microdisc emission was measured for fabricated microdiscs with diameter of 80 µm and height 1.0-1.5 µm. Figure 7.14-7.15 represent microdisc emission spectra for etched structure in BHF and KOH solutions.

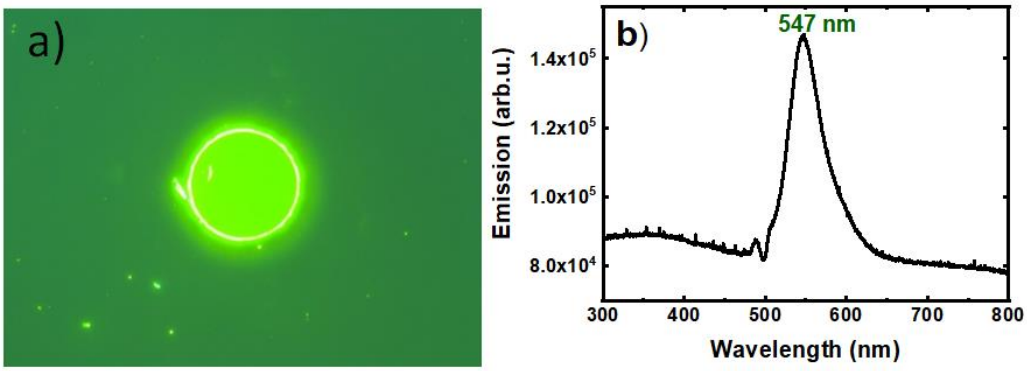

Figure 7.14. a) Microdisc emission for etched structure in BHF solution (image from fluorescent microscope); b) Microdisc emission signal.

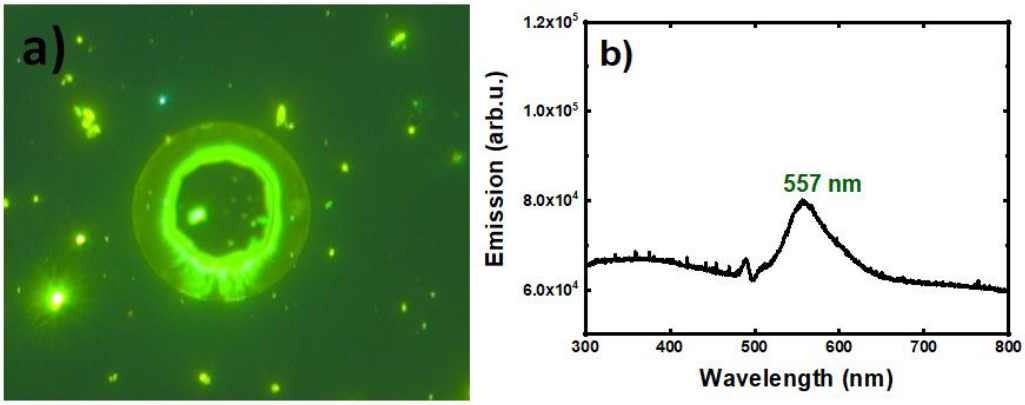

Figure 7.15. a) Microdisc emission for etched structure in KOH solution (image from fluorescent microscope); b) Microdisc emission signal.

For both types of microdiscs, emission is visible on fluorescent microscope (Figure 7.14-7.15). The maximum of wavelength emission is located at 547 (etched in BHF) and 557 nm (etched in KOH). The emission signal from microdiscs, etched in BHF, is stronger due to emission from all microdisc area. Whereas, in structure etched in KOH solution the edges of disc are very thin and emission is visible only near the pedestal, where sol-gel layer is thicker (Figure 7.15a).

The fabricated microdiscs were pumped by laser wavelength of 532 nm. Figure 7.16 represent rays of light propagation in fabricated microdisc with diameter about 80 µm. WGM modes were visible at the edge on microdisc, where light is reflected. However, the edge of the disk is not smooth enough, especially after the KOH etching, which may reduce the amount of modes in the structure. To improve the smoothness of the edges, a thicker layer of sol-gel must be used to fabricate such microstructures. However, even for a thin sol-

gel layer (0.3 µm), we showed that microdiscs works and this technology can be applied for further development.

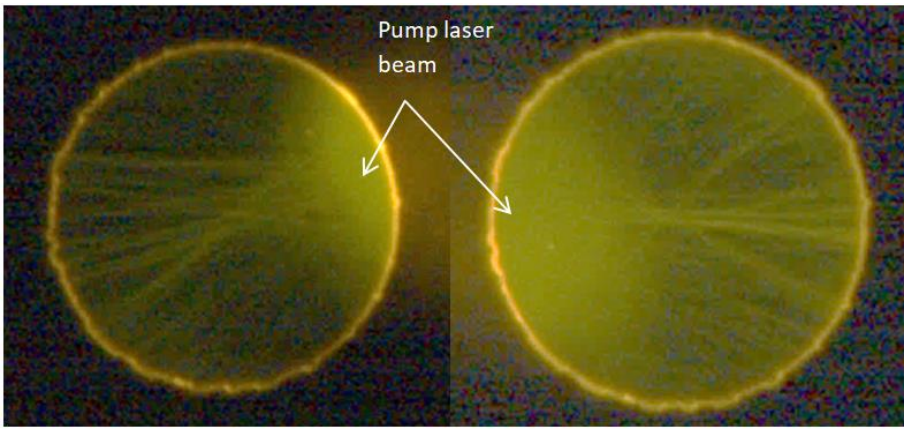

Figure 7.16. Rays of light propagation in fabricated microdiscs. Presented WGM modes for microdisc etched in BHF solution.

7.2 Fabrication and characterisation of etched waveguides

In work, the planar sol-gel SiO_x:TiO_y waveguides (WG) were used as the main component for planar device fabrication. A series of waveguides were fabricated by photolithography and plasma dry etching techniques (Figure 7.17). The etched thickness was varied from 0.1 to 0.3 µm.

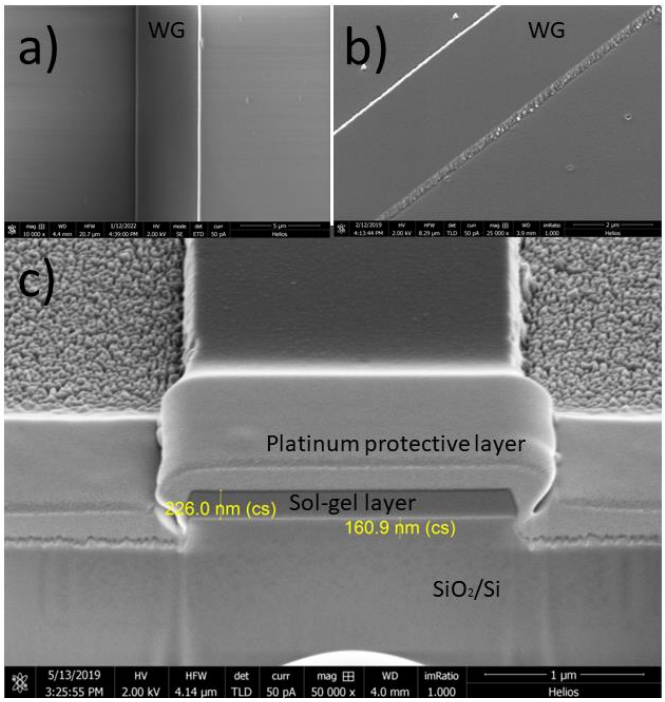

Figure 7.17. SEM images of etched waveguide: a) View of the etched waveguide from the top; b) View of the etched waveguide from the tilt 45°; c) Waveguide cross-section (for clarity, each layer on image has been appropriately signed as platinum protective layer, etched sol-gel layer, SiO_2/Si substrate).

7.2.1 Waveguide transmittance measurements

For waveguide transmittance measurements the experimental setup was made (Figure 7.18). After transmittance measurements, the quality of fabricated waveguides was verified. As light source for waveguide excitation was used the broadband Thorlabs source with multimode (MM) or single mode (SM) fiber. The one end of fiber is placed on *XYZ* stage, and applied for WG excitation and microscope with objective 40x was used for output image magnification and CCD camera for mode detection.

Sol-gel waveguide guides only visible light due to its dimensions and optical properties of sol-gel material. Therefore, the rest of the input wavelength from the source is cut out. The main difference between excitation sources consist in intensity of light power (Table 9), where the supercontinuum source has the more intensive excitation. The supercontinuum source excites of a few waveguides at the same time. In turn, broadband source and single mode fiber was used for excitation of single waveguide (Figure 7.19).

Table 9. Waveguide excitation sources.

Source	Power	Excitation
Supercontinum	mW	Objective 40x, collimated beam.
Broadband source Thorlabs and multimode fiber	pW	Multimode fiber, core diameter 50 um.
Broadband source Thorlabs and single mode fiber	pW	Single mode fiber, core diameter 5 um.

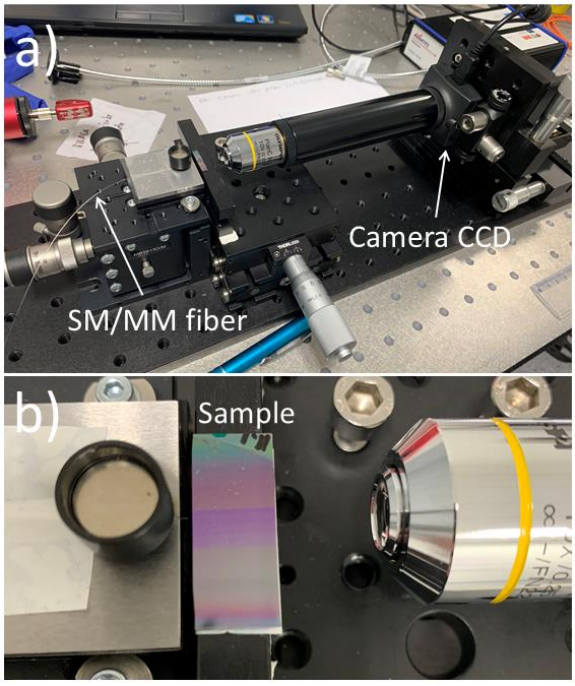

Figure 7.18. Experimental setup for waveguide excitation: a) View on CCD camera with 40x objective; sample stage; Thorlabs broadband source with SM/MM fiber; b) Zoom on sample with 40x objective.

The reference sample was fabricated with SU-8 photoresist which characterised by quite height optical properties, see Figure 7.19. Waveguide set excitation was performed using the three excitation methods. For measuring fabricated sol-gel waveguides the excitation with broadband source and SM fiber was applied due to selective coupling (Figure 7.20).

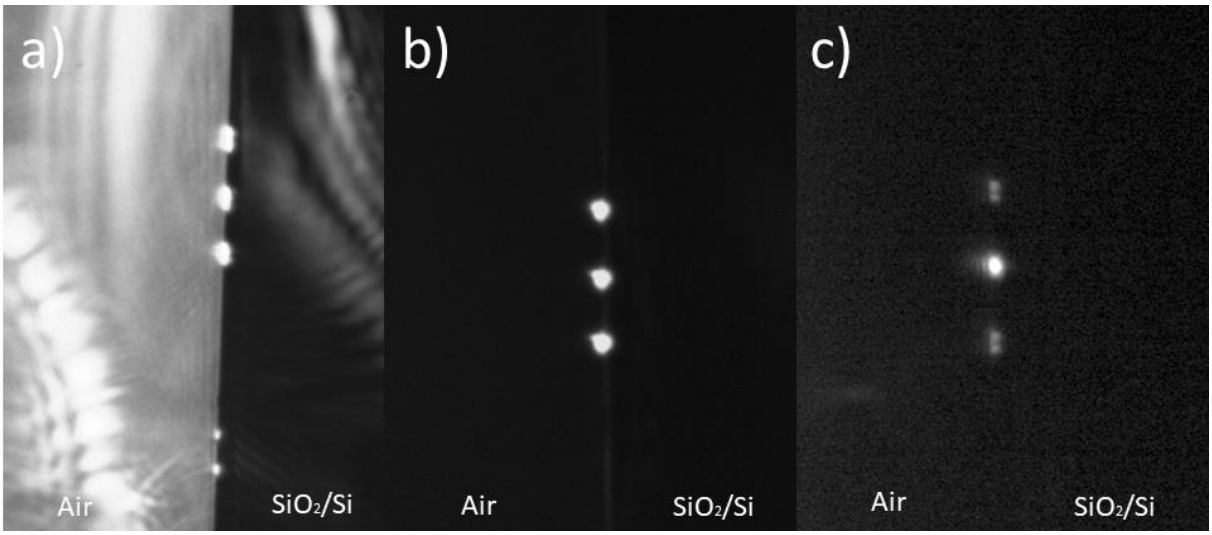

Figure 7.19. Output signal from excited SU-8 waveguides. On image a set of waveguides were coupled (H = 1 µm and W = 5 µm) by using the excitation source: a) Supercontinum; b) Broadband source Thorlabs and multimode fiber; c) Broadband source Thorlabs and single mode fiber.

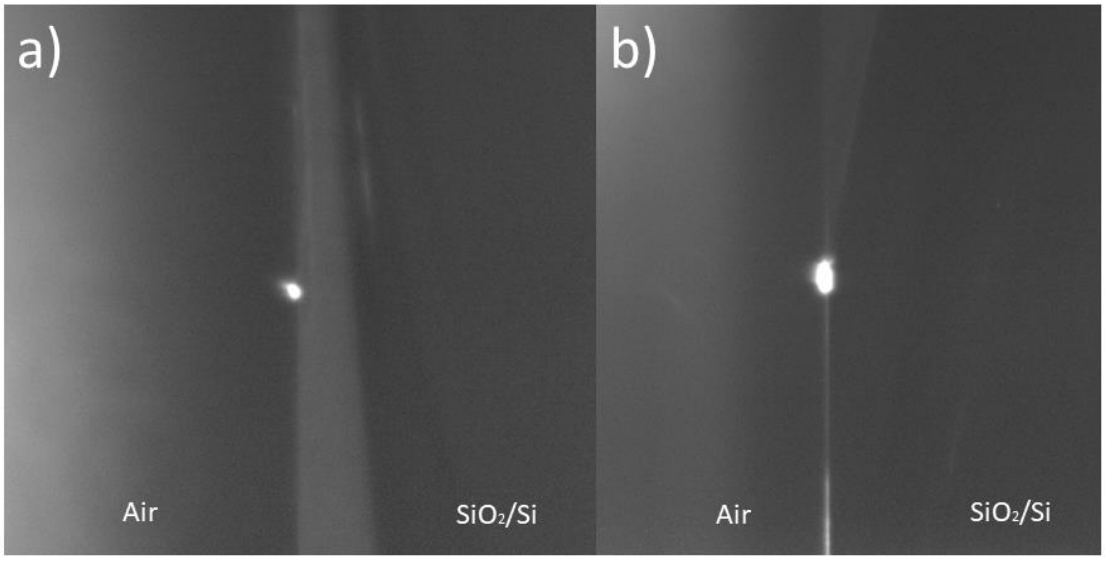

Figure 7.20. Comparison of output signal from sol-gel SiO_x:TiO_y waveguide: a) W = 5 µm; b) W = 20 µm.

Each sample contains a few sets of WG with different width, beginning from 1.2 to 20 µm. Such a large spread of width will allow to study the distribution of modes and their output signal. The thickness of the waveguides was unchanged and amounted to maximum of 0.3 µm. For each WG the width and transmittance were checked, see Figure 7.21.

Experimental measurements show that the brightest transmittance is visible for a 20 µm waveguide (Figure 7.21g).

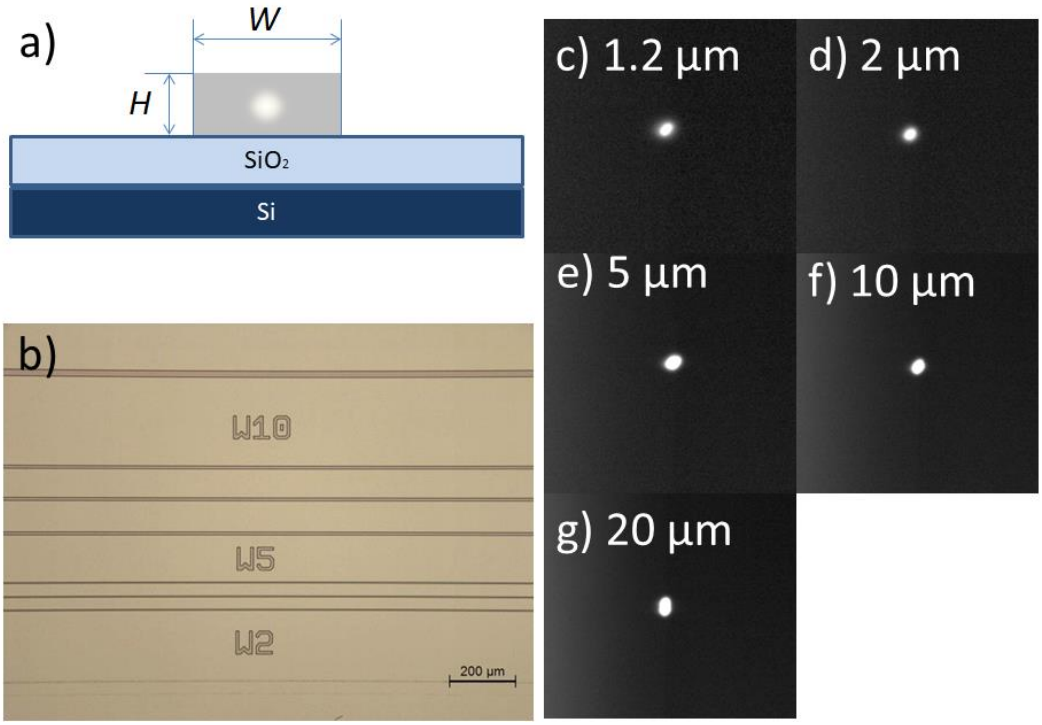

Figure 7.21. a) Schematic waveguide cross-section; b) Set of waveguides (image from optical microscope). Optical mode pattern in a planar sol-gel waveguide: c) 1.2 µm; d) 2 µm; e) 5 µm; f) 10 µm; g) 20 µm.

7.3 Integration of MX_2 materials with sol-gel waveguides

In this section, the preliminary results of research on the combination of MX_2 materials with sol-gel waveguides were presented. The first tests on integration of fabricated photonic microstructures were started with exfoliation and transfer of MX and MX_2 flakes on a top of fabricated structures (Figures 7.22-7.23).

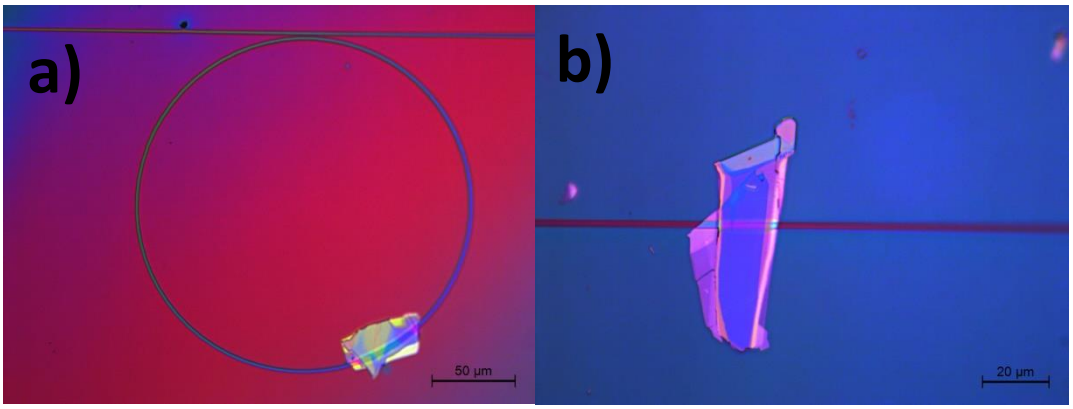

Figure 7.22. Images of transferred MX_2 flakes on top of: a) Sol-gel ring resonator; b) Sol-gel waveguide.

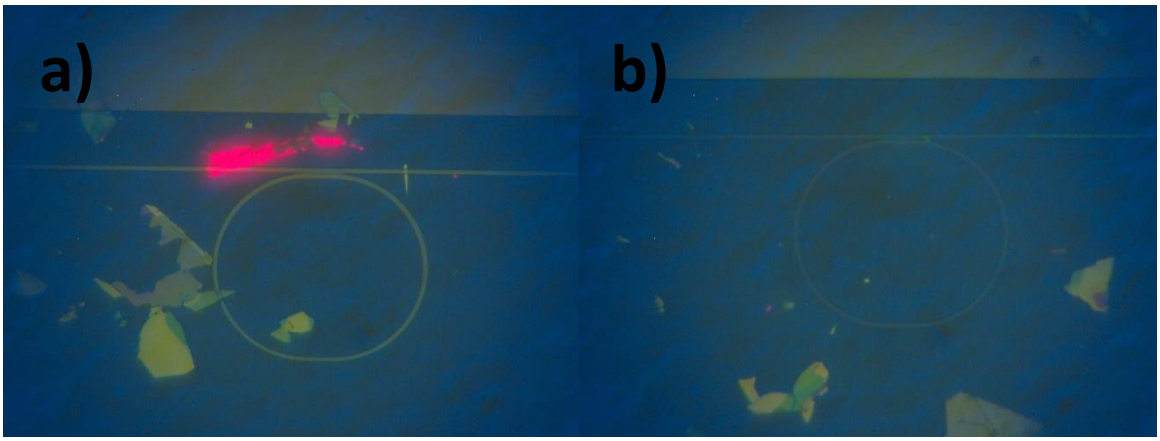

Figure 7.23. a) Image from fluorescent microscope of transferred WS_2 monolayer on top of waveguide-ring resonator; b) Image from fluorescent microscope of structure waveguide-ring resonator without WS_2 monolayer.

For Raman and PL measurements MoS_2 and WS_2 bilayers were transferred directly on top of sol-gel waveguides (Figures 7.24 - 7.26). In case of MoS_2 and WS_2 on waveguide, the PL signal is stronger and shifted towards the lower energies (Figure 7.24b and Figure 7.25c). Stronger signal could be related with enhanced PL light due to the presence of a waveguide underneath. A particularly stronger PL signal is visible on the side walls of the waveguide under WS_2 (Figure 7.25b). The performed experimental measurements confirms the light-matter interaction of applied material with the fabricated photonic structure.

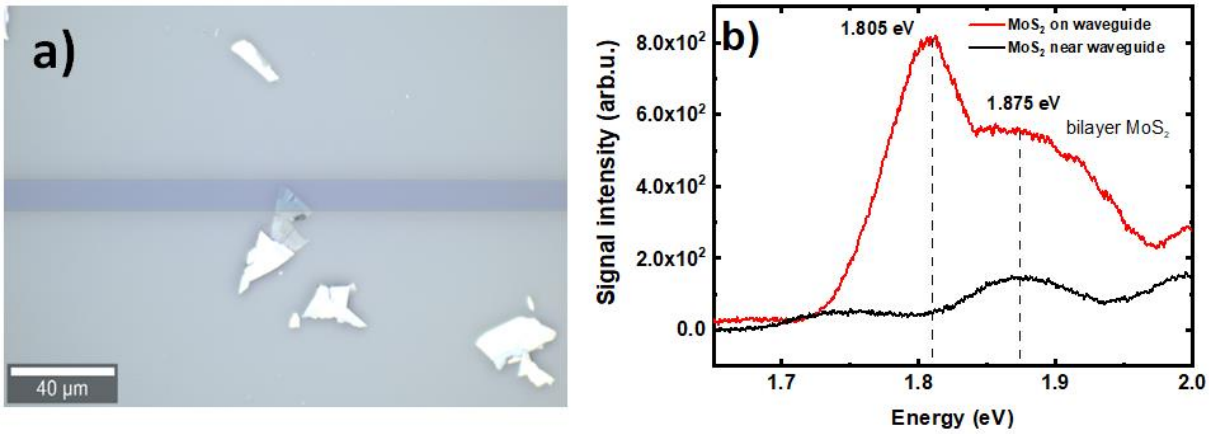

Figure 7.24. MoS_2 2-L on top of sol-gel waveguide: a) Image from optical microscope; b) Photoluminescence spectra for bilayer MoS_2 on waveguide.

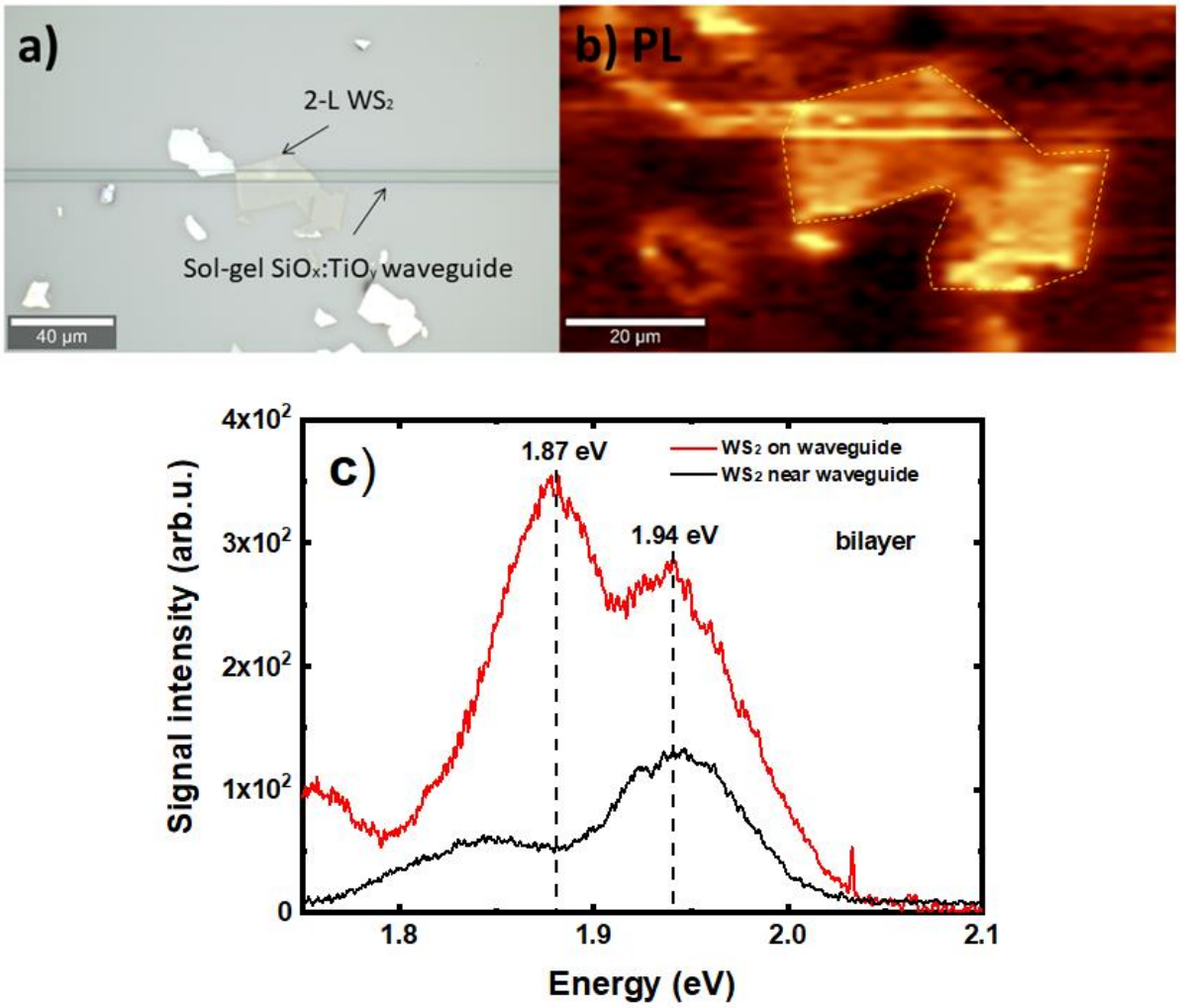

Figure 7.25. WS_2 1-L on top of sol-gel waveguide: a) Image from optical microscope; b) Photoluminescence map for WS_2/waveguide; c) Photoluminescence spectra for bilayer WS_2 on waveguide.

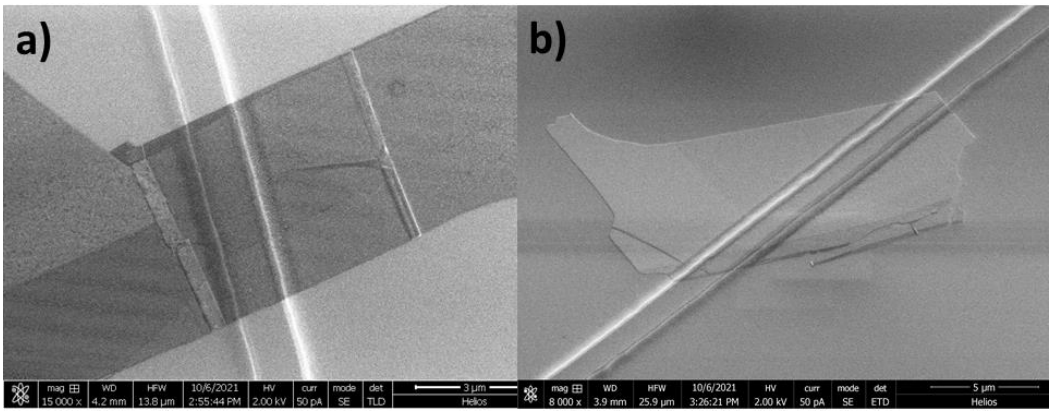

Figure 7.26. SEM images of WS_2 on waveguide: a) Few-layer; b) Thick flake.

7.3.1 Simulation of integration of MoS_2 flake with sol-gel ring resonator.

The simulation of applying MoS_2 layers with varied thickness on top of the planar waveguide was performed in the COMSOL Multiphysics software. Examining the impact of placing MoS_2 flake on top of the waveguide will allow to track the changes in waveguide mode distribution. In this simulation, only the TE_{00} mode was taken into account where the main purpose of simulation is to monitor how the mode distribution changes with thickness of the MoS_2 flake.

During the simulation, the effective mode index method (EIM) was used. The computational algorithm itself is based on conversion of the initial 3D waveguide structure into an analogous 2D structure, in which the wave propagation in the "reduced" dimension is described by the effective refractive index.[187] The EIM is used for wave confinement in depth direction of the waveguides, thus effective indices of the guided modes are computed. Table 10 presents the parameters for model in COMSOL. The cross-section of the model is shown in Figure 7.27.

Table 10. Model parameters for simulation: *design wavelength* – working ring resonator wavelength; *core width (w_core)* - width of sol-gel waveguide; *core refractive index (n_core)*- sol-gel refractive index; *cladding refractive index (n_clad)* - refractive index of air; *core height* - height of the sol-gel waveguide.

Design wavelength (wl_0)	**Core width (w_core)**	**Cladding width**	**Radius of ring resonator**
1.55(µm)	1(µm)	w_clad 10*w_core	r0 4*wl_0
Spacing between waveguide and ring resonator	**Core refractive index (n_core)**	**Cladding refractive index (n_clad)**	**Core height**
dx 3.5833*w_core	1.8	1.455	0.2(µm)
MoS_2 thickness	**MoS_2 refractive index**		
0.7 (nm)	3.8256		

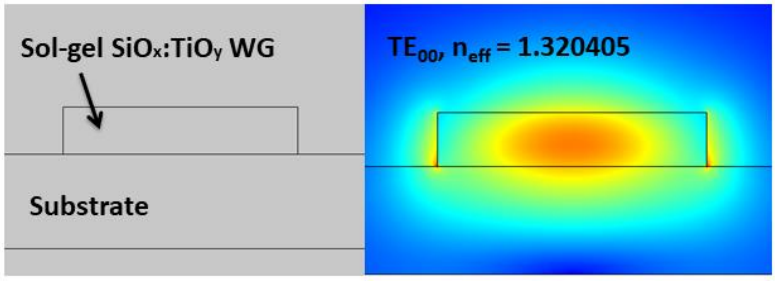

Figure. 7.27. Cross-section (2-D) of the sol-gel SiO_x:TiO_y waveguide without the MoS_2 flake and TE_{00} mode.

The field distribution of the TE_{00} mode is shown in Figure 7.28. In simulation the thickness of MoS_2 was varied from 5 to 25 nm. Analyzing the field distribution of the mode, when the thickness of the MoS_2 flake increases, we see that at a thickness of 25 nm the

mode is no longer located in the sol-gel waveguide, but only close to the flake. This effect is mainly caused by the high refractive index of the MoS_2 flake ($n \approx 3.8$), compared to the refractive index of the sol-gel ($n \approx 1.8$).

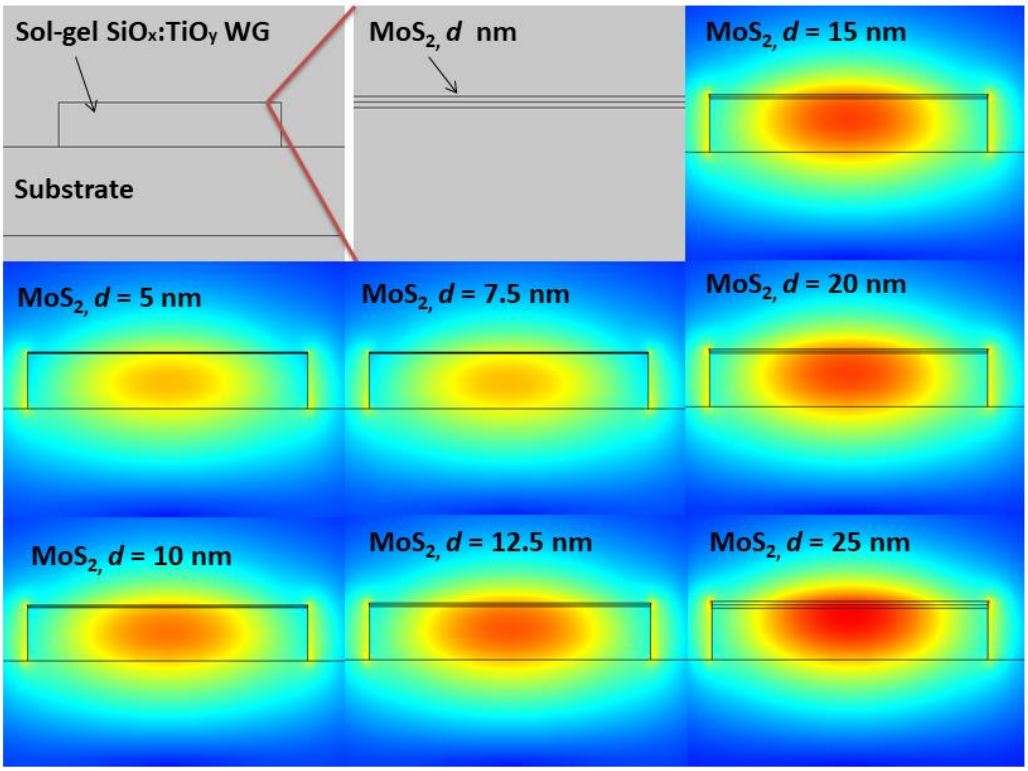

Figure. 7.28. Field distribution of the TE_{00} mode in sol-gel SiO_x:TiO_y waveguide with MoS_2 flake (d = 5, 7.5, 10, 12.5, 15, 20, 25 nm).

Table 11 shows the calculated effective mode indices for various flake thickness. The dependency graph is shown in Figure 7.29.

Table 11. The calculated effective mode indices for TE_{00} mode.

MoS_2	**0.7 nm**	**2.5 nm**	**5.0 nm**	**7.5 nm**	**10 nm**
n_{eff}	1.3249499116174	1.3240595049559	1.35449892990619	1.37309372938747	1.39271185991315
d	**10 nm**	**12.5 nm**	**15.0 nm**	**20 nm**	**25 nm**
n_{eff}	1.39271185991315	1.4133488268534	1.43495232167761	1.48106467854841	1.53079115519287

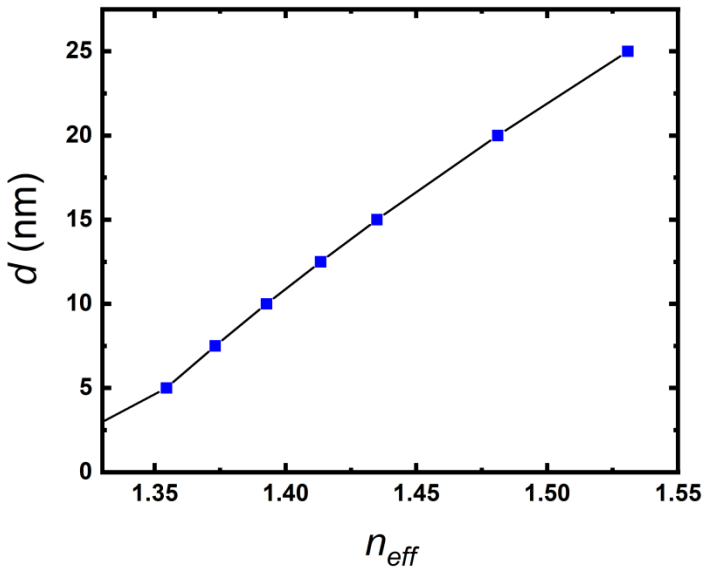

Figure 7.29. Dependence of the effective mode index on the thickness of the applied MoS_2 flake.

After calculation the effective mode indices, the operation of the ring resonator was simulated (Figure 7.30). After coupling light into the sol-gel waveguide, the part of light passes into ring resonator, which indicates that the parameters of our model are well selected.

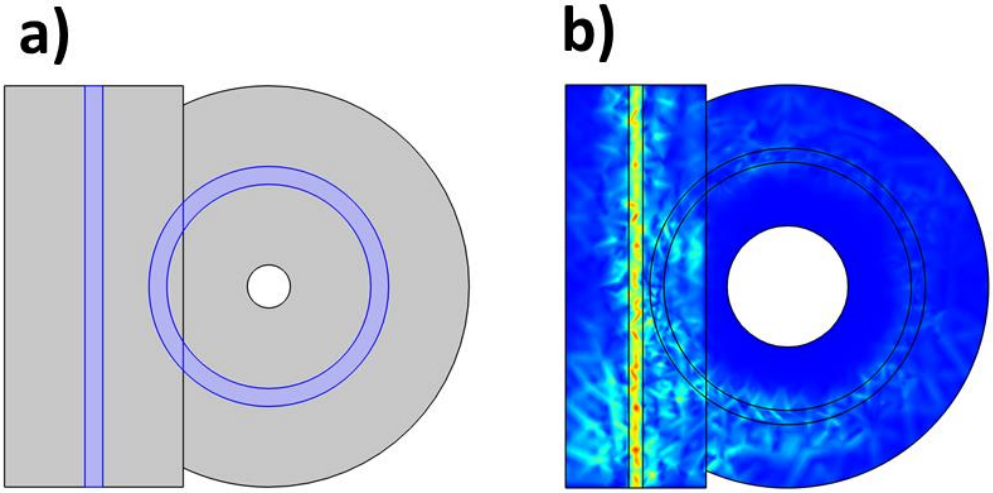

Figure 7.30. 2D model of sol-gel ring resonator: a) View from the top on 2D model of the ring resonator; b) Preview of the sol-gel waveguide excitation and the coupling effect in ring resonator.

8 Electrical contacts engineering to the three- and two-dimensional semiconductors

For study the metal contacts engineering, metals with different work-functions (Ti, Au, Pd, Pt, Cr, Al, Ag) were deposited on commercial bulk crystals (2D Semiconductors, HQ Graphene Co.) and exfoliated thin flakes. The two approaches have been tested for producing the high-quality contacts to exfoliated MX and MX_2 flakes:

1) Electrical contacts preparation with PVD technique preceded by a laser lithography.

2) Electrical contacts preparation with Gas Injection System (GIS) and Focused Ion Beam (FIB) in Scanning Electron Microscope Helios 660.

For fabrication the electrical contacts to bulk crystals, only the PVD technique was used. Metal pads were evaporated through the special metal mask with holes of a specific shape and diameter. During the metal contact fabrication by PVD technique it is important to avoid the highly reactive metals and to precisely control the evaporation conditions. For instance, choosing a low vaporization temperature metals; using the indirect evaporation to reduce the kinetic damage of 2D semiconductor; keeping the low deposition temperature and maintaining the high vacuum during vaporization. During the metal deposition the kinetic energy transfer from metal atoms to semiconductor and heating of the device from metal evaporation appears. Therefore, controlling the evaporation parameters allows to avoid the 2D material surface degradation. A very low deposition rate (~ 0.01-0.05 nm/s) and base vacuum of 10^{-7} mbar were kept to obtain the good quality metallic contacts.

The two approaches were used for electrical contact fabrication to exfoliated MX and MX_2 layered materials (Figure 8.1). The first two methods will be described in more detail below where the third method was used to prepare contacts in devices like photodetectors.

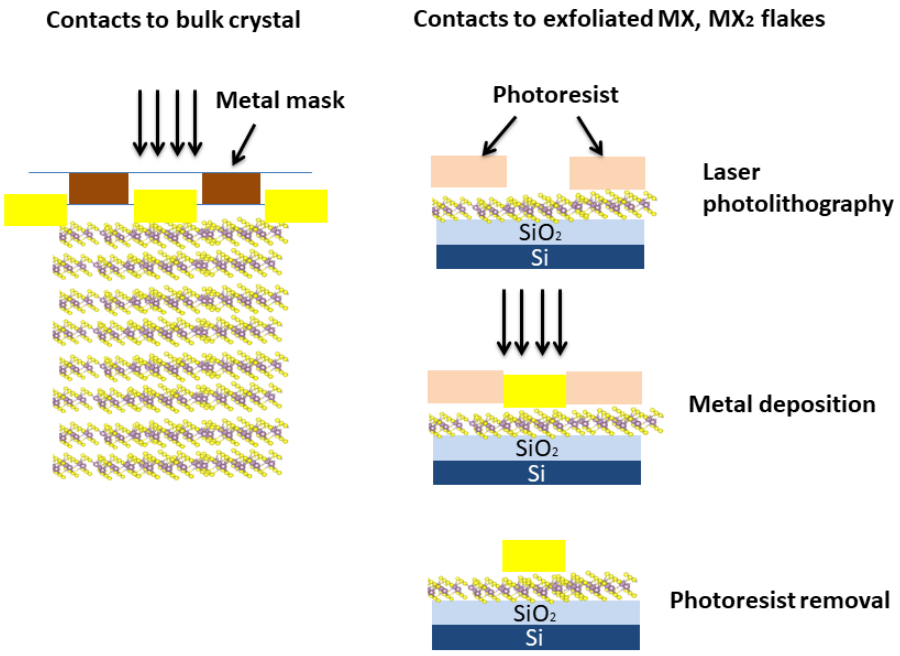

Figure 8.1. Metal contact engineering to bulk crystals and exfoliated MX, MX_2 flakes.

8.1 Electrical contacts to MX and MX_2 bulk crystals

The metal contacts were prepared on both sides of bulk crystal, where the ohmic contact was deposited from the bottom of the crystal and the Schottky from the top (Figure 8.2). The main application of the deposited contacts is to measure the number of defects in these crystals and to select the appropriate metal for Schottky/ohmic contact (publication ***P3***). The fabrication of metal contacts to the bulk crystals does not require of the pattern preparation by photolithography but only using a special metal mask with holes or shapes.

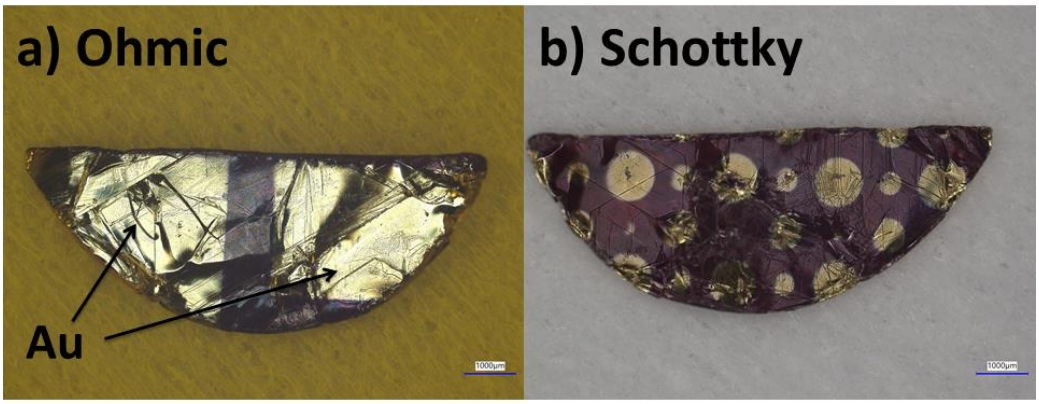

Figure 8.2. Example of fabricated ohmic and Schottky metal contacts to GeSe bulk crystal.

For the each material a few metals with different work functions were deposited on the same crystal. Table 12 presents a summary of the tested crystals and the types of obtained contacts.

Table 12. Summary of the metal contact engineering for monochalcogenides and dichalcogenides bulk crystals.

Material	**Metal (top-bottom)**	**Contact type (Schottky/Ohmic)**
Monochalcogenodes(MX)		
GeSe	Ni/Au - Au	low I & symmetric *I-V* (no Schottky or Ohmic)
	Ag/Au - Au	**Schottky**, p-type
GaSe	Ni/Au - Au	low I & symmetric *I-V* (no Schottky or Ohmic)
	Ag/Au - Au	**Schottky**,*p*-type
SnSe	Ag/Au - Au	**Schottky**,*p*-type
SnS	Ni/Au - Au	**Ohmic**, highly conductive
SnS	Ag/Au – Au	**Ohmic**, highly conductive
GeS	Ni/Au - Au	**Schottky**, *p*-type

Material	Metal (top-bottom)	Contact type (Schottky/Ohmic)
GeS	Ag/Au - Au	**Schottky**, *p*-type
GaS	Ni/Au - Au	very low I & assymmetric *I-V* (no Schottky or Ohmic)
GaS	Ag/Au - Au	very low I & assymmetric *I-V* (no Schottky or Ohmic)
GaTe	Ni/Au - Au	low I & assymetric *I-V*, (no Schottky or Ohmic), p-type
	Ag/Au - Au	low I & symmetric *I-V*, (no Schottky or Ohmic)
	Dichalcogenides(MX_2)	
MoS_2	Au-Au	**Schottky**, *n*-and *p*-type
	Pd/Au	**Schottky**, *n*-type
$MoSe_2$	Au-Au	**Schottky**, *n*-type
	Pd/Au	**Schottky**, *n*-type
	Ni/Au- Au	**Schottky**, *n*-type
$MoTe_2$	Au-Au	**Ohmic,** highly conductive
	Pd/Au	**Ohmic**, highly conductive
$SnSe_2$	Pd/Au	**Ohmic**, highly conductive
WSe_2	Au-Au	**Schottky**, *n*-and *p*-type
	Pd/Au	**Schottky**, *n*-type
WS_2	Au-Au	**Schottky**, *n*-and *p*-type
	Pd/Au	**Schottky**, *p*-type
ReS_2	Au-Au	**Schottky**
	Pd/Au	**Ohmic**, conductive
$ReSe_2$	Au-Au	**Schottky**
	Pd/Au	**Ohmic/Schottky** (dep. on contact size)

The conducted contact measurements on bulk crystals show that in the case of preparing contacts for monochalcogenides, obtaining ohmic and Schottky contact is more difficult. In some crystals it was difficult to determine the type of contact due to the low value of the passing current. In such cases, another metallization was performed. The electrical measurements of metal contacts on bulk crystals (Table 12), were carried out with the help of Lukasz Gelczuk from Department of Semiconductor Materials Engineering.

8.2 Electrical contacts to exfoliated MX and MX_2 thin flakes

In this work, a comprehensive study of metal contact engineering was performed for MX and MX_2 materials. The obtained results indicate that the performance of MX and MX_2-based devices can be further improved more effectively by selection of the matched contact metal. As part of my doctoral research, I have optimized the metal contact fabrication to minimize contamination and damage of exfoliated MX and MX_2 flakes during metal deposition. The electrical contacts to exfoliated MX and MX_2 thin flakes were obtained by using the laser photolithography for contact pattern preparation and PVD for metal deposition, followed by photoresist removal. In this fabrication process, laser photolithography offered ease of lift-off after metal deposition.

For sample preparation, the thin MX_2 flakes were exfoliated on a target sample. The polymer photosensitive layer (photoresist) was applied using a spin-coater to the top of the exfoliated flakes. Next, by using the laser photolithography, shape of the metal contact were prepared end photoresist exposed with Heidelberg Tabletop Maskless Aligner µMLA (Figures 8.3-8.4). After laser photolithography, the gold (Au) metal contacts with thickness of 100 nm were deposited by PVD technique, followed by photoresist removal (Figures 8.5-8.6).

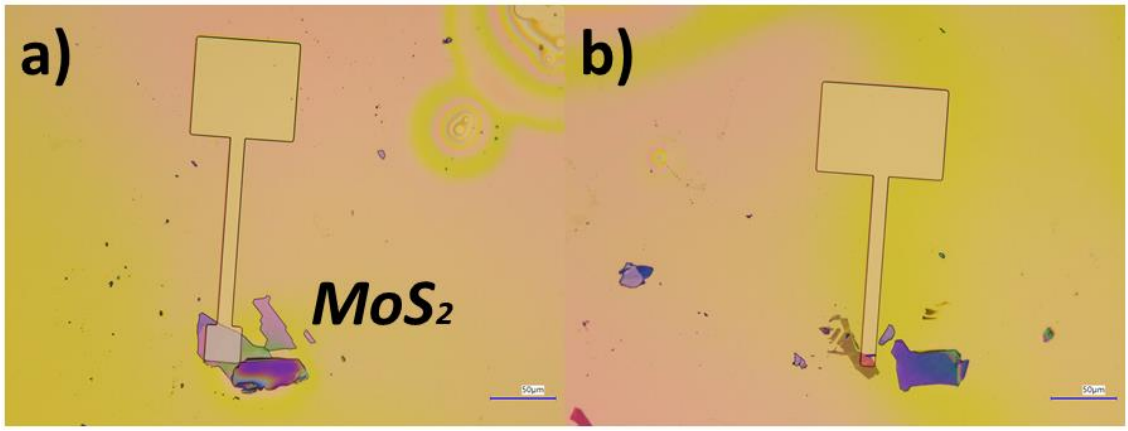

Figure 8.3. Photoresist contact shape after laser photolithography for: a) MoS_2 multilayer; b) MoS_2 few-layer.

The proposed contacts fabrication method requires only the preparation of the appropriate contact shape by laser photolithography. The advantage of laser photolithography is that this technology allows the contact pattern to be exposed directly on the exfoliated flake, without preparing an appropriate photolithography mask for exposure (Figure 8.4). Using this contact preparation method, contacts for flakes of various thicknesses were deposited, starting from few-layers to multilayers.

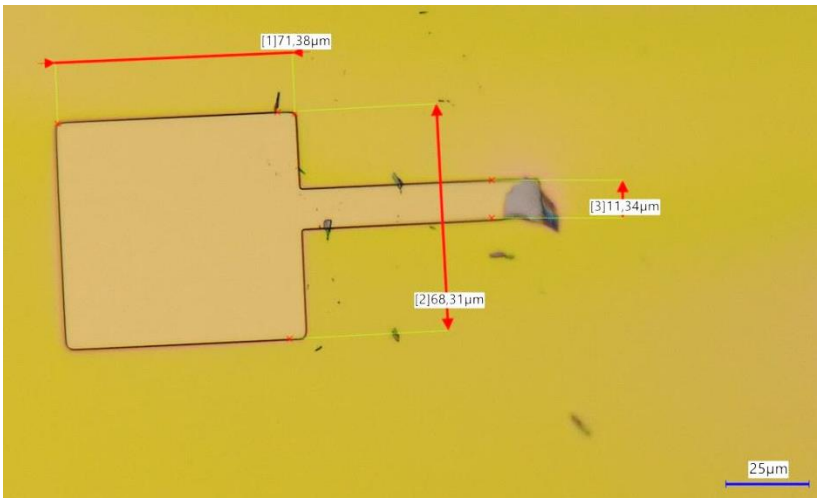

Figure 8.4. An example of a photoresist contact shape exposed by laser photolithography. The arrows indicate the measured contact dimensions in µm.

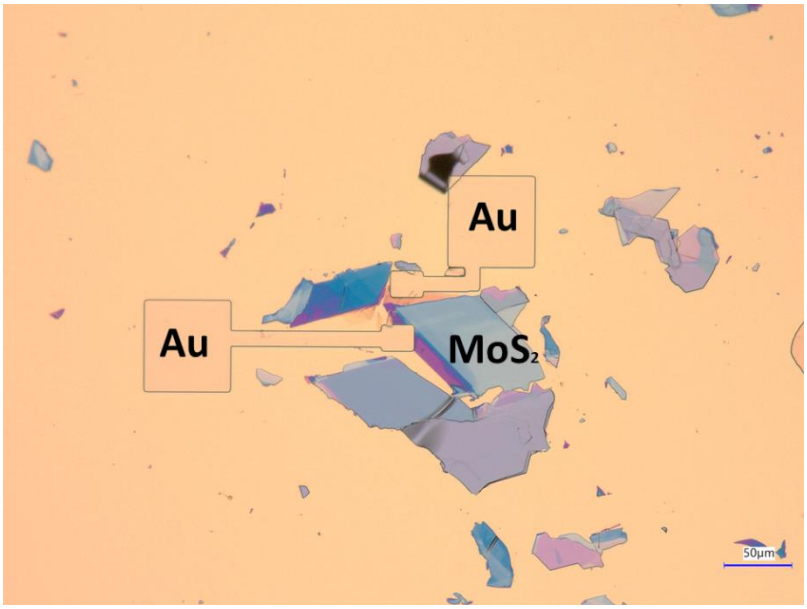

Figure 8.5. An example of fabricated Au contacts to MoS_2 multilayer.

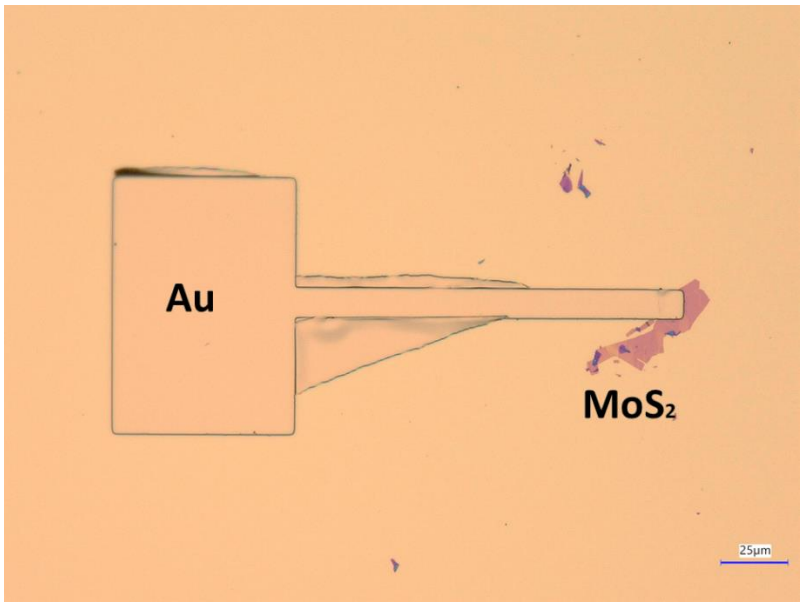

Figure 8.6. An example of fabricated Au contact to MoS_2 few-layer.

The method of preparing metallic contacts presented above was further used to produce the devices based on exfoliated MX and MX_2 flakes. Chapter 9 in detail presents the manufactured devices such as photodetectors on MoS_2 and WS_2 with contact fabrication by using Gas Injection System (GIS) and Focused Ion Beam (FIB).

8.3 An example device with manufactured contacts

Using the contact preparation method described above, the electrical contacts were prepared for a device such as a solar cell. As substrate was used SiO_2 wafer from Microchemical Co. The 100 nm silver (Ag) layer was deposited on SiO_2 by e-beam evaporation technique. Here, the Ag layer allows to increase the efficiency of the fabricated solar cell. Further, Au contact pads were prepared for electrical characterisation of obtained device. The exfoliated MoS_2 flakes were used as absorbing material due to its visible light absorbing properties. The *I-V* characteristics were measured in Dark (without illuminating the cell with incident light) and Light condition (with laser top illumination) (Figure 8.7). For device illumination was used laser diode with 532 nm excitation and power 2 mW.

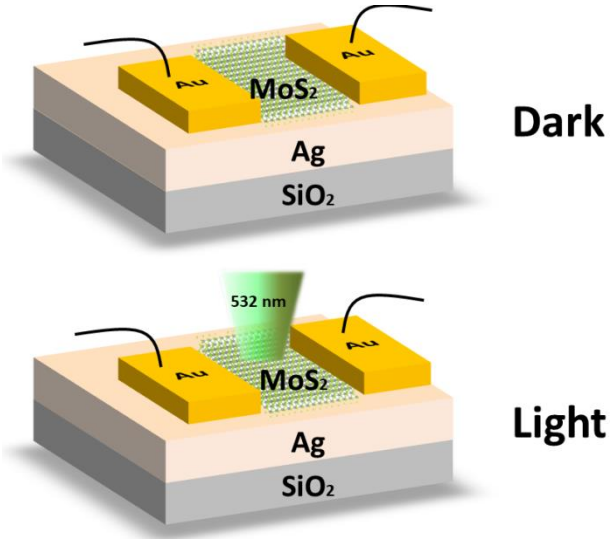

Figure 8.7. Schematic view on MoS_2 solar cell in Light and Dark conditions.

For electrical measurements a few devices with multilayer and few-layer MoS_2 flakes were prepared (Figure 8.8). For MoS_2 multilayer, the measured *I-V* electrical characteristics in Dark condition are almost ohmic whereas after illuminating the cell, an increase in conductivity was observed. In the case of monolayer the characteristics change significantly which may be related to the degradation of the few-layer flake.

From the device measurements we can see that the fabricated contacts by using the presented manufacturing techniques are characterized by the high strength and are suitable for several times electrical measurements. However, contacts prepared in this way (PVD and laser lithography) do not always provide a ohmic characteristics.

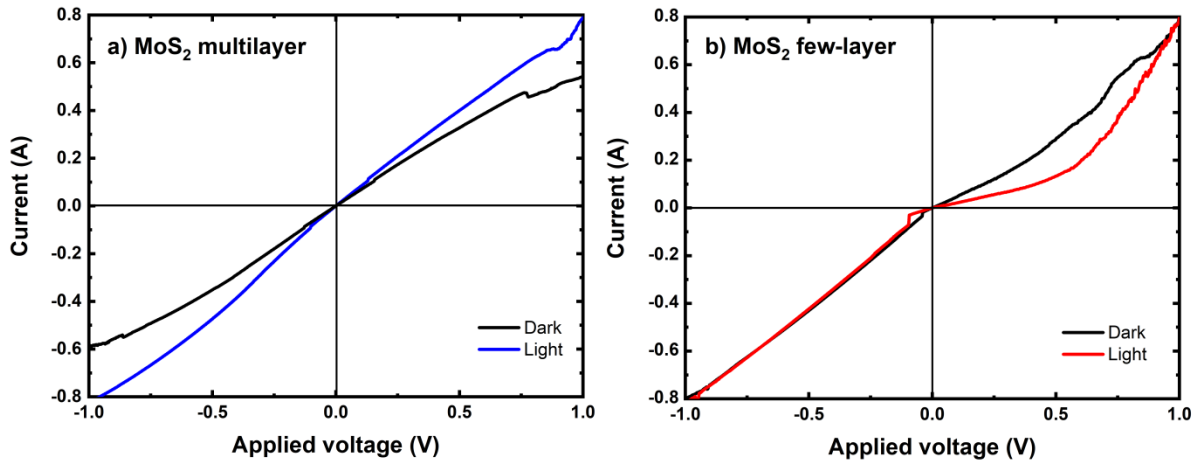

Figure 8.8. The *I-V* characteristic for MoS_2 solar cell on: a) MoS_2 multilayer; b) MoS_2 few-layer.

9 Photodetector on MX_2 layered materials

In this thesis, presented photodetector device is based on absorption of light by MX_2 materials and photoconductive effect. According to photoconductive effect, the two-dimensional material absorbs photons at and above the bandgap of the MX_2 which leads to the excitation of electron-hole pairs. The channel conductance become higher due to photoinduced carriers. In this work, the main parameter of PD as photoresponsivity *(R)* was appointed for each fabricated device. Responsivity is the main parameter for PD, this is a measure of output current per incoming optical power, describes how a detector system responds to illumination. Therefore, the performance of each photodetector was determined according to photoresponsivity.

9.1 Sample preparation

The photodetector fabrication is divided into several steps (Figure 9.1): 1) Preparation of sol-gel SiO_x:TiO_y layers by deep-coating technique; 2) Photolithography process; 3) Dry etching and photoresist removal; 4) Mechanical exfoliation and transfer of MX/MX_2 flakes on top of sol-gel waveguide; 5) Metal contact pads deposition; 6) Electrical and optical measurements.

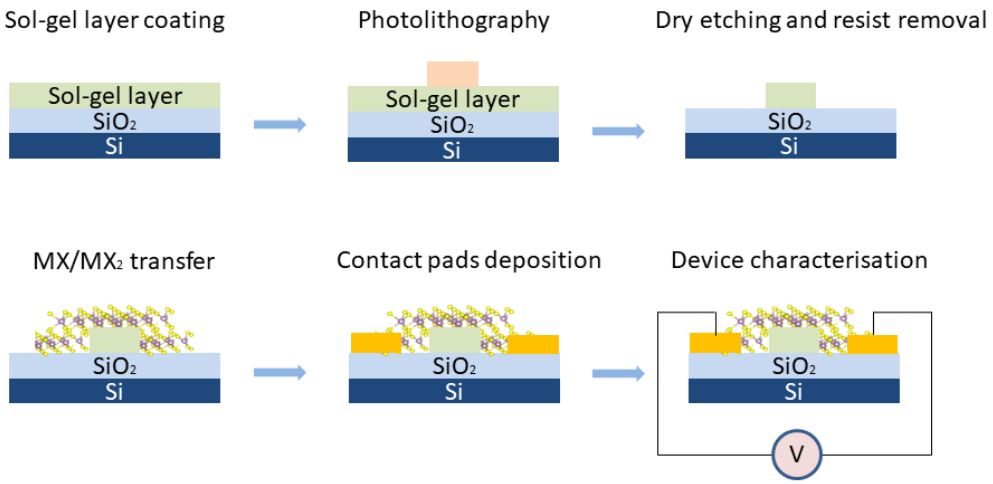

Figure 9.1. Photodetector fabrication process.

9.2 Contact pads preparation

The metal contacts pads for device characterisation were fabricated with a few techniques: metal deposition with Gas Injection System (GIS) and Focused Ion Beam (FIB) in Scanning Electron Microscope Helios 660 and electron-beam physical vapor deposition (PVD). Figure 9.2 shows the examples of deposited platinum (Pt) contacts with GIS and FIB technique. During Pt deposition process the interaction of surface emitted secondary electrons in the irradiated area with locally adsorbed gas molecules delivered by a gas injector system GIS appear. Pt pads were deposited in a single step, which is different from commonly used lithographic multi-stage processes. For this thesis, the standard Pt precursor

was used in Helios dual-beam FIB system. Platinum precursor is the organometallic trimethyl (methylcyclopentadienyl) platinum(IV), $(CH_3)_3$ $Pt(C_pCH_3)$. The all Pt pads depositions were performed on a FEI Helios NanoLabTM Dual-Beam instrument using an acceleration voltage of 30 kV. The distance between pads was varied from 23 to 41 µm, where the Pt pads nominal dimensions are 80 × 80 µm and thickness approx. 0.05 µm.

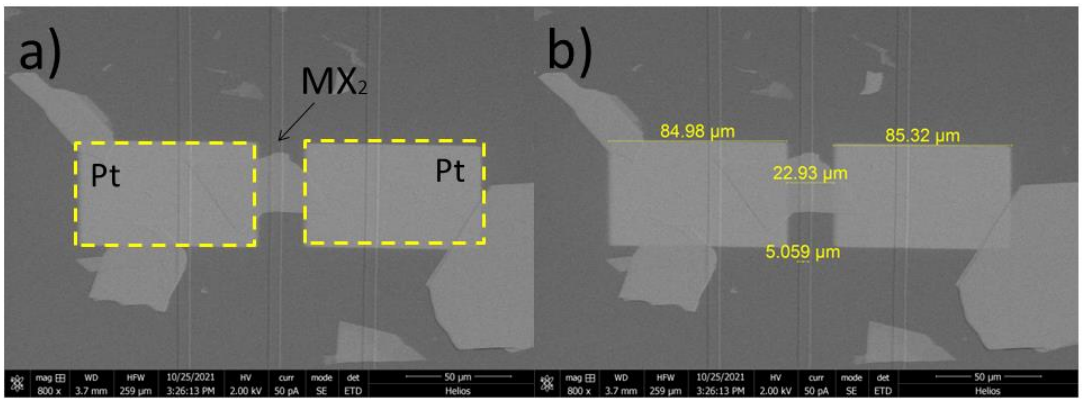

Figure 9.2. a) SEM image of the platinum contacts deposited with GIS and FIB; b) Dimensions of fabricated Pt contacts.

According to the first fabrication technique, which begins from laser lithography followed by PVD, a few samples were produced. Samples with patterned pads by laser lithography were loaded into a PreVAC electron beam evaporator for evaporation of Pt contacts with thickness approx. 0.05 µm. Two approaches were tested for this technology. The first approach is Pt deposition before transfer of MX_2 flake. The second approach is exfoliation and transfer of MX_2 material and later Pt deposition.

The samples with metal pads, received by two techniques, were used for electrical probing, providing better charge conduction and low contact resistance for the device. Examples of fabricated Pt pads are shown on Figures 9.3 - 9.4. The dimensions of each Pt pad size are approx. 150 × 100 µm.

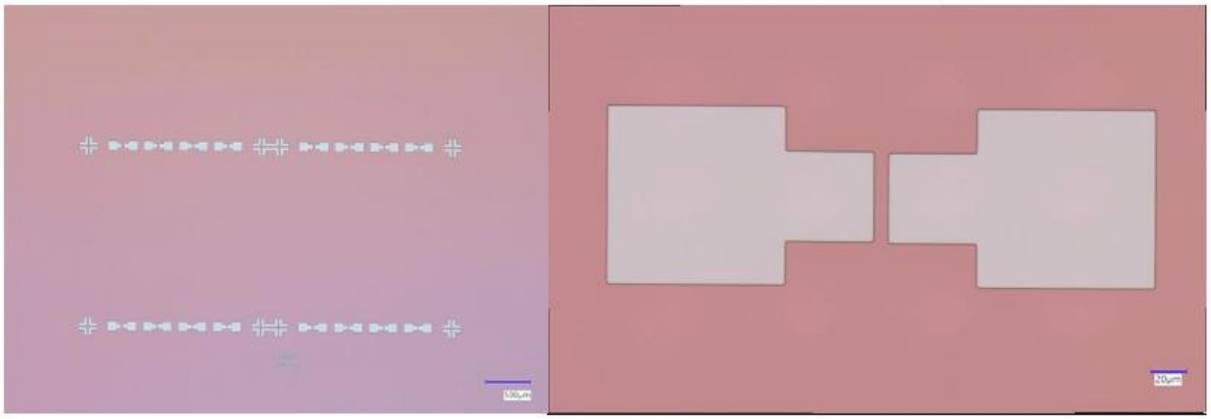

Figure 9.3. Contact pads pattern after photolithography.

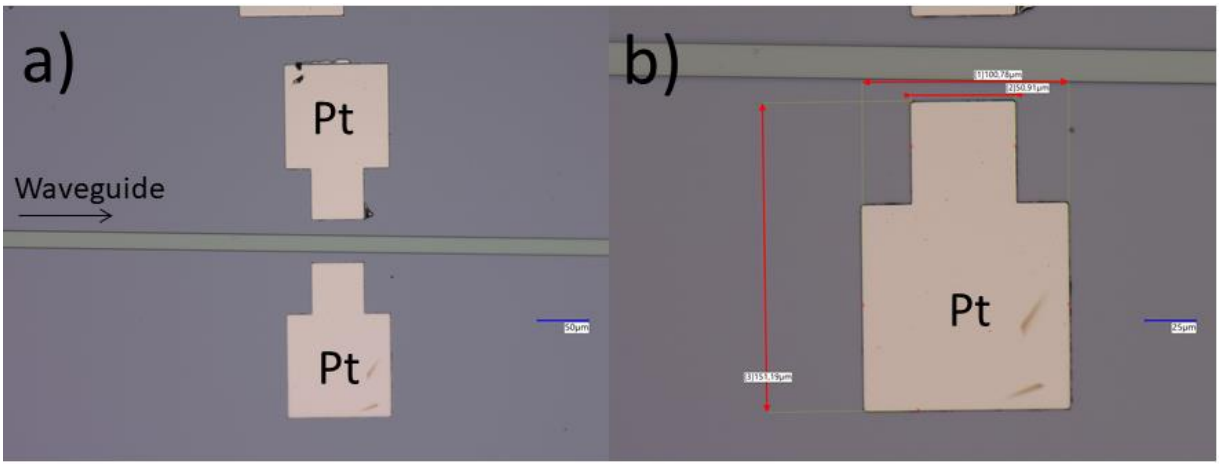

Figure 9.4. Images of deposited Pt contact pads: a) Image from optical microscope; b) Measurements of contact dimensions.

9.3 Experimental setup for device characterisation

For electrical device characterisation a special setup was built (Figure 9.5). Setup consist from: 1) Optical microscope Motic; 2) KEYSIGHT Source Unit for device characterisation; 3) Two electrodes with XYZ control; 4) XYZ stage for sample; 5) Broadband Thorlabs source with fiber for coupling light into waveguide; 6) CCD camera with objective for detection optical mode from waveguide.

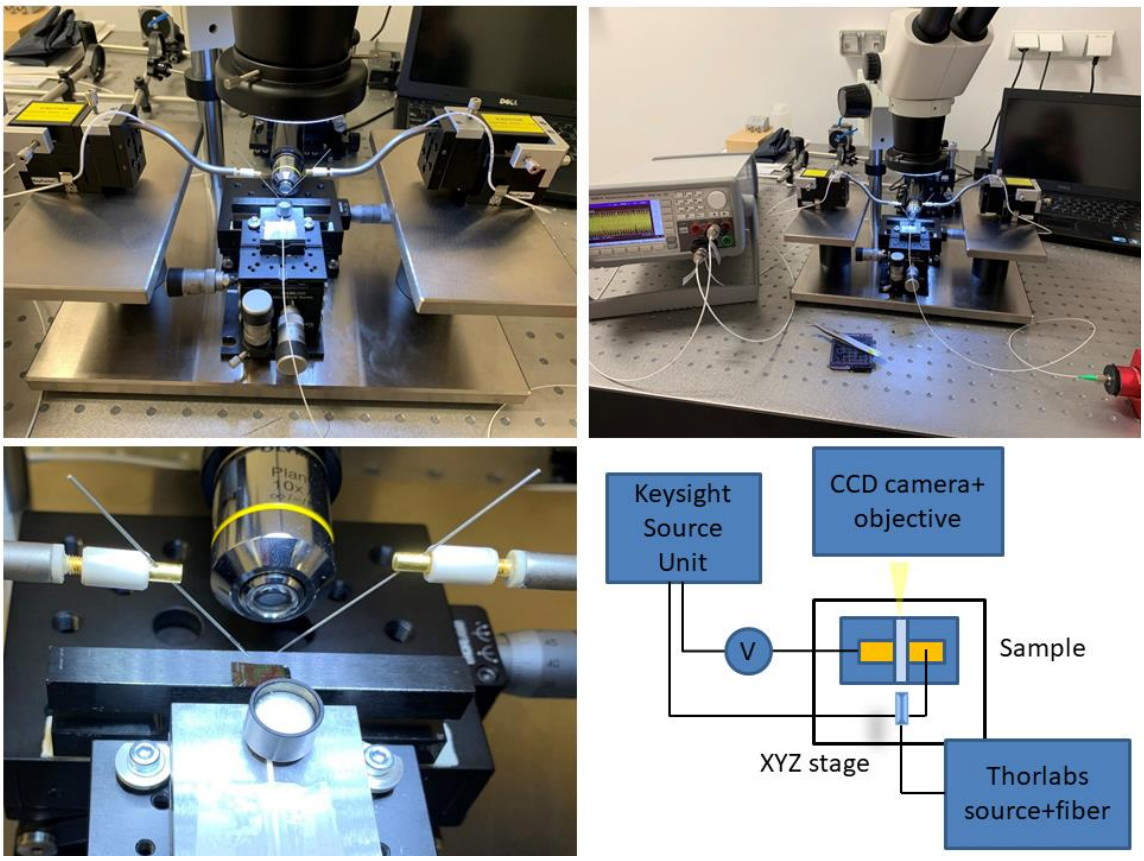

Figure 9.5. Experimental setup for measurement *I-V* characteristics.

For each sample the current-voltage *I-V* characteristic were measured by using a Keysight B2901A precision Sourcemeter and two electrodes. All measurements were conducted under ambient conditions at room temperature.

The measurement was made as follows: 1) The sample with sol-gel waveguides was placed on *XYZ* stage; 2) The ends of two electrodes were placed directly on photodetector contact pads; 3) By using Keysight Source Unit the voltage was applied on two electrodes and *I-V* characteristic in dark condition (without coupling light into the waveguide) was measured; 4) repeating the *I-V* characteristic measurements with the coupling light into the waveguide, optical mode is detected with CCD camera.

9.4 Device on graphene/WS_2

Device with graphene/WS_2 was fabricated on SiO_2/Si substrate. Firstly, WS_2 flakes were exfoliated on substrate and graphene monolayer was transferred directly on top of WS_2. After transfer, metal contacts (Ni/Au) were evaporated. Scheme of device preparation is shown on Figure 9.6.

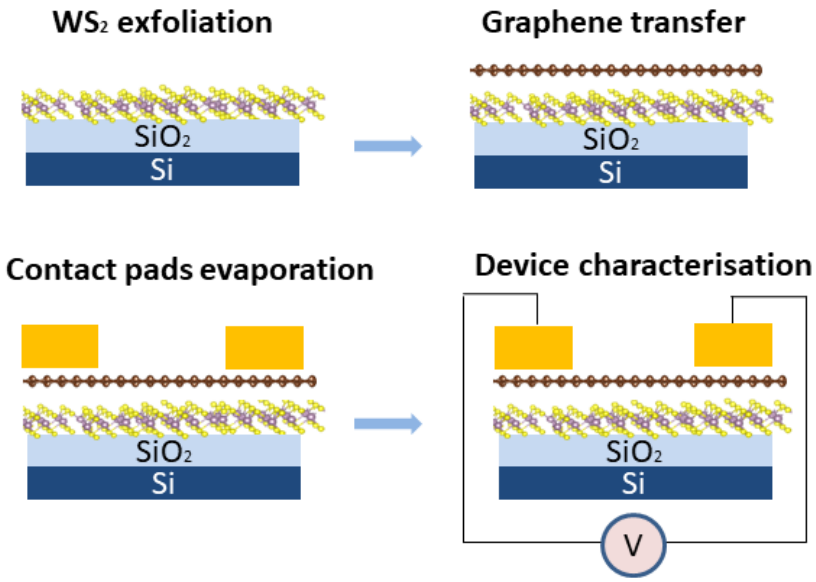

Figure 9.6. The fabrication scheme of device with graphene/WS_2. Scheme represent such steps as WS_2 exfoliation; graphene transfer; contact pads evaporation by PVD technique; device characterization.

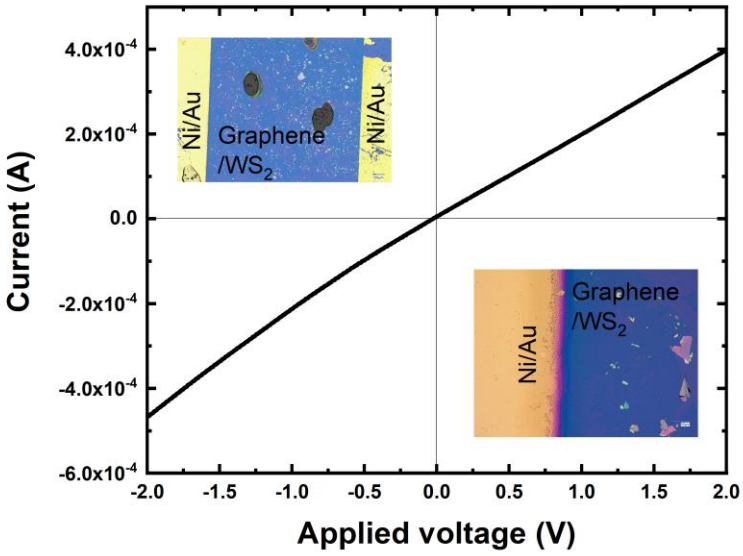

Figure 9.7. The *I-V* characteristic for device with graphene/WS_2.

9.5 Photodetector on WS_2

Photodetector was fabricated on sol-gel SiO_x:TiO_y waveguide (*W* = 5 µm and thickness *H* = 0.280 µm) and exfoliated flake with thickness *d* = 0.08 µm and width *w* = 91.31 µm. The Pt pads were deposited by GIS and Focused Ion Beam (Figure 9.8).

The *I-V* plots were measured for WS_2/waveguide photodetector, see Figure 9.9. From the detected characteristics we clearly see increase of conductivity which caused by light absorption due to WS_2 layer. The photocurrent increases linearly with the bias voltage for all curves, indicating a zero barrier at WS_2-Pt junction. The two methods for light coupling to waveguide were tested. The first one is the light coupling from the face of the waveguide (signed as Light on *I-V*) and the second one – from the top of WS_2/waveguide (signed as Top on *I-V*). By analysing these characteristics we see that the difference of light coupling is relatively small, see Figure 9.9a.

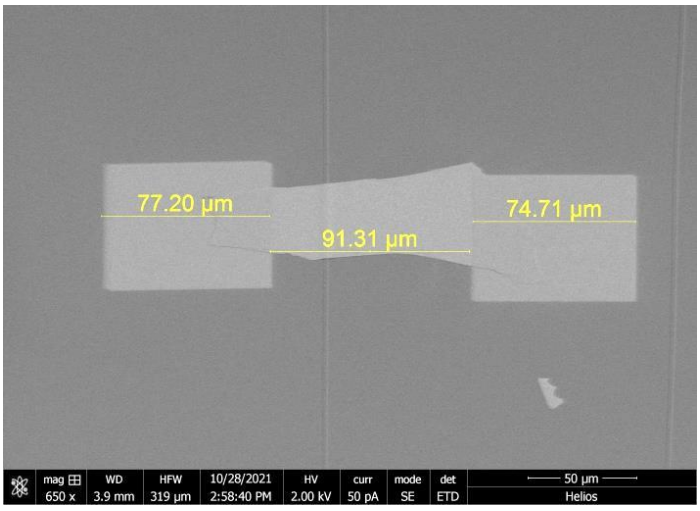

Figure 9.8. SEM image of WS_2 photodetector.

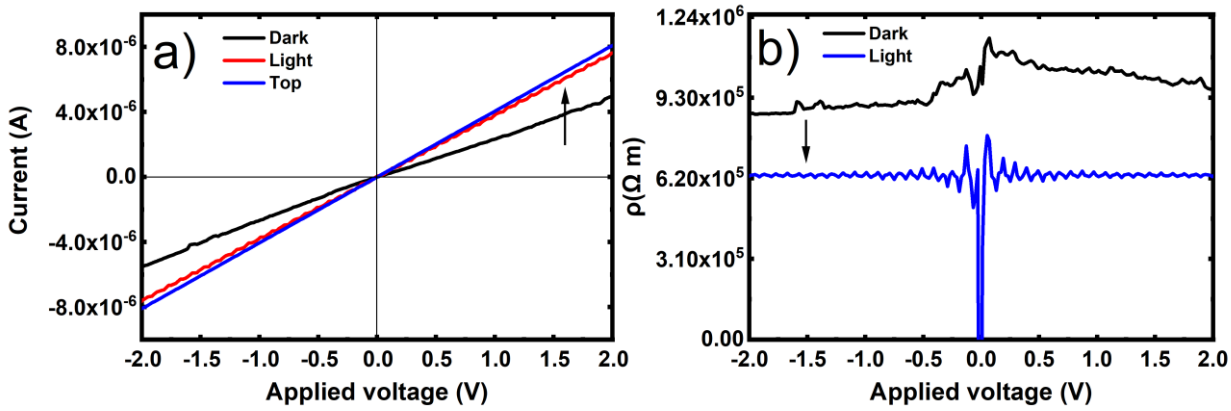

Figure 9.9. Optoelectrical photodetector characterization: a) *I-V* characteristics for WS_2/waveguide (flake thickness *d* = 80 nm); b) Calculated *(ρ-V)* characteristics for n-WS_2/waveguide.

The transmittance spectra for waveguide with/without WS_2 flake were measured in order to check how the transmittance changes after applying the flake on top of waveguide (Figure 9.10). For WG without flake, the transmittance signal is quite strong with maximum at 0.590 µm. Whereas, after transfer WS_2 flake, the signal was dropped, indicating significant light absorption of the WS_2. This result confirm that this material is an ideal candidate for building a photodetector based on MX_2 material. The absorption of WS_2 flake depends from the layer thickness and flake length. To avoid the extrinsic losses in waveguide, Pt contacts were located away from waveguide, where the minimal distance does not exceed 15 µm.

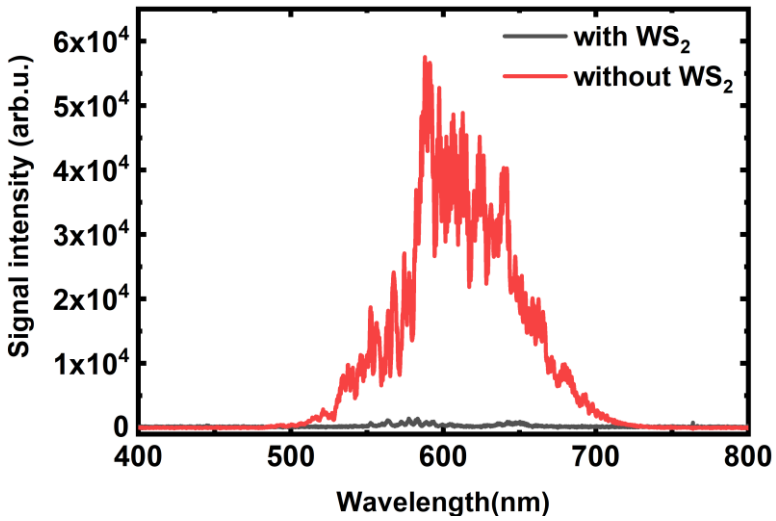

Figure 9.10. Transmittance comparison spectra for waveguide with/without WS_2.

9.6 Electrical properties of fabricated photodetectors

The electrical parameters calculated from *I-V* curves were presented above. The main three parameters were resistance *(R)*, resistivity *(ρ)* and conductivity *(σ)* of our devices. In case photodetectors, the amount of current depends on the magnitude of the applied voltage *(V_{bias})* and material characteristics that the current is flowing through. The material

can resist the flow of the charges. The measure of how much a material resists the flow of charges is known as the electrical resistivity. The greater the resistivity, the larger the field needed to produce a given current density. In PhD thesis, a few materials were measured (MoS_2, $MoSe_2$, WSe_2, WS_2, ReS_2) with the purpose to study their electrical characteristics.

The parameters which affect the resistance *(R)*:

- The material resistivity;
- The total length of the material;
- The cross-sectional area;
- The material temperature.

Electrical conductivity is material characteristic which represents material's ability to conduct current. In ideal, the resistance of material is proportional to its length and inversely proportional to its cross-sectional area. Therefore, the electrical resistivity is does not depend from geometric properties of a material.

In an isotropic three-dimensional (3D) material, the electrical resistance (*R*), electrical resistivity (ρ) and conductivity (σ) are defined as:

- Electrical resistance is *R*:

$$R = \frac{V}{I}, \tag{4}$$

- Electrical resistivity (ρ):

$$R = \rho\frac{L}{A};\ \rho = \frac{RA}{L}, \tag{5}$$

where *R* denotes the calculated resistance; *A* denotes the cross-sectional area of the flake; *L* denotes the flake length between Pt pads.

The cross-sectional area was calculated by formula:

$$A = (Lwd), \tag{6}$$

where *L* denotes the flake length between Pt pads; *w* denotes flake width; *d* denotes the flake thickness.

- Electrical conductivity (σ):

$$\sigma = \frac{1}{\rho}, \tag{7}$$

where ρ denotes the electrical resistivity (Ωm).

For study how type of material and flake dimensions affects the electrical characteristic of devices on MoS_2, $MoSe_2$, WS_2, WSe_2, ReS_2 flakes, the electrical resistance, electrical resistivity and electrical conductivity were calculated and presented in Table 13.

The calculated resistance for MX_2 based devices varies from 0.34 to 450 kΩ depending from material. Therefore, the device-to-device resistance variation could be related with the local inhomogeneity of MX_2 film. The highest resistance received for device with ReS_2 flake, which is 410 kΩ, due to the longest length *L* of flake between pads (189 μm). Against, the lowest resistance is obtained for the device with MoS_2 flake, which is 0.36 kΩ and flake length of 15 μm. These obtained results confirm the theory regarding the influence of flake length between pads on the resistance value and can be used for the construction of devices based on MX_2 materials with desired characteristics. The flake length of 15 μm is minimal length which can be used for photodetector fabrication due to appearing of negative effects from close Pt pads to the mode distribution in the waveguide. The maximum length of flake is arbitrary but too high resistance values must be taken into account.

The calculated values of electrical conductivity show that its value depends on the thickness of the material, where the conductivity increase with a thickness decrease. The lowest resistivity and highest conductivity was received for device with MoS_2 with flake length of 15 μm and thickness 0.045 μm (Table 13):

- Electrical resistivity $\rho = 9.00 \cdot 10^{-10}$ Ωm.
- Electrical conductivity $\sigma = 1.11 \cdot 10^{9}$ S/m.

The bulk platinum has the conductivity of $0.94 \cdot 10^{7}$ S/m and resistivity $10.60 \cdot 10^{-8}$ Ωm. These values are quite close to obtained for MoS_2 devices with Pt pads; results indicates the height quality of fabricated Pt metal contacts. As summary, the higher conductivity is obtained for thinner flakes MoS_2 (0.045 μm), $MoSe_2$ (0.025 μm), WSe_2 (0.015 μm). This result is consistent with Ref.[186]

Table 13. The electrical resistance, resistivity and conductivity for devices on exfoliated MX_2 flakes, calculated from *I-V* characteristics (V_{bias} = 0 V).

	MoS_2	**$MoSe_2$**	**WSe_2**	**WS_2**	**ReS_2**
	L=15 μm; *d*=0.045 μm	*L*=40 μm; *d*=0.025 μm	*L*=72 μm; *d*=0.015 μm	*L*=91μm; *d*=0.08 μm	*L*=189 μm; *d*=0.130 μm
R(kΩ)	0.364	0.401	0.392	409.4	410.6
ρ(Ωm)	$9.00 \cdot 10^{-10}$	$2.00 \cdot 10^{-10}$	$3.90 \cdot 10^{-10}$	$8.78 \cdot 10^{-7}$	$3.53 \cdot 10^{-4}$
σ(S/m)	$1.11 \cdot 10^{9}$	$3.16 \cdot 10^{9}$	$2.56 \cdot 10^{9}$	$1.13 \cdot 10^{6}$	$2.8 \cdot 10^{3}$

9.6.1 Electrical properties study of annealed photodetectors

The advanced electronic technology requires channel materials and ultralow-resistance contacts to be find out. For examination the contacts quality (stability in ambient conditions, resistance to high temperatures), a few fabricated devices were annealed in N_2 gas. The *I-V* characteristics were remeasured after heating at 373, 523 and 673 K. Annealing was achieved by rapid thermal annealing at these temperatures for 5 min in N_2 gas.

Figure 9.11-9.13 shows the *I-V* characteristics for devices before annealing (at 293 K) and after annealing (at 373, 523, 673 K). Before annealing, the *I-V* plot show perfect ohmic behaviour with a resistance 21∼26 kΩ at 2 V. After annealing, the resistance increased to 54-157 kΩ. Such an increase can be related with sintering together the Pt particles and increase in the impurities content.

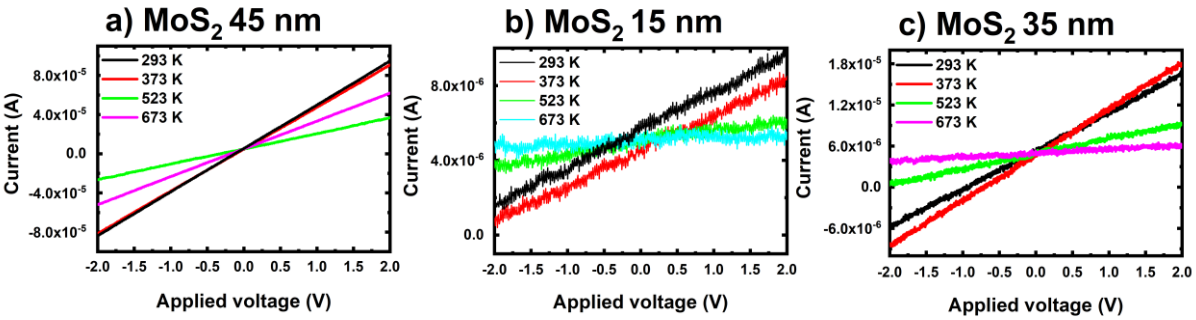

Figure 9.11. The *I-V* characteristics for annealed devices on MoS_2.

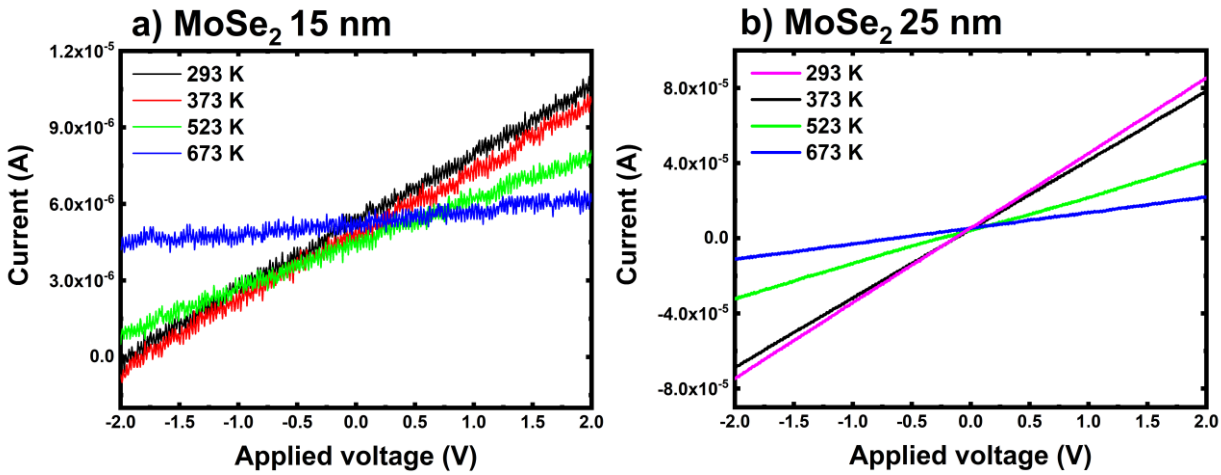

Figure 9.12. The *I-V* characteristics for annealed devices on $MoSe_2$.

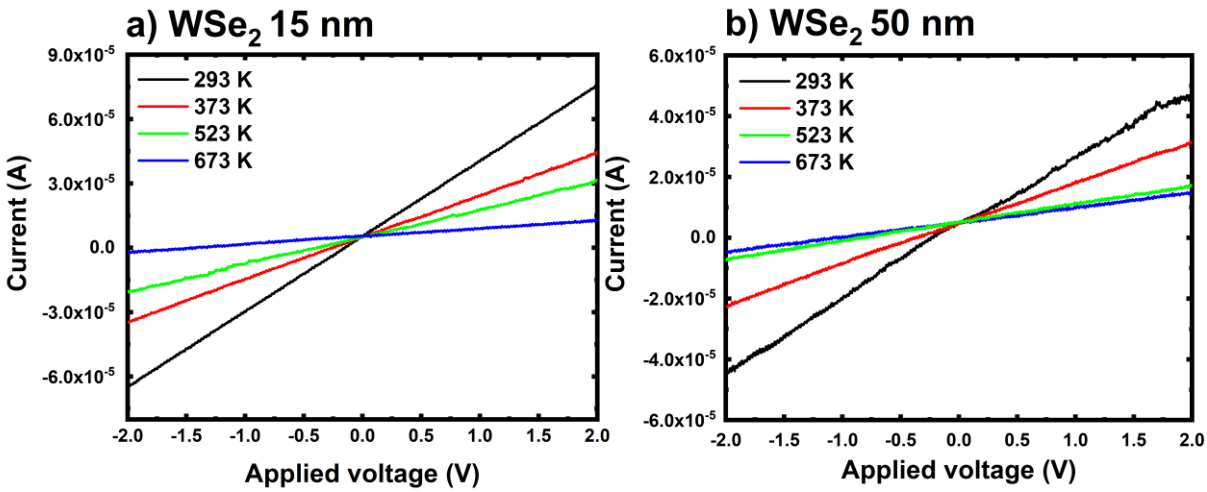

Figure 9.13. The *I-V* characteristics for annealed devices on WSe_2.

Based on obtained experimental measurements, the electrical resistance was calculated for MoS_2, $MoSe_2$ and WSe_2 at 293, 373, 523, 673 K. At 273 K the resistance values from 21 to 26 kΩ. After heating to 673K a significant increase of resistivity was noticed, which is the expected effect as resistance is temperature dependent. The highest value is reached 157 kΩ for device on WSe_2 material (Figure 9.17c). As platinum is conductor, therefore resistance increases with increasing temperature. This behaviour is visible in our experiment.

Before annealing, resistivity of MoS_2, $MoSe_2$, WSe_2 based devices is varied from 2 to 9 $\cdot 10^{-10}$ Ωm at 0 V. After annealing, the value of resistivity at 0 V is: a) for MoS_2 increased from $8.97 \cdot 10^{-10}$ to $1.03 \cdot 10^{-9}$ Ωm; b) for $MoSe_2$ increased from $3.16 \cdot 10^{-10}$ to $4.29 \cdot 10^{-9}$ Ωm; c) for WSe_2 increased from $3.9 \cdot 10^{-10}$ to $3.62 \cdot 10^{-10}$ Ωm. Due to a slight increase in resistivity, the obtained results indicate quite high quality of fabricated devices. After annealing up to 673 K the resistivity is decreased due to heating of ability the organic compounds in Pt pads. Therefore, resistivity is the highest for annealed samples at 673 K.

9.7 Wavelength selective coupling in photodetector

A few devices on WSe_2 exfoliated flakes were measured and characterised according to selective wavelength coupling (Figure 9.14). The excitation were achieved with broadband source and transmission BrightLine single-band bandpass filters: *FF01-520/35-25* with transmission band *502.5 – 537.5 nm* and the second filter *FF01-605/15-25* with transmission band *597.5 – 612.5 nm*.

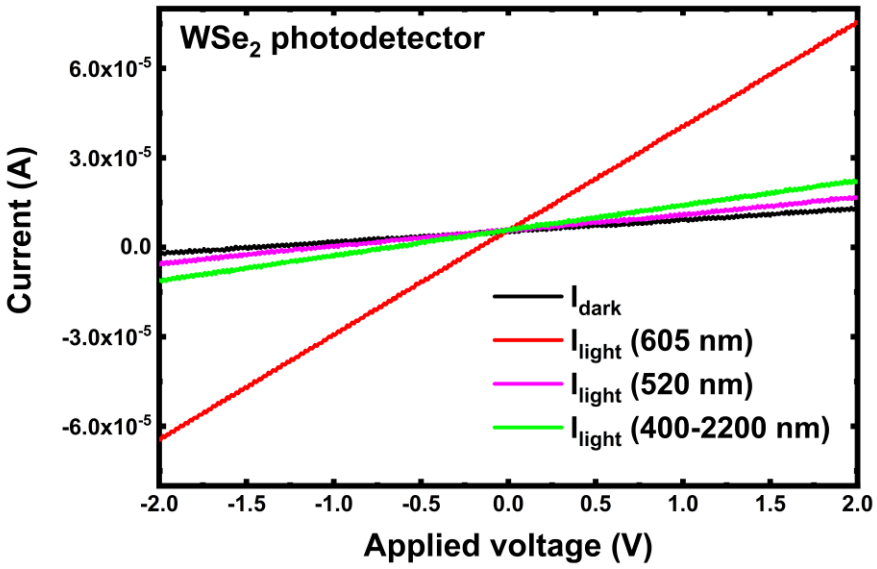

Figure 9.14. The *I-V* characteristics for WSe_2 photodetector. Comparison of wavelength-dependent coupling with broadband source (400-2200 nm), single wavelength 520 and 605 nm.

Comparison of conductivity on *I-V* characteristics shows its significant increase after waveguide excitation by wavelength with 605 nm. Such increase due to the fact that the waveguide transmits more light at 580-620 nm and more light at this wavelength is absorbed by the material. Therefore, efficiency of photodetectors is higher by 605 nm excitation compared to broadband source or 520 nm (Figure 9.15b). Moreover, this result could be related with lower excitation power is we use broadband wavelength (400-2200 nm) and higher power at single wavelength after applying filter.

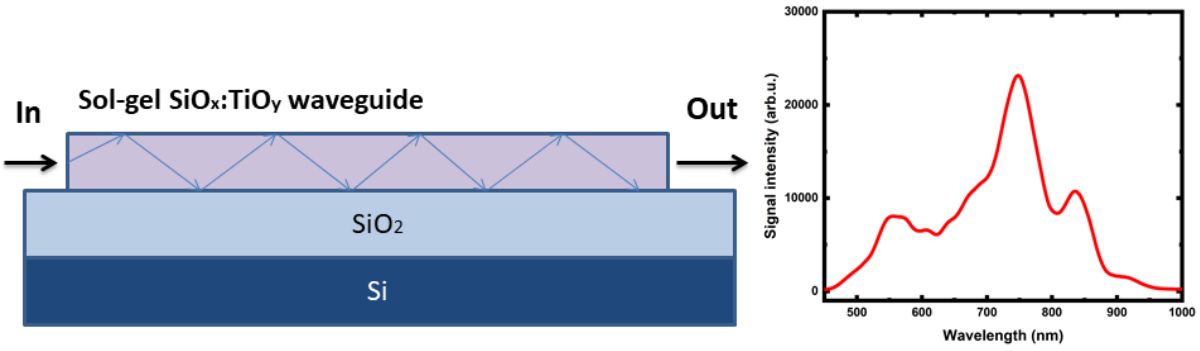

Figure 9.15. Sol-gel photonic waveguide and reference spectra. Waveguides provide confinement through total internal reflection. This can be visualized by the arrows representing the ray tracing of a beam propagating along the waveguide.

9.8 Photodetector photoresponsivity

1) Photocurrent (I_{ph}). The photocurrent is defined with formula:

$$I_{ph} = I_{light} - I_{dark}, \tag{8}$$

2) Photoresponsivity (R). Photoresponsivity is the ratio of the photocurrent (I_{ph}) to the incident power density (P_{in}), in units AW^{-1}:

$$R = \frac{I_{ph}}{P_{in}A}, \tag{9}$$

where I_{ph} denotes the photocurrent; P_{in} denotes the incident power density (AW^{-1}), A denotes the effective absorption flake area. Photoresponsivity describes the ability of photoelectric conversion in photodetectors.

Table 14 presents the calculated values of photoresponsivity for our fabricated devices. These values are ranges from $4.75 \cdot 10^{-3}$ A/W for p-MoS_2 and 62.2 A/W for WSe_2. Therefore, the highest value is affected by larger absorbance of WSe_2 material and covering this wavelength with propagation wavelength of waveguide. Our fabricated waveguides for fabrication photodetectors are propagate at wavelength 500-700 nm. Absorbance spectra of our MX_2 materials cover visible spectra.

Table 14. Summary of calculated photodetector parameters at V_{bias} = 2 V.

Material	**Excitation wavelength (nm)**	**Excitation laser power(W)**	**Photoresponsivity (A/W)**
n-MoS_2 (60 nm)	400-2200	$1 \cdot 10^{-6}$	$2.54 \cdot 10^{-2}$
n-MoS_2 (150 nm)	400-2200	$1 \cdot 10^{-6}$	3.03
p-MoS_2 (200 nm)	400-2200	$1 \cdot 10^{-6}$	$4.75 \cdot 10^{-3}$
p-MoS_2 (60 nm)	400-2200	$1 \cdot 10^{-6}$	$2.42 \cdot 10^{-4}$
p-MoS_2 (500 nm)	400-2200	$1 \cdot 10^{-6}$	$7.53 \cdot 10^{-3}$
WSe_2 (130 nm)	400-2200	$1 \cdot 10^{-6}$	9.2
WSe_2 (130 nm)	605	$1 \cdot 10^{-6}$	62.2
WSe_2 (130 nm)	520	$1 \cdot 10^{-6}$	1.5
WS_2 (80 nm)	400-2200	$1 \cdot 10^{-6}$	2.67

Based on measured *I-V* characteristics, the photoresponsivity dependence from the waveguide excitation power is shown on Figure 9.16. The highest whereas value (60 A/W) is received for device excitation at wavelength 605 nm.

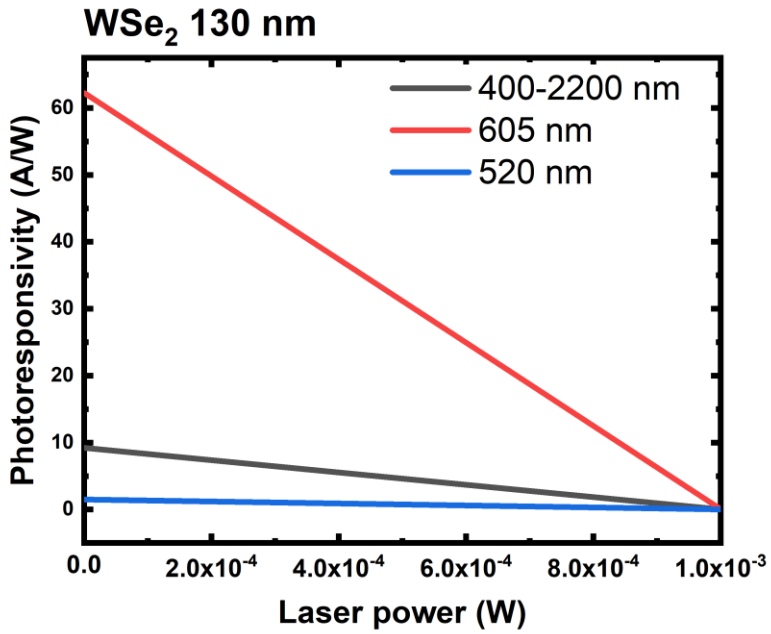

Figure 9.16. Dependence of photoresponsivity from the waveguide excitation power at broadband wavelength (400-2200 nm), single wavelength (605 and 520 nm). Values calculated for V_{bias} = 2 V.

9.9 Stability of devices under ambient conditions

To verify the stability of devices under laboratory conditions, a few samples with photodetectors were remeasured after one year at ambient conditions. Figure 9.17 represent results from these measurements for $MoSe_2$ and WSe_2 based devices.

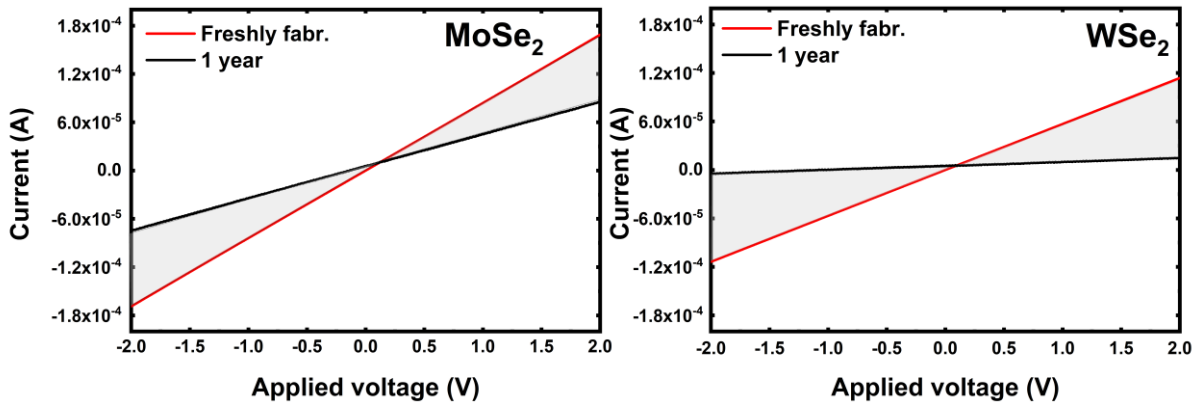

Figure 9.17. The *I-V* characteristics comparison at I_{dark} for $MoSe_2$ and WSe_2 based devices. Characteristics were measured for freshly fabricated devices and after a year.

The comparison of the measured characteristics indicates a decrease in the conductivity of the devices, which may result in increased resistance and gradual degradation of the material or Pt contacts. Additionally, protective layer can be used as a solution to keep the initial values of conductivity. Whereas our sample still behave linear ohmic characteristic, which show the high stability of our device even without protective layer. Therefore, as a solution to maintain device characteristics, the thin polymer film or thin Al_2O_3 can prevent the electrical property degradation.

Summary and future work

The presented PhD work based on fabrication of photonic microstructures like waveguides and microdiscs from the novel material as sol-gel SiO_x:TiO_y and their integration with the two-dimensional materials like monochalcogenides (MX) and dichalcogenides (MX_2). The research conducted as part of this PhD work aimed to prove the theses described at the beginning of this PhD work:

1) Fabrication of photonic microstructures (waveguides, microdiscs, ring resonators) from the new material platform as sol-gel SiO_x:TiO_y with low roughness and appropriate optical properties, which confirmed by experimental tests. These fabricated microstructures were further used as a basis for semiconductor devices.
2) The integration of two-dimensional layered materials like MX and MX_2 materials with a sol-gel SiO_x:TiO_y platform allows the study of new optical properties of these two-dimensional materials. The integration was performed using a specially created system for transfer the two-dimensional materials to various types of structures. Additionally, various types of heterostructures (for instance with graphene), made of two-dimensional materials were created on the sol-gel surface.
3) The photodetector device, which was created on the basis of a planar sol-gel waveguide and thin exfoliated flakes, in work presented. To characterize the photodetector, a special electrical measurement setup was built.

In presented work the application of novel sol-gel SiO_x:TiO_y material was presented. From two-compound SiO_x:TiO_y material the photonic waveguides and microdiscs on visible wavelength were fabricated. The obtained microstructures are characterised by high refractive index ($n \approx 1.80$ at wavelength 632.8 nm) and low roughness (of the order of several nanometers), which are important for optical applications. The waveguide transmittance measurements were performed to confirm the low propagation losses.

The mechanical exfoliation was applied for integration the exfoliated two-dimensional materials with previously fabricated photonic waveguides. By using a special transfer setup, monochalcogenides (MX) and dichalcogenides (MX_2) layered materials are successively integrated with the created structures. Additionally, a special setup was created for carrying out the graphene transfer on a target substrate. In work, transferred graphene layer was used as a transparent electrode and further implemented in one of the presented devices.

This work provides results on Raman and photoluminescence spectroscopy of two-dimensional materials and their heterostructures. A comprehensive study of stability the mechanically exfoliated layered MX and MX_2 materials under ambient conditions in work presented. Additionally, the encapsulation possibilities of highly reactive $HfSe_2$ and ReS_2 layered materials by sol-gel SiO_x:TiO_y was demonstrated.

Subsequent stages of PhD work consisted of research on the preparation of the integrated devices on SiO_x:TiO_y waveguide. First, the issue of preparing the electrical contacts for bulk and exfoliated two-dimensional materials was examined and presented.

The work presents and demonstrate the use of GIS and FIB for fabrication metallic electrical contacts for microdevices. The most important advantage of this technology is repeatability, thanks to which it is possible to always obtain ohmic contacts, hard to obtain using other methods and technologies. For presented photodetectors the electrical properties were measured and calculated.

Finally, the future work on this topic will include the research on fabrication of photonic devices on another two-dimension materials and also their heterostructures like MX_2/h-BN/MX_2. Moreover, the impact of encapsulation by atomic layer deposition Al_2O_3 layer on the electrical properties of finished device will be explored.

Publications and Conferences

Publications related to the topic of the PhD thesis

P1. **Hlushchenko, D**., Siudzinska, A., Cybinska, J. et al. Stability of mechanically exfoliated layered monochalcogenides under ambient conditions. *Sci. Rep.* **2023**, *13*, 19114. https://doi.org/10.1038/s41598-023-46092-1

Impact factor: 4.997

Daria Hlushchenko contribution:

- My participation consisted in writing the article and preparing all tested samples using mechanical exfoliation; performing measurements of Raman and photoluminescence spectra; analysis of the collected spectra; observation of material degradation using an optical microscope and a scanning electron microscope (SEM images).

P2. Butt, M.A.; Tyszkiewicz, C.; Karasiński, P.; Zięba, M.; **Hlushchenko, D.;** Baraniecki, T.; Kaźmierczak, A.; Piramidowicz, R.; Guzik, M.; Bachmatiuk, A. Development of a low-cost silica-titania optical platform for integrated photonics applications. *Optics Express.* **2022**, *30(13)*, 23678-23694.

https://doi.org/10.1364/OE.460318

Impact factor: 3.833

Daria Hlushchenko contribution:

- My participation consisted in preparing samples with SiO_x:TiO_y planar waveguides (cleaning the substrate, preparing the substrate for photolithography); performing optical photolithography to obtain a photoresist pattern; participation in plasma etching (development of etching parameters); characterization of waveguides after plasma etching using SEM (Fig. 10 and 12); writing point 3 in the publication. Additionally, realization of cross-sections by using Focused Ion-Beam (FIB).

P3. Kim, J.Y.; Gelczuk, L.; Polak, M.P.; **Hlushchenko, D.;** Morgan, D.; Kudrawiec, R.; Szlufarska, I. Experimental and theoretical studies of native deep-level defects in transition metal dichalcogenides. *npj 2D Materials and Applications*. **2022**, *6(75)*, 1-11. DOI: 10.1038/s41699-022-00350-4

Impact factor: 10.516

Daria Hlushchenko contribution:

- Fabrication of electrical contacts for DLTS measurements: substrate and sample preparation; metal deposition of Ohmic and Schottky contacts; sample heating in inert atmosphere; preparing a description of the sample preparation for the article.

Other publications

P4. Melnychenko, A.M.; Zelewski, S.J.; **Hlushchenko, D.;** Lis, K.; Bachmatiuk, A.; Kudrawiec, R. Electro-modulation and surface photovoltage spectroscopy with semi-transparent graphene electrodes. *Applied Surface Science.* **2023**, vol. 613, art. 156020, s. 1-9. https://doi.org/10.1016/j.apsusc.2022.156020

Impact factor: 7.392

Daria Hlushchenko contribution:

- Preparation of semi-transparent graphene electrode: sample cleaning; graphene electrochemical delamination from Cu foil and transfer to the sample; performing graphene layer characterisation (SEM images), measuring Raman spectra for graphene samples.

P5. Ciechanowicz, P., Gorantla, S., Michałowski, P. P., Zdanowicz, E., Rousset, J.-G., **Hlushchenko, D.**, Adamczyk, K., Majchrzak, D., Kudrawiec, R., Hommel, D., Arsenic-Induced Growth of Dodecagonal GaN Microrods with Stable a-Plane Walls. *Adv. Optical Mater.* **2021**, *9*, 2001348. https://doi.org/10.1002/adom.202001348

Impact factor: 10.050

Daria Hlushchenko contribution:

- Performing GaN material surface characterisation: SEM images of surface, defects; cross-sections by using Focused Ion-Beam (FIB).

Conferences

1) Prequel Symposium on Advanced Technologies and Materials, Wrocław, Polska 13.10.2020-15.10.2020.

2) Phobia Annual nanophotonics International Conference 2020, Wrocław, Polska 12.10.2020-14.10.2020.

3) National Electronics Conference 2021, Darlowo, Poland, 5.09.2021-9.09.2021.

References

(1) Zhou, Z.; Yap, Y.K. Two-Dimensional Electronics and Optoelectronics: Present and Future. *Electronics* **2017**, *6(3*), 53.

(2) Wang, T.; Xu, Y.Q. Photonic Structure-Integrated Two-Dimensional Material Optoelectronics. *Electronics* **2016**, *5(4)*, 93.

(3) Ye, M.; Zhang, D.; Yap, Y.K. Recent Advances in Electronic and Optoelectronic Devices Based on Two-Dimensional Transition Metal Dichalcogenides. *Electronics* **2017**, *6(2)*, 43.

(4) Huo, Z.; Wei, Y.; Wang, Y.; Wang, Z.L.; Sun, Q. Integrated Self-Powered Sensors Based on 2D Material Devices. *Adv. Funct. Mater.* **2022**, *32*, 2206900.

(5) Pirri, C.F.; Cocuzza, M. Editorial for the Special Issue on 2D Nanomaterials Processing and Integration in Miniaturized Devices. *Micromachines* **2021**, *12*, 254.

(6) Yang, Y.; Pan, R.; Tian, S.; Gu, C.; Li, J. Plasmonic Hybrids of MoS_2 and 10-nm Nanogap Arrays for Photoluminescence Enhancement. *Micromachines* **2020**, *11*, 1109.

(7) Verna, A.; Marasso, S.L.; Rivolo, P.; Parmeggiani, M.; Laurenti, M.; Cocuzza, M. Lift-Off Assisted Patterning of Few Layers Graphene. *Micromachines* **2019**, *10*, 426.

(8) Pak, S.; Sohn, J.-I. 2D Nanostructures for Optoelectronic and Green Energy Devices. *Nanomaterials* **2023**, *13*, 1070.

(9) Jang, A.-R. Tuning Schottky Barrier of Single-Layer MoS_2 Field-Effect Transistors with Graphene Electrodes. *Nanomaterials* **2022**, *12*, 3038.

(10) Shin, K.H.; Seo, M.-K.; Pak, S.; Jang, A.-R.; Sohn, J.I. Observation of Strong Interlayer Couplings in WS_2/MoS_2 Heterostructures via Low-Frequency Raman Spectroscopy. *Nanomaterials* **2022**, *12*, 1393.

(11) Singh, K.J.; Ciou, H.-H.; Chang, Y.-H.; Lin, Y.-S.; Lin, H.-T.; Tsai, P.-C.; Lin, S.-Y.; Shih, M.-H.; Kuo, H.-C. Optical Mode Tuning of Monolayer Tungsten Diselenide (WSe_2) by Integrating with One-Dimensional Photonic Crystal through Exciton–Photon Coupling. *Nanomaterials* **2022**, *12*, 425.

(12) Zheng, S.H.; Shi, X.Y.; Das, P.; Wu, Z.-S.; Bao, X.H. The Road Towards Planar Microbatteries and Micro-Supercapacitors: From 2D to 3D Device Geometries. *Adv. Mater.* **2019**, *31*, 1900583.

(13) Mak, K.F.; Shan, J. Photonics and optoelectronics of 2D semiconductor transition metal dichalcogenides. *Nature Photonics* **2016**, *10*, 216–226.

(14) Cho, B.; Kim, Y. Preparation and Properties of 2D Materials. *Nanomaterials* **2020**, *10*, 764.

(15) Zhang, X.; Zhang, R.; Zheng, X.; Zhang, Y.; Zhang, X.; Deng, C.; Qin, S.; Yang, H. Interlayer Difference of Bilayer-Stacked MoS_2 Structure: Probing by Photoluminescence and Raman Spectroscopy. *Nanomaterials* **2019**, *9*, 796.

(16) Fu, Y.; Sun, J.; Du, Z.; Guo, W.; Yan, C.; Xiong, F.; Wang, L.; Dong, Y.; Xu, C.; Deng, J.; Guo, T.; Yan, Q. Monolithic Integrated Device of GaN Micro-LED with Graphene Transparent Electrode and Graphene Active-Matrix Driving Transistor. *Materials* **2019**, *12*, 428.

(17) Xiong, F.; Guo, W.; Feng, S.; Li, X.; Du, Z.; Wang, L.; Deng, J.; Sun, J. Transfer-Free Graphene-Like Thin Films on GaN LED Epiwafers Grown by PECVD Using an Ultrathin Pt Catalyst for Transparent Electrode Applications. *Materials* **2019**, *12*, 3533.

(18) Zhang, Y.; Liu, H.; Tan, L.; Zhang, Y.; Jeppson, K.; Wei, B.; Liu, J. Properties of Undoped Few-Layer Graphene-Based Transparent Heaters. *Materials* **2020**, *13*, 104.

(19) Dragoman, M.; Dragoman, D. 2D Nanoelectronics Physics and Devices of Atomically Thin Materials. *Springer, Nanoscience and Technology* **2017**. DOI 10.1007/978-3-319-48437-2.

(20) Ng, L.W.T.; Hu, C.; Howe, R.C.T.; Zhu, X.; Yang, Z.; Jones, C.G.; Hasan, T. Printing of Graphene and Related 2D Materials Technology, Formulation and Applications. *Springer*, **2019**, 19-101.

(21) Yin, L.; Cheng, R.; Wen, Y.; Liu, C.; He, J. Emerging 2D Memory Devices for In-Memory Computing. *Adv. Mater.* **2021**, *33*, 2007081.

(22) Joy, R.; Balakrishnan, N.T.M.; Das, A.; Shafeek, S.; Thakur, V.K.; Zaghib, K.; Jaffarali, J.F.M.; Reddy, M.V.V.; Raghavan, P. Graphene: Chemistry and Applications for Lithium-Ion Batteries. *Electrochem* **2022**, *3*, 143–183.

(23) Pezone, R.; Baglioni, G.; Sarro, P.M.; Steeneken, P.G.; Vollebregt, S. Sensitive Transfer-Free Wafer-Scale Graphene Microphones. *ACS Appl. Mater. Interfaces* **2022**, *14*, 21705−21712.

(24) Cesano, F.; Scarano, D. Graphene and Other 2D Layered Hybrid Nanomaterial-Based Films: Synthesis, Properties, and Applications. *Coatings* **2018**, *8*, 419.

(25) Gong, F.; Li, H.; Wang, W.; Xia, D.; Liu, Q.; Papavassiliou, D.V.; Xu, Z. Recent Advances in Graphene-Based Free-Standing Films for Thermal Management: Synthesis, Properties, and Applications. *Coatings* **2018**, *8*, 63.

(26) Shi, W.; Ma, X. Photovoltaic Effect in Graphene/MoS_2/Si Van der Waals Heterostructures. *Coating*s **2018**, *8*, 2.

(27) Hu, Z.; Ding, Y.; Hu, X.; Zhou, W.; Yu, X.; Zhang, S. Recent progress in 2D group IV–IV monochalcogenides: synthesis, properties and applications. *Nanotechnology* **2019**, *30*, 252001 (26pp).

(28) Sarkar, A.S.; Stratakis, E. Recent Advances in 2D Metal Monochalcogenides. *Adv. Sci.* **2020**, *7*, 2001655.

(29) Gomes, L.C.; Carvalho, A. Electronic and optical properties of low dimensional group-IV monochalcogenides. *J. Appl. Phys.* **2020**, *128*, 121101.

(30) Cheng, K.; Guo, Y.;Han, N.; Su, Y.; Zhang, J.; Zhao, J. Lateral heterostructures of monolayer group-IV monochalcogenides: band alignment and electronic properties. *J. Mater. Chem. C* **2017**, *5*, 3788.

(31) Fei, R.; Li, W.; Li, J.; Yang, L. Giant Piezoelectricity of Monolayer Group IV Monochalcogenides: SnSe, SnS, GeSe, and GeS. *Applied Physics Letters* **2015**, *107*, 173104.

(32) Xu, L.; Yang, M.; Wang, S.J.; Feng, Y.P. Electronic and optical properties of the monolayer group-IV monochalcogenides MX (M = Ge, Sn; X = S, Se, Te). *Physical Review B* **2017**, *9*5, 235434.

(33) Chang, K.; Parkin, S.S.P. Experimental formation of monolayer group-IV monochalcogenides. *J. Appl. Phys.* **2020**, *127*, 220902.

(34) Mehboudi, M.; Fregoso, B.M.; Yang, Y.; Zhu, W.; Zande, A.; Ferrer, J.; Bellaiche, L.; Kumar, P.; Barraza-Lopez, S. Structural Phase Transition and Material Properties of Few-Layer Monochalcogenides. *Physical Review Letters* **2016**, *117*, 246802.

(35) Cheng, K.; Guo, Y.; Han, N.; Jiang, X.; Zhang, J.; Ahuja, R.; Su, Y. Zhao, J. 2D lateral heterostructures of group-III monochalcogenide: Potential photovoltaic applications. *Appl. Phys. Lett.* **2018**, *112*, 143902.

(36) Ye, Z.; Tan, C.; Huang, X.; Ouyang, Y.; Yang, L.; Wang, Z.; Dong, M. Emerging MoS_2 Wafer-Scale Technique for Integrated Circuits. *Nano-Micro Lett*. **2023**, *15*, 38.

(37) Budania, P.; Baine, P.T.; Montgomery, J.H.; McNeill, D.W.; Mitchell, S.J.N.; Modreanu, M.; Hurley, P.K. Comparison between Scotch tape and gel-assisted mechanical exfoliation techniques for preparation of 2D transition metal dichalcogenide flakes. *Micro & Nano Letters* **2017**, *12(12)*, 970–973.

(38) Ottaviano, L.; Palleschi, S.; Perrozzi, F.; D'Olimpio, G.; Priante, F.; Donarelli, M.; Benassi, P.; Nardone, M.; Gonchigsuren, M.; Gombosuren, M. *et al.* Mechanical exfoliation and layer number identification of MoS_2 revisited. *2D Mater.* **2017**, *4*, 045013.

(39) Liu, F. Mechanical exfoliation of large area 2D materials from vdW crystals. *Progress in Surface Science* **2021**, *96*, 100626.

(40) Dong, S.; Zhang, X.; Nathamgari, S.S.P.; Krayev, A.; Zhang, X.; Hwang, J.W.; Ajayan, P.M.; Espinosa, H.D. Facile fabrication of 2D material multilayers and vdW heterostructures with multimodal microscopy and AFM characterization. *Materials Today* **2022**, *52*, 1369-7021.

(41) Li, Z.; Ren, L.; Wang, S.; Huang, X.; Li, Q; Lu, Z.; Ding, S.; Deng, H.; Chen, P.; Lin, J.; Hu, Y.; Liao, L.; Liu, Y. Dry Exfoliation of Large-Area 2D Monolayer and Heterostructure Arrays. *ACS Nano* **2021**, *15*, 13839−13846.

(42) Li, Y.; Kuang, G.; Jiao, Z.; Yao, L.; Duan, R. Recent progress on the mechanical exfoliation of 2D transition metal dichalcogenides. *Mater. Res. Express* **2022**, *9*, 122001.

(43) Onodera, M.; Masubuchi, S.; Moriya, R.; Machida, T. Assembly of van der Waals heterostructures: exfoliation, searching, and stacking of 2D materials. *Japanese Journal of Applied Physics* **2020**, *59*, 010101.

(44) Lee, Y.-C.; Chang, S.-W.; Chen, S.-H.; Chen, S.-L.; Chen, H.-L. Optical Inspection of 2D Materials: From Mechanical Exfoliation to Wafer-Scale Growth and Beyond. *Adv. Sci.* **2022**, *9*, 2102128.

(45) Huang, Y.; Pan, Y.-H.; Yang, R.; Bao, L.-H.; Meng, L.; Luo, H.-L.; Cai, Y.-Q.; Liu, G.-D. *et al*. Universal mechanical exfoliation of large-area 2D crystals. *Nature communications* **2020**, *11*, 2453.

(46) Son, S.; Shin, Y.J.; Zhang, K.; Shin, J.; Lee, S.; Idzuchi, H.; Coak, M.J.; Kim, H.; Kim, J.; Jae Kim, H.; Kim, M.; Kim, D.; Kim, P.; Park, J.-G. Strongly adhesive dry transfer technique for van der Waals heterostructures. *2D Mater*. **2020**, *7*, 041005.

(47) Mlack, J.T.; Das, P.M.; Danda, G.; Chou, Y.-C.; Naylor, C.H.; Lin, Z.; López, N.P.; Zhang, T.; Terrones, M.; Johnson, A.T.C.; Drndić, M. Transfer of monolayer TMD WS_2 and Raman study of substrate effects. *Scientific Reports* **2017**, *7*, 43037.

(48) Park, M.; Choi, J.S.; Yan G.L.; Lee, H. Raman Spectra Shift of Few-Layer IV-VI 2D Materials. *Scientific Reports* **2019**, *9*, 19826.

(49) Yin, P.; Lin, Q.; Duan, Y. Applications of Raman spectroscopy in two-dimensional materials. *Journal of Innovative Optical Health Sciences* **2020**, *13*, 2030010.

(50) Saito, R.; Tatsumi, Y.; Huang, S.; Ling, X.; Dresselhaus, M.S. Raman spectroscopy of transition metal dichalcogenides. *J. Phys.: Condens. Matter* **2016**, *28*, 353002.

(51) Carvalho, B.R.; Pimenta, M.A. Resonance Raman spectroscopy in semiconducting transition-metal dichalcogenides: basic properties and perspectives. *2D Mater.* **2020**, *7*, 042001.

(52) Shao, F.; Zenobi, R. Tip-enhanced Raman spectroscopy: principles, practice, and applications to nanospectroscopic imaging of 2D materials. *Analytical and Bioanalytical Chemistry* **2019**, *411*, 37–61.

(53) Cong, X.; Liu, X.-L.; Lin, M.-L.; Tan, P.-H. Application of Raman spectroscopy to probe fundamental properties of two-dimensional materials. *npj 2D Materials and Applications* **2020**, *13(5),* 2030010.

(54) Song, X.; Guo, Z.; Zhang, Q.; Zhou, P.; Bao, W.; Zhang, D.W. Progress of Large-Scale Synthesis and Electronic Device Application of Two-Dimensional Transition Metal Dichalcogenides. *Small* **2017**, *13*, 1700098.

(55) Jariwala, D.; Sangwan, V.K.; Lauhon, L.J.; Tobin J. Marks, T.J.; Hersam, M.C. Emerging Device Applications for Semiconducting Two-Dimensional Transition Metal Dichalcogenides. *ACS Nano* **2014**, *8(2)*, 1102–1120.

(56) Yin, L.; Xu, K.; Wen, Y.; Wang, Z.; Huang, Y.; Wang, F.; Shifa, T.A.; Cheng, R.; Ma, H.; He, J. Ultrafast and ultrasensitive phototransistors based on few-layered $HfSe_2$. *Appl. Phys. Lett.* **2016**, *109*, 213105.

(57) Duan, X.; Wang, C.; Pan, A.; Yu, R.; Duan, X. Two-dimensional transition metal dichalcogenides as atomically thin semiconductors: opportunities and challenges. *Chem. Soc. Rev*. **2015**, *44*, 8859.

(58) Choi, W.; Choudhary, N.; Han, G.H.; Park, J.; Akinwande, D.; Lee, Y.H. Recent development of two-dimensional transition metal dichalcogenides and their applications. *Materials Today* **2017**, *20(3)*, 1369-7021.

(59) Peng, B.; Ang, P.K.; Loh, K.P. Two-dimensional dichalcogenides for light-harvesting applications. *Nano Today* **2015**, *10*, 128—137.

(60) Pu, J.; Takenobu, T. Monolayer Transition Metal Dichalcogenides as Light Sources. *Adv. Mater.* **2018**, *30*, 1707627.

(61) Wang, Q.H.; Kalantar-Zadeh, K.; Kis, A.; Coleman, J.N.; Strano, M.S. Electronics and optoelectronics of two-dimensional transition metal dichalcogenides. *Nature Nanotechnology*, **2017**, *7*, 699-712.

(62) Mak, K.F.; Shan, J. Photonics and optoelectronics of 2D semiconductor transition metal dichalcogenides. *Nature Photonics* **2016**, *10*, 216-226.

(63) Krasnok, A.; Lepeshov, S.; Alu, A. Nanophotonics with 2D transition metal dichalcogenides. *Optics Express* **2018**, *26(12)*, 15972.

(64) Mu, C. Photodetectors based on sensitized two-dimensional transition metal dichalcogenides—A review. *J. Mater. Res.* **2017**, 32(22), 4115-4131.

(65) Pei, Y.; Chen, R.; Xu, H.; He, D.; Jiang, C.; Li, W.; Xiao, X. Recent progress about 2D metal dichalcogenides: Synthesis and application in photodetectors. *Nano Res.* **2021**, *14(6)*, 1819–1839.

(66) Niu, L.; Li, K.; Zhen, H.; Chui, Y.-S.; Zhang, W.; Yan, F.; Zheng, Z. Salt-Assisted High-Throughput Synthesis of Single- and Few-Layer Transition Metal Dichalcogenides and Their Application in Organic Solar Cells. *Small* **2014**, *10(22)*, 4651–4657.

(67) Eftekhari, A. Tungsten dichalcogenides (WS_2, WSe_2, and WTe_2): materials chemistry and applications. *J. Mater. Chem. A* **2017**, *5*, 18299.

(68) Zibouche, N.; Kuc, A.; Musfeldt, J.; Heine, T. Transition-metal dichalcogenides for spintronic applications. *Ann. Phys.* **2014**, *9-10*, 395–401.

(69) Liu, Y.; Gao, Y.; Zhang, S.; He, J.; Yu, J.; Liu, Z. Valleytronics in transition metal dichalcogenides materials. *Nano Res.* **2019**, *12(11)*, 2695–2711.

(70) Mirabelli, G.; McGeough, C.; Schmidt, M.; McCarthy, E.K.; Monaghan, S.; Povey, I.M.; McCarthy, M.; Gity, F.; Nagle, R.; Hughes, G.; Cafolla, A.; Hurley, P.K.; Duffy, R. Air sensitivity of MoS_2, $MoSe_2$, $MoTe_2$, HfS_2, and $HfSe_2$. *J. Appl. Phys.* **2016**, *120*, 125102.

(71) Li, Q.; Zhou, Q.; Shi, L.; Chen, Q.; Wang, J. Recent advances in oxidation and degradation mechanisms of ultrathin 2D materials under ambient conditions and their passivation strategies. *J. Mater. Chem. A*, **2019**, *7*, 4291.

(72) Chae, S.H.; Jin, Y.; Kim, T.S.; Chung, D.S.; Na, H.; Nam, H.; Kim, H.; Perello, D.J.; Jeong, H.Y.; Ly, T.H.; Lee, Y.H. Oxidation Effect in Octahedral Hafnium Disulfide Thin Film. *ACS Nano* **2016**, *10,* 1309−1316.

(73) Li, Q.; Shi, L.; Wu, R.; Lin, C.; Bai, X.; Ouyang, Y.; Baraiya, B.A.; Jhac, P.K.; Wang, J. Unveiling chemical reactivity and oxidation of 1T-phased group VI disulfides. *Phys.Chem.Chem.Phys.* **2019**, *21*, 17010.

(74) Yao, Q.; Zhang, L.; Bampoulis, P.; Zandvliet, H.J.W. Nanoscale Investigation of Defects and Oxidation of $HfSe_2$. *J. Phys. Chem. C* **2018**, *122*, 25498−25505.

(75) Davis, S.M. Photoemission studies of Rhenium Disulfide Oxidation: Altered core-level structure and reactivity of defect states. *Catalysis Letters* **1989**, *2*, 1-8.

(76) Kotsakidis, J.C.; Zhang, Q.; Vazquez de Parga, A.L.; Currie, M.; Helmerson, K.; D. Kurt Gaskill, D.K.; Fuhrer, M.S. Oxidation of Monolayer WS_2 in Ambient Is a Photoinduced Process. *Nano Lett.* **2019**, *19*, 5205−5215.

(77) Liu, Y.; Tan, C.; Chou, H.; Nayak, A.; Wu, D.; Ghosh, R.; Chang, H.-Y.; Hao, Y.; Wang, X.; Kim, J.-S.; Piner, R.; Ruoff, R.S.; Akinwande, D.; Lai, K. Thermal Oxidation of WSe_2 Nanosheets Adhered on SiO_2/Si Substrates. *Nano Lett*. **2015**, *15*, 4979−4984.

(78) Addou, R.; Smyth, C.M.; Noh, J.-Y.; Lin, Y.-C.; Pan, Y.; Eichfeld, S.M.; Fölsch, S.; Robinson, J.A.; Cho, K.; Feenstra, R.M.; Wallace, R.M. One dimensional metallic edges in atomically thin WSe_2 induced by air exposure. *2D Mater*. **2018**, *5*, 025017.

(79) Santosh K.C.; Longo, R.C.; Wallace, R.M.; Cho, K. Surface oxidation energetics and kinetics on MoS_2 monolayer. *Journal of Applied Physics* **2015**, *117*, 135301.

(80) Ryu, Y.; Kim, W.; Koo, S.; Kang, H.; Watanabe, K.; Taniguchi, T.; Ryu, S. Interface-Confined Doubly Anisotropic Oxidation of Two-Dimensional MoS_2. *Nano Lett.* **2017**, *17*, 7267−7273.

(81) Hou, X.; Lin, Q.; Wei, Y.; Hao, Q.; Ni, Z.; Qiu, T. Surface-Enhanced Raman Scattering Monitoring of Oxidation States in Defect-Engineered Two-Dimensional Transition Metal Dichalcogenides. *J. Phys. Chem. Lett.* **2020**, *11*, 7981−7987.

(82) Martincova, J.; Otyepka, M.; Lazar, P. Oxidation of metallic two-dimensional transition metal dichalcogenides: 1T-MoS_2 and 1T-TaS_2. *2D Mater*. **2020**, *7*, 045005.

(83) Kang, S.; Kim, Y.S.; Jeong, J.H.; Kwon, J.; Kim, J.H.; Jung, Y.; Kim, J.H.; Kim, B.; Bae, S.H.; Huang, P.Y.; Hone, J.C.; Hu; Jeong, H.Y.; Park, J.-W.; Lee, C.-H.; Lee, G.-H. Enhanced Photoluminescence of Multiple Two-Dimensional van der Waals Heterostructures Fabricated by Layer-by-Layer Oxidation of MoS_2. *ACS Appl. Mater. Interfaces* **2021**, *13*, 1245−1252.

(84) Sirota, B.; Glavin, N.; Krylyuk, S.; Davydov, A.V.; Voevodin, A.A. Hexagonal $MoTe_2$ with Amorphous BN Passivation Layer for Improved Oxidation Resistance and Endurance of 2D Field Effect Transistors. *Scientific Reports* **2018**, *8*, 8668.

(85) Gan, Y.; Liang, J.; Cho, C.; Li, S.; Guo, Y.; Ma, X.; Wu, X.; Wen, J.; Du, X.; He, M.; Liu, C.; S Yang, S.A.; Wang, K.; Zhang, L. Bandgap opening in $MoTe_2$ thin flakes induced by surface oxidation. *Front. Phys.* **2020**, *15(3)*, 33602.

(86) Pace, S.; Martini, L.; Convertino, D.; Keum, D.H.; Forti, S.; Pezzini, S.; Fabbri, F.; Mišeikis, V.; Coletti, C. Synthesis of Large-Scale Monolayer 1T'-$MoTe_2$ and Its Stabilization via Scalable hBN Encapsulation. *ACS Nano* **2021**, *15*, 4213−4225.

(87) Borodin, B.R.; Benimetskiy, F.A.; Alekseev, P.A. Substrate-dependent degradation of thin TMDC layers in ambient conditions. *Journal of Physics: Conference Series* **2020**, *1695*, 012197.

(88) Ahn, S.; Kim, G.; Nayak, P.K.; Yoon, S.I.; Lim, H.; Shin, H.-J.; Suk Shin, H.S. Prevention of Transition Metal Dichalcogenide Photodegradation by Encapsulation with h-BN Layers. *ACS Nano* **2016**, *10*, 8973−8979.

(89) Rong, Y.; He, K.; Pacios, M.; Robertson, A.W.; Bhaskaran, H.; Warner, J.H. Controlled Preferential Oxidation of Grain Boundaries in Monolayer Tungsten Disulfide for Direct Optical Imaging. *ACS Nano* **2015**, *9(4)*, 3695–3703.

(90) Iqbal, M.W.; Iqbal, M.Z.; Khan, M.F.; Shehzad, M.A.; Seo, Y.; Park, J.H.; Hwang, C.; Eom, J. High-mobility and air-stable single layer WS_2 field-effect transistors sandwiched between chemical vapor deposition-grown hexagonal BN films. *Scientific Reports* **2015**, *5*, 10699.

(91) Kang, M.; Yang, H.I.; Choi, W. Oxidation of WS_2 and WSe_2 monolayers by ultraviolet-ozone treatment. *J. Phys. D: Appl. Phys.* **2019**, *52*, 505105 (6pp).

(92) Yamamoto, M.; Dutta, S.; Aikawa, S.; Nakaharai, S.; Wakabayashi, K.; Fuhrer, M.S.; Ueno, K.; Tsukagoshi, K. Self-Limiting Layer-by-Layer Oxidation of Atomically Thin WSe_2. *Nano Lett*. **2015**, *15*, 2067−2073.

(93) Li, Z.; Yang, S.; Dhall, R.; Kosmowska, E.; Shi, H.; Chatzakis, I.; Cronin, S.B. Layer Control of WSe_2 via Selective Surface Layer Oxidation. *ACS Nano* **2016**, *10*, 6836−6842.

(94) Shioya, H.; Tsukagoshi, K.; Ueno, K.; Oiwa, A. Selective oxidation of the surface layer of bilayer WSe_2 by laser heating. *Japanese Journal of Applied Physics* **2019**, *58*, 120903.

(95) Tan, C.; Liu, Y.; Chou, H.; Kim, J.-S.; Wu, D.; Akinwande, D.; Lai, K. Laser-assisted oxidation of multi-layer tungsten diselenide nanosheets. *Applied Physics Letters* **2016**, *108*, 083112.

(96) Ahn, S.; Kim, G.; Nayak, P.K.; Yoon, S.I.; Lim, H.; Shin, H.-J.; Shin, H.S. Prevention of Transition Metal Dichalcogenide Photodegradation by Encapsulation with h-BN Layers. *ACS Nano* **2016**, *10*, 8973−8979.

(97) Fan. Y.; Lee, J.; Hu, J.; Mao, Z.; Wei, J.; Feng, P.X.-L. Environmental Instability and Degradation of Single and Few-Layer WTe_2 Nanosheets in Ambient Conditions. *Small* **2016**, *12(42)*, 5802–5808.

(98) Yang, J.; Jin, Y.; Xu, W.; Zheng, B.; Wang, R.; Xu, H. Oxidation-Induced Topological Phase Transition in Monolayer 1T'- WTe_2. *J. Phys. Chem. Lett.* **2018**, *9*, 4783−4788.

(99) Hou, F.; Zhang, D.; Sharma, P.; Singh, S.; Wu, T.; Seidel, J. Oxidation Kinetics of WTe_2 Surfaces in Different Environments. *ACS Appl. Electron. Mater.* **2020**, *2*, 2196−2202.

(100) Wang, Y.Y.; Huang, S.M.; Yu, K.; Jiang, J.; Liang, Y.; Zhong, B.; Zhang, H.; Kan, G.F.; Quan, S.F.; Yu, J. Atomically flat HfO_2 layer fabricated by mild oxidation HfS_2 with controlled number of layers. *J. Appl. Phys.* **2020***, 127*, 214303.

(101) Liu, L.; Li, Y.; Huang, X.; Chen, J.; Yang, Z.; Xue, K.-H.; Xu, M.; Chen, H.; Zhou, P.; Miao, X. Low-Power Memristive Logic Device Enabled by Controllable Oxidation of 2D $HfSe_2$ for In-Memory Computing. *Adv. Sci.* **2021**, *8(15)*, 2005038.

(102) Kang, M.; Rathi, S.; Lee, I.; Li, L.; Khan, M.A.; Lim, D.; Lee, Y.; Park, J.; Yun, S.J.; Youn, D.-H.; Jun, C.; Kim, G.-H. Tunable electrical properties of multilayer $HfSe_2$ field effect transistors by oxygen plasma treatment. *Nanoscale* **2017**, *9*, 1645.

(103) Cruz, A.; Mutlu, Z.; Ozkan, M.; Ozkan, C.S. Raman investigation of the air stability of 2H polytype $HfSe_2$ thin films. *MRS Communications* **2018**, *8*, 1191‑1196.

(104) Gao, E.; Lin, S., Qin, Z.; Buehler, M.J.; Feng, X.; Xu, Z. Mechanical exfoliation of two-dimensional materials. *Journal of the Mechanics and Physics of Solids* **2018**, *115*, 248–262.

(105) Mleczko, M.J.; Zhang, C.; Lee, H.R.; Kuo, H.-H.; Magyari-Köpe, B.; Moore, R.G.; Shen, Z.-X.; Fisher, I.R.; Nishi, Y.; Pop, E. $HfSe_2$ and $ZrSe_2$: Two-dimensional semiconductors with native high-k oxides. *Sci. Adv.* **2017**, *3*, e1700481.

(106) Yang, L.; Tiwari, S.C.; Jo, S.S.; Hong, S.; Mishra, A.; Krishnamoorthy, A.; Kalia, R.K.; Nakano, A.; Jaramillo, R.; Vashishta, P. Unveiling oxidation mechanism of bulk ZrS_2. *MRS Advances* **2021**, *6*, 303–306.

(107) Pradhan, N.R.; Garcia, C.; Isenberg, B.; Rhodes, D.; Feng, S.; Memaran, S.; Xin, Y.; McCreary, A.; Walker, A.R.H; Raeliarijaona, A.; Terrones, H.; Terrones, M.; McGill, S.; Balicas, L. Phase Modulators Based on High Mobility Ambipolar $ReSe_2$ Field- Effect Transistors. *Scientific Report* **2018**, *8*, 12745.

(108) Rong, Y.; He, K.; Pacios, M.; Robertson, A.W.; Bhaskaran, H.; Warner, J.H. Controlled Preferential Oxidation of Grain Boundaries in Monolayer Tungsten Disulfide for Direct Optical Imaging. *ACS Nano* **2015**, *9(4)*, 3695–3703.

(109) Iqbal, M.W.; Iqbal, M.Z.; Khan, M.F.; Shehzad, M.A.; Seo, Y.; Park, J.H.; Hwang, C.; Eom, J. High-mobility and air-stable single layer WS_2 field-effect transistors sandwiched between chemical vapor deposition-grown hexagonal BN films. *Scientific Reports* **2015**, *5*, 10699.

(110) Kotsakidis, J.C.; Zhang, Q.; Vazquez de Parga, A.L.; Currie, M.; Helmerson, K.; Gaskill, D.K.; Fuhrer., M.S. Oxidation of Monolayer WS_2 in Ambient Is a Photoinduced Process. *Nano Lett.* **2019**, *19*, 5205−5215.

(111) Kang, M.; Yang, H.I.; Choi, W. Oxidation of WS_2 and WSe_2 monolayers by ultraviolet-ozone treatment. *J. Phys. D: Appl. Phys.* **2019**, *52*, 505105 (6pp).

(112) Liu, Y.; Tan, C.; Chou, H.; Nayak, A.; Wu, D.; Ghosh, R.; Chang, H.-Y.; Hao, Y.; Wang, X.; Kim, J.-S.; Piner, R.; Ruoff, R.S. *et al*. Thermal Oxidation of WSe_2 Nanosheets Adhered on SiO_2/Si Substrates. *Nano Lett.* **2015**, *15*, 4979−4984.

(113) Yao, K.; Femi-Oyetoro, J.D.; Yao, S.; Jiang, Y.; Bouanani, L.E.; Jones, D.C.; Ecton, P.A.; Philipose, U.; Bouanani, M.E.; Rout, B.; Neogi, Perez, J.M. Rapid ambient degradation of monolayer MoS_2 after heating in air. *2D Mater.* **2020**, *7*, 015024.

(114) Huang, F.; Lv, Y.; Zhang, S.; Wei, G.; Zhao, S. Instability and protection of monolayer WS_2 under heating and corona discharge conditions. *Mater. Res. Express* **2019**, *6*, 115084.

(115) Pace, S.; Ferrera, M.; Convertino, D.; Piccinini, G.; Magnozzi, M.; Mishra, N.; Forti, S.; Bisio, F.; Canepa, M.; Fabbri, F.; Coletti, C. Thermal stability of monolayer WS_2 in BEOL conditions. *J. Phys. Mater.* **2021**, *4*, 024002.

(116) Karasinski, P.; Kazmierczak, A.; Zieba, M.; Tyszkiewicz, C.; Wojtasik, K.; Kielan, P. Highly Sensitive Sensor Structure Based on Sol-Gel Waveguide Films and Grating Couplers. *Electronics* **2021**, *10*, 1389.

(117) Karasinski, P.; Zieba, M.; Gondek, E.; Nizioł, J.; Gorantla, S.; Rola, K.; Bachmatiuk, A.; Tyszkiewicz, C. Sol-Gel Derived Silica-Titania Waveguide Films for Applications in Evanescent Wave Sensors—Comprehensive Study. *Materials* **2022**, *15*, 7641.

(118) Kozlowski L.; Shahbaz, M.; Butt, M.A.; Tyszkiewicz, C.; Karasinski, P.; Kazmierczak, A.; Piramidowicz, R. Low-cost Integrated Photonic Platform Developed via a Sol-gel Dip-coating Method: A Brief Review. *Sensors & Transducers*, **2020**, *259(5)*, 82-92.

(119) Butt, M.A.; Tyszkiewicz, C.; Karasinski, P.; Zieba, M.; **Hlushchenko, D**.; Baraniecki, T.; Kazmierczak, A.; Piramidowicz, R.; Guzik, M.; Bachmatiuk, A. Development of a low-cost silica-titania optical platform for integrated photonics applications. *Optics Express* **2022**, *30(13)*, 23678

(120) Butt, M.A.; Kazmierczak, A.; Tyszkiewicz, C.; Karasinski, P.; Środa, E.; Olszewski, J.; Pala, P.; Martynkien, T.; **Hlushchenko, D.**; Baraniecki, T.; Bachmatiuk, A.; Jusza, A.; Guzik, M.; Piramidowicz, R. HYPHa project: a low-cost alternative for integrated photonics. *Photonic letters of Poland* **2022**, *14(2)*, 25-27.

(121) Butt, M.A.; Kazmierczak, A.; Tyszkiewicz, C.; Karasinski, P.; Piramidowicz, R. Mode Sensitivity Exploration of Silica–Titania Waveguide for Refractive Index Sensing Applications. *Sensors* **2021**, *21*, 7452.

(122) Butt, M.A.; Tyszkiewicz, C.; Karasinski, P.; Zieba, M.; Kazmierczak, A.; Zdonczyk, M.; Duda, Ł.; Guzik, M.; Olszewski, J.; Martynkien, T.; *et al*. Optical Thin Films Fabrication Techniques—Towards a Low-Cost Solution for the Integrated Photonic Platform: A Review of the Current Status. *Materials* **2022**, *15*, 4591.

(123) Butt, M.A.; Tyszkiewicz, C.; Wojtasik, K.; Karasinski, P.; Kazmierczak, A.; Piramidowicz, R. Subwavelength Grating Waveguide Structures Proposed on the Low-Cost Silica–Titania Platform for Optical Filtering and Refractive Index Sensing Applications. *Int. J. Mol. Sci.* **2022**, *23*, 6614.

(124) Rinke T.J.; Koch, C. Photolithography: Basis of Microstructuring. MicroChemicals, Germany, **2017**.

(125) Pal, P.; Sato, K. A comprehensive review on convex and concave corners in silicon bulk micromachining based on anisotropic wet chemical etching. *Micro and Nano Systems Letters* **2015**, *3(6)*, 1-42.

(126) Buhlery, J.; Steiner, F.-P.; Baltes, H. Silicon dioxide sacrificial layer etching in surface micromachining. *J. Micromech. Microeng*. **1997**, *7*, 1-13.

(127) Schulman, D.S.; Arnold, A.J.; Das, S. Contact engineering for 2D materials and devices. *Chem. Soc. Rev*. **2018**, *47*, 3037.

(128) Chen, Y.; Li, Y.; Wu, J.; Duan, W. General criterion to distinguish between Schottky and Ohmic contacts at the metal/two-dimensional semiconductor interface. *Nanoscale* **2017**, *9*, 2068.

(129) Chu, C.-H.; Lin, H.-C.; Yeh, C.-H.; Liang, Z.-Y.; Chou, M.-Y.; Chiu, P.-W. End-Bonded Metal Contacts on WSe_2 Field- Effect Transistors. *ACS Nano* **2019**, *13*, 8146−8154.

(130) Zhang, W.; Chiu, M.-H.; Chen, C.-H.; Chen, W.; Li, L.-J.; Wee, L.-J. Role of Metal Contacts in High-Performance Phototransistors Based on WSe_2 Monolayers. *ACS Nano* **2014**, *8*, 8653–8661.

(131) Wang, X.; Kim, S.Y.; Wallace, R.M. Interface Chemistry and Band Alignment Study of Ni and Ag Contacts on MoS_2. *ACS Appl. Mater. Interfaces* **2021**, *13*, 15802−15810.

(132) Wang, X.; Hu, Y.; Kim, S.Y.; Addou, R.; Cho, K.; Wallace, R.M. Origins of Fermi Level Pinning for Ni and Ag Metal Contacts on Tungsten Dichalcogenides. *ACS Nano* **2023**, *17*, 20353−20365.

(133) Guo, C.; Wang, F.; Wang, T.; Liu, Y. Anisotropic interface characteristics of bilayer GeSe based field effect transistors. *Physica E* **2022**, *142*, 115317.

(134) Zhao, P.; Yang, H.; Li, J.; Jin, H.; Wei, W.; Yu, L.; Huang, B.; Dai, Y. Design of new photovoltaic systems based on two-dimensional group-IV monochalcogenides for high performance solar cells. *J. Mater. Chem. A* **2017**, *5*, 24145.

(135) Guo, Y.; Pan, F.; Ren, Y.; Wang, Y.; Yao, B.; Zhao, G.; Lu, J. Anisotropic interfacial properties of monolayer GeSe—metal contacts. *Semicond. Sci. Technol.* **2019**, *34*, 095021 (12pp).

(136) Guo, Y.; Zhao, G.; Pan, F.; Quhe, R.; Lu, J. The Interfacial Properties of Monolayer MX–Metal Contacts. *Journal of Electronic Materials* **2022**, *51*, 4824–4835.

(137) Zhang, P.; Zhang, Y.; Wei, Y.; Jiang, H.; Wang, X.; Gong, Y. Contact engineering for two-dimensional semiconductors. *Journal of Semiconductors* **2020**, *41*, 071901.

(138) Liu, N.; Zhou, S.; Gao, N.; Zhao, J. Tuning Schottky barriers for monolayer GaSe FETs by exploiting a weak Fermi level pinning effect. *Phys.Chem.Chem.Phys.* **2018**, *20*, 21732.

(139) Yan, Y.; Deng, Q.; Li, S.; Guo, T.; Li, X.; Jiang, X.; Song, X.; Huang, W.; Yang, J.; Xia, C. In-plane ferroelectricity in few-layered GeS and its van der Waals ferroelectric diodes. *Nanoscale* **2021**, *13,* 16122.

(140) Chuanxi, Y.; Sun, L.; Brandt, R.E.; Kim, S.B.; Zhao, X.; Feng, J.; Buonassisi, T.; Gordon, R.G. Measurement of Contact Resistivity at Metal-Tin Sulfide (SnS) Interfaces. *Journal of Applied Physics* **2017**, *122(4)*, 045303.

(141) Yang, C.; Sun, L.; Brandt, R.E.; Kim, S.B.; Zhao, X.; Feng, J.; Buonassisi, T.; Gordon, R.G. Measurement of contact resistivity at metal-tin sulfide (SnS) interfaces. *Journal of applied physics* **2017**, *122*, 045303 .

(142) He, C.; Cheng, M.; Li, T.; Zhang, W.; Tunable Ohmic, p-Type Quasi-Ohmic, and n-Type Schottky Contacts of Monolayer SnSe with Metals. *ACS Appl. Nano Mater*. **2019**, *2*, 2767−2775.

(143) Cho, S.-H.; Cho, K.; Park, N.-W.; Park, S.; Koh, J.-H.; Lee, S.-K. Multi-Layer SnSe Nanoflake Field-Effect Transistors with Low-Resistance Au Ohmic Contacts. *Nanoscale Research Letters* **2017**, *12*, 373.

(144) Wang, Y.; Kim, J.C.; Wu, R.J.; Martinez, J.; Song, X.; Yang, J.; Zhao, F.; Mkhoyan, A.; Jeong, H.Y.; Chhowalla, M. Van der Waals contacts between three-dimensional metals and two-dimensional semiconductors. *Nature* **2019**, *568*, 70.

(145) Kwon, H.; Lee, K.; Heo, J.; Oh, Y.; Lee, H.; Appalakondaiah, S.; Ko, W.; Kim, H.W.; Jung, J.-W.; Suh, H.; Min, H.; Jeon, I.; Hwang, E.; Hwang, S. Characterization of Edge Contact: Atomically Resolved Semiconductor–Metal Lateral Boundary in MoS_2. *Adv. Mater.* **2017**, *29*, 1702931.

(146) Wang, Y. Electrical contacts on two-dimensional transition metal dichalcogenide semiconductors. University of Cambridge Repository, **2021**. https://doi.org/10.17863/CAM.77546.

(147) Parto, K.; Pal, A.; Chavan, T.; Agashiwala, K.; Yeh, C.-H.; Cao, W.; Banerjee, K. One-Dimensional Edge Contacts to Two-Dimensional Transition-Metal Dichalcogenides: Uncovering the Role of Schottky-Barrier Anisotropy in Charge Transport across MoS_2/Metal Interfaces. *Physical Review Applied* **2021**, *15*, 064068.

(148) Kim, C.; Moon, I.; Lee, D.; Choi, M.S.; Ahmed, F.; Nam, S.; Cho, Y.; Shin, H.-J.; Park, S.; Yoo, W.J. Fermi Level Pinning at Electrical Metal Contacts of Monolayer Molybdenum Dichalcogenides. *ACS Nano* **2017**, *11*, 1588−1596.

(149) McDonnell, S.; Azcatl, A.; Addou, R.; Gong, C.; Battaglia, C.; Chuang, S.; Cho, K.; Javey, A.; Wallace, R.M. Hole Contacts on Transition Metal Dichalcogenides: Interface Chemistry and Band Alignments. *ACS Nano* **2014**, *8(6)*, 6265-6272.

(150) Wang, Y.; Kim, J.C.; Li, Y.; Ma, K.Y.; Hong. S.; Kim. M.; Shin, H.S.; Jeong, H.Y.; Chhowalla, M. P-type electrical contacts for 2D transition-metal dichalcogenides. *Nature* **2022** *610(7930)*, 61-66.

(151) Ouyang, B.; Xiong, S.; Jing, Y. Tunable phase stability and contact resistance of monolayer transition metal dichalcogenides contacts with metal. *npj 2D Materials and Applications* **2018**, *13*, 1-13.

(152) Shimazu, Y.; Arai, K.; Iwabuchi, T. Metal–insulator transition in a transition metal dichalcogenide: Dependence on metal contacts. *IOP Conf. Series: Journal of Physics: Conf. Series* **2018**, *969*, 012105.

(153) Smyth, C.M.; Addou, R.; Hinkle, C.L.; Wallace, R.M. Origins of Fermi-Level Pinning between Molybdenum Dichalcogenides ($MoSe_2$, $MoTe_2$) and Bulk Metal Contacts: Interface Chemistry and Band Alignment. *J. Phys. Chem. C* **2019**, *123*, 23919−23930.

(154) Sar, H.; Ozden, A.; Demiroglu, I.; Sevik, C.; Perkgoz, N.K.; Ay, F. Long-Term Stability Control of CVD-Grown Monolayer MoS_2. *Phys. Status Solidi RRL* **2019**, *13*, 1800687.

(155) Smyth, C.M.; Addou, R.; Hinkle, C.L.; Wallace, R.M. Origins of Fermi Level Pinning between Tungsten Dichalcogenides (WS_2, WTe_2) and Bulk Metal Contacts: Interface Chemistry and Band Alignment. *J. Phys. Chem. C* **2020**, *124*, 14550−14563.

(156) Wang, X.; Hu, Y.; Kim, S.Y.; Addou, R.; Cho, K.; Wallace, R.M. Origins of Fermi Level Pinning for Ni and Ag Metal Contacts on Tungsten Dichalcogenides. *ACS Nano* **2023**, *17*, 20353−20365.

(157) Mitta, S.B.; Choi, M.S.; Nipane, A.; Ali, F.; Kim, C.; Teherani, J.T.; Hone, J.; Yoo, W.J. Electrical characterization of 2D materials-based field-effect transistors. *2D Mater.* **2021**, *8*, 012002.

(158) Go, J.S.; Kim, M.; Kim, S.; Jeon, H.; Hong, S.; Kim, J.; Oh, G.H.; Mane, S.M.; Kim, T.W. Optical and electrical properties of monolayer ReS_2 developed via chemical vapor deposition on SiO_2/Si substrate. *Journal of the Korean Physical Society* **2021**, *78*, 1109–1115.

(159) Zhang, L.; Tang, Y.; Yan, H.; Yildirim, T.; Yang, S.; Song, H.; Zhang, X.; Tian, F.; Luo, Z.; Pei, J. *et al*. Direct observation of contact resistivity for monolayer TMD based junctions via PL spectroscopy. *Nanoscale* **2022**, *14*, 8260.

(160) Moun, M.; Singh, A.; Singh, R. Study of Electrical Behavior of Metal-Semiconductor Contacts on Exfoliated MoS_2 Flakes. *Phys. Status Solidi A* **2018**, *215*, 1800188.

(161) Kayyalha, M.; Maassen, J.; Lundstrom, M.; Shi, L.; Chen, Y.P. Gate-tunable and thickness-dependent electronic and thermoelectric transport in few-layer MoS_2. *J. Appl. Phys.* **2016**, *120*, 134305.

(162) Chamlagain, B.; Khondaker, S.I. Rapid Degradation of the Electrical Properties of 2D MoS_2 Thin Films under Long-Term Ambient Exposure. *ACS Omega* **2021**, *6*, 24075−24081.

(163) Hunsperger, R.G. Integrated Optics. Theory and Technology. Fifth Edition, Springer-Verlag Berlin Heidelberg GmbH, **2002**.

(164) He, J.; Paradisanos, I.; Liu, T.; Cadore, A.R.; Liu, J.; Churaev, M.; Wang,R.N.; Raja, A.S.; Javerzac-Galy, C.; Roelli, P. *et al.* Loss Integrated Nanophotonic Circuits with Layered Semiconductor Materials. *Nano Lett.* **2021**, *21(7),* 2709–2718.

(165) Righini, G.C.; Dumeige, Y.; Feron, P.; Ferrari, M.; Conti, G.N.; Ristic, D.; Soria, S. Whispering gallery mode microresonators: Fundamentals and applications, Italy, **2011**, *34(7).*

(166) Anedda, A.; Carbonaro, C.M.; Clemente, F.; Corpino, R.; Ricci, P.C.; Rossini, S. Rhodamine 6G impregnated porous silica: A photoluminescence study. *Materials Science and Engineering C* **2005**, *25*, 641– 644.

(167) Bo, F.; Wang, J.; Cui, J.; Ozdemir, S.K.; Kong, Y.; Zhang, G.; Xu, J.; Yang, L. Lithium-Niobate–Silica Hybrid Whispering-Gallery-Mode Resonators. *Adv. Mater*. **2015**, *27*, 8075–8081.

(168) Chiasera, A.; Dumeige, Y.; Feron, P.; Ferrari, M.; Jestin, Y.; Conti, G.N.; Pelli, S.; Soria, S.; Righini, G.C. Spherical whispering-gallery-mode microresonators. *Laser & Photon* **2010**, *3(4)*, 457–482.

(169) Reynolds, T.; Riesen, N.; Meldrum, A.; Fan, X.; Hall, J.M.M.; Monro, T.M.; Francois, A. Fluorescent and lasing whispering gallery mode microresonators for sensing applications. *Laser Photonics* **2017**, *11(2)*, 1600265.

(170) Wei, G.-Q.; Wang, X.-D.; Liao, L.-S. Recent Advances in Organic Whispering-Gallery Mode Lasers. *Laser Photonics Rev*. **2020**, *14*, 2000257.

(171) Toropov, N.; Cabello, G.; Serrano, M.P.; Gutha, R.R.; Rafti, M.; Vollmer, F. Review of biosensing with whispering-gallery mode lasers. *Light: Science & Applications* **2021**, *10(42)*, 1-19.

(172) Hua, X.; Zhang, D.; Kim, B.; Seo, D.; Kang, K.; Yang, E.-H.; Hu, J.; Chen, X.; Liang, H.; Watanabe, K. *et al.* Stabilization of Chemical-Vapor-Deposition-Grown WS_2 Monolayers at Elevated Temperature with Hexagonal Boron Nitride Encapsulation. *ACS Appl. Mater. Interfaces* **2021**, *13*, 31271−31278.

(173) Behura, S.; Nguyen, P.; Che, S.; Debbarma, R.; Berry, V. Large-Area, Transfer-Free, Oxide-Assisted Synthesis of Hexagonal Boron Nitride Films and Their Heterostructures with MoS_2 and WS_2. *J. Am. Chem. Soc.* **2015**, *137*, 13060−13065.

(174) Huang, Z.; He, C.; Qi, X.; Yang, H.; Liu, W.; Wei, X.; Peng, X.; Zhong, J. Band structure engineering of monolayer MoS_2 on h-BN: first-principles calculations. *J. Phys. D: Appl. Phys.* **2014**, *47*, 075301 (6pp).

(175) Katoch, J.; Ulstrup, S.; Koch, R.J.; Moser, S.; McCreary, K.M.; Singh, S.; Xu, J.; Jonker, B.T.; Kawakami, R.K.; Bostwick, A. *et al.* Giant spin-splitting and gap renormalization driven by trions in single-layer WS_2/h-BN heterostructures. *Nature Physics* **2018**, *14*, 355–359.

(176) Withers, F.; Bointon, T.H.; Hudson, D.C.; Craciun, M.F.; Russo, S. Electron transport of WS_2 transistors in a hexagonal boron nitride dielectric environment. *Scientific report* **2014**, *4*, 4967.

(177) Uchiyama, Y.; Watanabe, K.; Taniguchi, T.; Kojima, K.; Endo, T.; Miyata, Y.; Shinohara, H.; Kitaura, R. Indirect bandgap of hBN-encapsulated monolayer MoS_2. *Condensed Matter* **2019**, *2*, 1903.

(178) Chen, M.; Haddon, R.C.; Yan, R.; Bekyarova, E. Advances in transferring chemical vapour deposition graphene: a review. *Mater. Horiz*. **2017**, *4*, 1054.

(179) Liu, L.; Liu, X.; Zhan, Z.; Guo, W.; Xu, C.; Deng, J.; Chakarov, D.; Hyldgaard, P.; Schröder, E.; Yurgens, A.; Sun, J. A Mechanism for Highly Efficient Electrochemical Bubbling Delamination of CVD-Grown Graphene from Metal Substrates. *Adv. Mater. Interfaces* **2016**, *3*, 1500492.

(180) Wang, Y.; Zheng, Y.; Xu, X.; Dubuisson, E.; Bao, Q.; Lu, J.; Loh, K.P. Electrochemical Delamination of CVD Grown Graphene Film: Toward the Recyclable Use of Copper Catalyst. *ACS Nano* **2011**, *12(5)*, 9927-9933.

(181) Lu, W.; Cheng, S.; Yan, M.; Wang, Y.; Xia, Y. Selective soluble polymer–assisted electrochemical delamination of chemical vapor deposition graphene. *J Solid State Electrochem* **2019**, *23*, 943–951.

(182) Wang, X.; Tao, L.; Hao, Y.; Liu, Z.; Chou, H.; Kholmanov, I.; Chen, S.; Tan, C.; Jayant, N.; Yu, Q.; Akinwande, D.; Ruoff, R.S. Direct Delamination of Graphene for High-Performance Plastic Electronics. *Small* **2014**, *10(4)*, 694–698.

(183) Cherian, C.T.; Giustiniano, F.; Martin-Fernandez, I.; Andersen, H.; Balakrishnan, J.; Özyilmaz, B. 'Bubble-Free' Electrochemical Delamination of CVD Graphene Films. *Small* **2015**, *11(2)*, 189–194.

(184) Reisfeld, R. Fluorescent Dyes in Sol-Gel Glasses. *Journal of Fluorescence* **2002**, *12*, 317-325.

(185) Jorge, J.; Castro, G.R.; Martinesa, M.A.U. Comparison among Different pH Values of Rhodamine B Solution Impregnated into Mesoporous Silica. *Orbital: The Electronic Journal of Chemistry* **2013**, *5(1)*, 23-29.

(186) Kumari, N.; Kalyan, M.; Ghosh, S.; Maity, A.R.; Mukherjee, R. Possible negative correlation between electrical and thermal conductivity in p-doped WSe_2 single crystal. *Mater. Res. Express* **2021**, 8, 045902.

(187) Ghosh, T.; Samanta, B.; Jana, P..C.; Ganguly, P. Comparison of calculated and measured refractive index profiles of continuous wave ultraviolate written waveguides in $LiNbO_3$ and its analysis by effective index based matrix method. *J. Appl. Phys*. **2015**, *117*, 053106.